To the Graduate Council:

I am submitting herewith a dissertation written by William Kelly Dagenhart entitled "Coulomb Excitation Studies of $^{115}$Sn." I recommend that it be accepted in partial fulfillment of the requirements for the degree of Doctor of Philosophy, with a major in Physics.

Paul H. Stelson

Paul H. Stelson, Major Professor

We have read this dissertation
and recommend its acceptance:

Carrol R. Bingham

Julius Smith

Leo T. Riedinger

H. K. McGowan

Russell L. Robinson

Accepted for the Council:

L Evans Roth

Vice Chancellor
Graduate Studies and Research

Thesis
T16
.D344
cop. 2

# COULOMB EXCITATION STUDIES OF $^{115}Sn$

A Dissertation

Presented for the

Doctor of Philosophy

Degree

The University of Tennessee, Knoxville

William Kelly Dagenhart

March 1977

1315333

# DEDICATION

This thesis is dedicated to the memory of my father.

# ACKNOWLEDGMENTS

It is a pleasure to express my sincere appreciation to Dr. P. H. Stelson who directed the research, and to Drs. F. K. McGowan, W. T. Milner, S. Raman, and R. L. Robinson for their considerable collaboration and involvement in the accomplishment of this work. I also wish to thank Drs. R. M. Ronningen and W. K. Tuttle for their helpful suggestions and for their assistance in taking data.

Mrs. Anita Barker was of great help in typing the rough draft. Mrs. Anita Barker was also especially patient and diligent in typing the manuscript for the dissertation and associated journal article under trying conditions.

The research described in this dissertation was carried out in the Physics Division of the Oak Ridge National Laboratory, which is operated by Union Carbide Corporation under contract with the U. S. Energy Research and Development Administration. The assistance of the entire staff of the Van de Graaff Laboratory, particularly the staff of the Tandem accelerator, and support from the former Isotopes Division and from the Fusion Energy Division of the Oak Ridge National Laboratory are gratefully acknowledged. I am especially appreciative of administrative support from my past immediate supervisors, W. A. Bell and L. O. Love of the Isotopes Division, and to my present immediate supervisors, Drs. W. L. Stirling and L. D. Stewart of the Fusion Energy Division.

The doctoral committee consisted of Professors P. H. Stelson, L. L. Riedinger, and C. R. Bingham of the Physics Department and

J. Smith of the Mathematics Department of the University of Tennessee, and Drs. F. K. McGowan and R. L. Robinson of ORNL.

I especially wish to thank my wife Sally and children Jonathan, Keith, David, and Pamela for their patience and understanding throughout this research. We finally made it.

# ABSTRACT

The tin isotopes, with Z = 50 are classified as "single-closed-shell nuclei," since Z = 50 is a magic number, and differences in their structure are determined completely by differences in the number of neutrons in the valence shells. The shell-model description of nuclei in this region is fairly simple, and makes possible detailed microscopic calculations. The Z = 50 region is one of the very few places among heavy nuclei where detailed shell-model calculations can be made and tested by comparison with experiment. The Coulomb excitation research described in this study was initiated to fill in experimental data on the nucleus $^{115}$Sn for which no Coulomb excitation data existed and which had not received very much study due to its low natural abundance.

For the Coulomb excitation measurements, five types of experiments were performed. First using α particle beams of 9.4, 10.0, and 10.6 MeV, γ-ray yields were taken at an angle, θ, between the beam and the detector of 55°. This data was used to refine existing level diagrams, look for new transitions, and measure B(E2)'s, B(M1)'s, and branching ratios. Secondly, γ-γ coincidence measurements were performed with a 10.6 MeV α-particle beam to confirm the level diagram and search for new transitions. Next, γ-ray angular distributions were taken using a 10.0 MeV α-particle beam to determine spins, parities, and γ-ray mixing ratios. Next, a beam of 45 MeV $^{16}$O ions was used to determine the lifetimes of states whose decaying γ-rays showed Doppler broadening. Finally, inelastic

particle spectra were taken with the reaction $^{115}Sn(\alpha,\alpha')^{115}Sn$ using the Enge split-pole magnetic spectrograph. These data provided an independent and accurate method of verifying the in-beam $\gamma$-ray measurements of $B_{ex}(E2)$.

Where theoretical calculations exist for comparison with the data the disagreement is still approximately 100% for most parameters.

# TABLE OF CONTENTS


| CHAPTER | | PAGE |
|---|---|---|
| I. | INTRODUCTION . . . . . | 1 |
| II. | THEORY OF COULOMB EXCITATION AND NUCLEAR MODELS . . . | 5 |
| | Introduction . . . . . | 5 |
| | The Classical Theory of Coulomb Excitation . . . . . | 7 |
| | Calculation of the Reduced Transition Probability . | 15 |
| | Angular Distribution of the De-excitation Gamma-Rays | 17 |
| III. | NUCLEAR MODELS . . . . . | 21 |
| | The Collective Model . . . . . | 21 |
| | Shell Model Calculations . . . . . | 27 |
| IV. | EXPERIMENTAL ARRANGEMENT AND PROCEDURE . . . . . | 31 |
| | Tandem Van de Graaff Beam Facility and Computer Data Handling Equipment . . . . . | 32 |
| | Enge Spectrograph Apparatus . . . . . | 36 |
| | Gamma-Ray Detectors . . . . . | 44 |
| | Gamma-Ray Singles Experiments . . . . . | 51 |
| | Gamma-Ray Angular Anisotropy Experiments . . . . . | 53 |
| | Gamma-Gamma Coincidence Experiments . . . . . | 55 |
| | Doppler Shift Lifetime Measurements . . . . . | 57 |
| | Target Preparation Techniques . . . . . | 60 |
| | Reduction of Gamma-Ray Spectra and ($\alpha$,$\alpha'$) Spectra . | 77 |
| V. | EXPERIMENTAL RESULTS . . . . . | 80 |
| | Gamma-Ray Singles . . . . . | 80 |
| | Gamma-Ray Anisotropies . . . . . | 101 |

CHAPTER PAGE

Gamma-Gamma Coincidence . . . . . 101

Inelastic Particle Spectra . . . . . 113

Data Summary . . . . . 123

VI. DISCUSSION AND CONCLUSIONS . . . . . 129

Discussion of Individual Levels of $^{115}Sn$ . . . . . 129

Comparison of the Enge and Gamma-Ray Results . . . . 133

Summary . . . . . 134

Concluding Remarks . . . . . 142

LIST OF REFERENCES . . . . . 143

APPENDIX . . . . . 148

VITA . . . . . 156

# LIST OF TABLES


| TABLE | | PAGE |
|---|---|---|
| I. | Mass analysis of thick $^{115}$Sn targets . . . . . | 62 |
| II. | Specifications for the thin and thick targets . . . | 64 |
| III. | Mass assay for the $^{115}$Sn thin target from the ion microprobe spectrum . . . . . | 75 |
| IV. | List of $\gamma$-rays from the $^{115}$Sn$(\alpha,\alpha'\gamma)^{115}$Sn reaction with identification of contaminant and $^{115}$Sn lines for the 28.52% $^{115}$Sn target . . . . . | 83 |
| V. | List of $\gamma$-rays from the $^{115}$Sn$(\alpha,\alpha'\gamma)^{115}$Sn reaction with identification of contaminant and $^{115}$Sn lines for the 92.31% $^{115}$Sn target . . . . . | 86 |
| VI. | Gamma-ray energies and internal conversion coefficients for $^{115}$Sn . . . . . | 93 |
| VII. | Summary of the $B_{ex}$(E2) values obtained for $^{115}$Sn from in-beam $\gamma$-ray measurements . . . . . | 95 |
| VIII. | Values taken for the effective stopping power of tin atoms in tin used to calculate Doppler broadened $\gamma$-ray peak shapes . . . . . | 97 |
| IX. | Calculated lifetimes for $^{115}$Sn states using Dagenhart and Dagenhart/Stelson stopping power tables and the $^{115}$Sn$(\alpha,\alpha'\gamma)^{115}$Sn Doppler shift measurements . . . | 100 |
| X. | Summary of $\gamma$-ray anisotropy results for $^{115}$Sn . . . | 102 |
| XI. | Summary of coincidence information obtained from the Coulomb excitation of $^{115}$Sn . . . . . | 112 |

TABLE PAGE

XII. Comparison of $B_{ex}(E2)$ from Enge magnet $^{115}Sn(\alpha,\alpha')^{115}Sn$ and in-beam $\gamma$-ray measurements . . . . . 122

XIII. Summary of information obtained from the Coulomb excitation of $^{115}Sn$ . . . . . 124

XIV. Comparison of published data on $^{115}Sn$ energy levels, transitions, and spin assignments with the present study . . . . . 130

XV. A comparison of experimental with theoretically calculated values for $B_d(M1)$, $B_d(E2)$, and T(E2)/T(M1) for the 497.35 keV transition . . . . . 138

XVI. A comparison of some experimental data from Nuclear Data Sheets on relative cross-sections for particle transfer reactions . . . . . 139

XVII. Systematics of the even-even and odd tin B(E2) center of gravities . . . . . 141

# LIST OF FIGURES


| FIGURE | | PAGE |
|---|---|---|
| 1. | Classical picture of the scattering of a particle of charge $Z_1e$ and mass $A_1$ by a target of charge $Z_2e$ and mass $A_2$ via Coulomb interaction . . . . . | 9 |
| 2. | Analogy between cascade $\gamma$-ray and Coulomb excitation angular distributions . . . . . | 18 |
| 3. | Effect of spin-orbit coupling on the level system of a well of a shape intermediate between the square and oscillator wells . . . . . | 30 |
| 4. | Schematic illustration of the arrangement for Coulomb excitation with the Tandem accelerator . . | 33 |
| 5. | Schematic illustration of the Enge split-pole magnetic spectrograph . . . . . | 38 |
| 6. | Schematic illustration of the 20 cm gas flow position sensitive proportional counter detector . . . . . | 41 |
| 7. | Enge magnet detector electronics for measuring inelastically scattered particles for the 20 and 60 cm detectors . . . . . | 43 |
| 8. | Linearity of the 20 cm gas flow proportional detector . . . . . | 45 |
| 9. | Absolute efficiency of the 60 $cm^3$ coaxial Ge(Li) detector as a function of $\gamma$-ray energy . . . . . | 48 |
| 10. | Absolute efficiency of the 100 $cm^3$ coaxial Ge(Li) detector as a function of $\gamma$-ray energy . . . . . | 50 |

FIGURE PAGE

11. Ge(Li) detector positions for γ-ray yield and angular anisotropy measurements (top view) . . . . . 52

12. Diagram of the electronics setup used in γ-γ coincidence measurements on $^{115}Sn$ . . . . . 54

13. Volume ion microprobe scan of the 28.52% $^{115}Sn$ target showing impurities . . . . . 65

14. Schematic of the 180° Oak Ridge Sector Isotope Separator ion optic system . . . . . 67

15. Schematic of the 180° Oak Ridge Sector Isotope Separator used to prepare the high purity thin tin targets . . . . . 68

16. Photograph of the 180° Oak Ridge Sector Isotope Separator target apparatus . . . . . 70

17. Schematic of the target apparatus used on the 180° Oak Ridge Sector Isotope Separator to prepare the high purity thin tin targets . . . . . 71

18. Ion microprobe scan of the 99.12% $^{115}Sn$ thin target (thickness 75 $\mu g/cm^2$) . . . . . 74

19. Ion microprobe scan of the 99.12% $^{115}Sn$ thin target showing impurities . . . . . 76

20. Gamma-ray spectrum observed with a 60 $cm^3$ Ge(Li) detector when 10.5 MeV α-particles Coulomb excited an isotopically enriched $^{115}Sn$ target whose enrichment was 28.52% $^{115}Sn$ . . . . . 81

FIGURE PAGE

21. Gamma-ray spectrum observed with a 100 $cm^3$ Ge(Li) detector when 10.6 MeV α-particles Coulomb excited an isotopically enriched $^{115}Sn$ target whose enrichment was 92.31% $^{115}Sn$ . . . . . 82

22. Energy level diagram of $^{115}Sn$ with branching ratios . 91

23. Doppler broadened γ-ray peaks observed when $^{115}Sn$ was Coulomb excited with 45 MeV $^{16}O$ projectiles. The detector was located at 0° to the beam . . . . 98

24. Doppler broadened γ-ray peak observed when $^{115}Sn$ was Coulomb excited with 45 MeV $^{16}O$ projectiles. The detector was located at 90° to the beam . . . . 99

25. The angular distribution coefficient $A_2$ vs δ for the spin sequence $\frac{1}{2}$ (E2) $\frac{3}{2}$ (E2 + M1)$\frac{1}{2}$ including experimental results for $^{115}Sn$, $E_\gamma$ = 1280.08 keV . 103

26. The angular distribution coefficient $A_2$ vs δ for the spin sequence $\frac{1}{2}$ (E2) $\frac{5}{2}$ (E2 + M1) $\frac{3}{2}$ including experimental results for $^{115}Sn$, $E_\gamma$ = 919.79 keV . 104

27. The angular distribution coefficient $A_2$ vs δ for the spin sequence $\frac{1}{2}$ (E2) $\frac{3}{2}$ (E2 + M1) $\frac{3}{2}$ including experimental results for $^{115}Sn$, $E_\gamma$ = 782.99 keV . . 105

28. The angular distribution coefficient $A_2$ vs δ for the spin sequence $\frac{1}{2}$ (E2) $\frac{3}{2}$ (E2 + M1) $\frac{1}{2}$ including experimental results for $^{115}Sn$, $E_\gamma$ = 497.35 keV . . 106

FIGURE PAGE

29. The angular distribution coefficient $A_2$ vs $\delta$ for the spin sequence $\frac{1}{2}$ (E2) $\frac{5}{2}$ (E2 + M1) $\frac{3}{2}$ including experimental results for $^{115}Sn$, $E_\gamma$ = 489.27 keV . . 107

30. The angular distribution coefficient $A_2$ vs $\delta$ for the spin sequence $\frac{1}{2}$ (E2) $\frac{5}{2}$ (E2 + M1) $\frac{5}{2}$ including experimental results for $^{115}Sn$, $E_\gamma$ = 430.27 keV . . 108

31. The angular distribution coefficient $A_2$ vs $\delta$ for the spin sequence $\frac{1}{2}$ (E2) $\frac{5}{2}$ (E2 + M1) $\frac{7}{2}$ including experimental results for $^{115}Sn$, $E_\gamma$ = 373.69 keV . . 109

32. The angular distribution coefficient $A_2$ vs $\delta$ for the spin sequence $\frac{1}{2}$ (E2) $\frac{3}{2}$ (E2 + M1) $\frac{5}{2}$ including experimental results for $^{115}Sn$, $E_\gamma$ = 293.60 keV . . 110

33. The angular distribution coefficient $A_2$ vs $\delta$ for the spin sequence $\frac{1}{2}$ (E2) $\frac{5}{2}$ (E2 + M1) $\frac{3}{2}$ including experimental results for $^{115}Sn$, $E_\gamma$ = 136.70 keV . . 111

34. Gated Enge magnet spectra of $^{115}Sn(\alpha,\alpha')^{115}Sn$ reaction at 10.0 MeV for the 25 $\mu g/cm^2$ target using the 20 cm position sensitive detector . . . . . 117

35. Ungated Enge magnet spectra of $^{115}Sn(\alpha,\alpha')^{115}Sn$ reaction at 9.5 MeV for the 75 $\mu g/cm^2$ target and the 60 cm position sensitive detector . . . . . 118

36. Gated Enge magnet spectrum of $^{115}Sn(\alpha,\alpha')^{115}Sn$ reaction at 10.2 MeV for the 75 $\mu g/cm^2$ target with the 60 cm position sensitive detector . . . . . 119

FIGURE PAGE

37. Gated sum pulse from the left and right detector pulses for the 10.2 MeV $^{115}Sn(\alpha,\alpha')^{115}Sn$ data of Figure 36 . . . . . 121

38. Level diagram showing the levels in $^{115}Sn$ which are observed from Coulomb excitation. Also shown are the values of $B_d(E2)/B_{sp}(E2)$ . . . . . 127

39. Level diagram showing the levels in $^{115}Sn$ which are observed from Coulomb excitation. Also shown are the values of $B_d(M1)$ taken from Table XIII in units of $(e\hbar/2mc)^2$ . . . . . 128

40. Level diagram for tin, displaying excitation strengths to the various states of $^{115,117,119}Sn$ . 135

41. Systematics of the levels in the odd tin nuclei in the energy region below 2 MeV . . . . . 136

42. Plating cell apparatus . . . . . 152

# CHAPTER I

## INTRODUCTION

The Coulomb excitation reaction has seen increasing use since the early 1950's in the study of nuclear structure. In this process target nuclei are bombarded by charged projectiles at subcoulomb barrier energies which excite low lying states in the target nuclei. Since the projectile energy is kept below the Coulomb barrier the electromagnetic interaction is the only one involved. As this force is completely understood, the dynamics of the interaction can be accurately calculated and some basic nuclear properties can be extracted in a model independent fashion.

The electromagnetic process tends to most strongly excite those nuclear states which exhibit a collective character and has thus been one of the most useful methods for studying collective motion in nuclei.

In practice one may observe the de-excitation $\gamma$ radiation, the inelastically scattered projectiles, or the internal conversion electrons resulting from a Coulomb excitation event. The most widely used technique has been the observation of the de-excitation $\gamma$-rays. From these observations one may extract such information as level energies, spins, relative parities, $\gamma$-ray multipolarities, multipole mixtures, and relative probabilities of various decay modes.

Tin nuclei are particularly interesting since they have a closed proton shell at $Z = 50$ and a detailed comparison can be made

between experiment and theory as the neutron number is varied. Relatively little work has been reported on the Coulomb excitation of the odd isotopes of tin.[1,2] The odd tin nuclei are typically vibrational and their structure is of interest from a shell model point of view.[3] A recent study by Stelson et al.,[4] has reported on the Coulomb excitation of $^{117,119}Sn$ with $\alpha$ and $^{16}O$ projectiles. In this study deduced levels, J, $\pi$, B(E2), B(M1), and $T_{1/2}$ values were reported. The rare isotope (0.35% N.A.) $^{115}Sn$ has been studied via reaction mechanisms by several authors,[5-8] but no results from Coulomb excitation studies have been reported. Schwengler[9] has studied the excited states of $^{115}Sn$ through the reaction $^{115}In(p,n\gamma)^{115}Sn$ and has reported J, $\pi$, and level energies. Madueme et al.[10] have studied $^{115}Sn$ through the reactions $^{115}In(p,n)^{115}Sn$, $^{112}Cd(\alpha,n)^{115}Sn$, $^{115}In(d,2n)^{115}Sn$, and $^{113}Cd(\alpha,2n)^{115}Sn$ and have proposed a level scheme containing 21 levels on the basis of measurement of: $\gamma$ ray energies and intensities, excitation functions, conversion electron intensities, $\gamma$-$\gamma$ and e-$\gamma$-coincidences and angular distribution of $\gamma$-rays.

The purpose of this research was to Coulomb excite enriched samples of $^{115}Sn$ nuclei with $\alpha$ and $^{16}O$ projectiles from the ORNL Tandem Van de Graaff accelerator and to measure $E_\gamma$, $I_\gamma$, $I_\gamma(\theta)$, $\gamma$-$\gamma$ coincidences and Doppler broadening with high efficiency Ge(Li) detectors. Inelastic $\alpha$ spectra from the reaction $^{115}Sn(\alpha,\alpha')^{115}Sn$ were measured with an Enge split pole magnetic spectrograph to

provide an additional measurement of $B_{ex}(E2)$. From these measurements a level scheme has been deduced and J, $\pi$, B(E2), B(M1), $\tau$ values are reported.

Chapters II and III present a brief review of the Coulomb excitation theory which is the basis of the present study. Sufficient detail is presented to give methods for data reduction for B(E2), B(M1), $\tau$ values from experimental data. Chapter IV describes the Tandem Van de Graaff and computer data handling facility which was used in these experiments. Chapter IV describes the Enge split pole magnetic spectrograph facility associated position sensitive proportional counter, and readout electronics for detecting $\alpha$ particles which have scattered from the thin $^{115}Sn$ targets. Details of the thin target preparation and data reduction are also presented. Chapter IV describes the gamma-ray in-beam experimental apparatus and experiments. Details of measurements for gamma-ray yields, gamma-ray angular anisotropy, gamma-gamma coincidence, and Doppler shift lifetime measurements are presented. Future experiments are discussed which could avoid many of the low Z target contaminant gamma-rays which have been encountered in this study. Chapter V presents the results from the gamma-ray singles experiments giving the deduced decay scheme and $B_{ex}(E2)$. Chapter V presents the results from the gamma-ray anisotropy measurements with the deduced spin-parity assignments. Chapter V presents results from the gamma-gamma coincidence measurements. The use of the gated spectra in verifying the deduced level scheme and in identifying contaminant gamma-rays is presented. Chapter VI summarizes the information

obtained in this study. A discussion is given of each nuclear level along with a comparison of the in-beam gamma results with the independent Enge measurements. Directions for future study of this nucleus are suggested.

# CHAPTER II

# THEORY OF COULOMB EXCITATION AND NUCLEAR MODELS

## A. INTRODUCTION

This chapter discusses those elements of Coulomb excitation theory and nuclear models that have been developed by others, which are most pertinent to this study. A brief outline of the derivation of the classical Coulomb excitation cross section by Alder et al.,[11] is given along with some of the more useful formulas and results. Some special cases are considered in which deviations from the simple classical theory are found to be significant, and methods for handling some of these problems are presented.

In the early stages of the study of nuclear reactions, the possibility was discussed of producing nuclear excitations by the long-range electric interactions of bombarding particles.[12] At incident energies so low that the Coulomb repulsion prevents the particles from penetrating into the nucleus, such excitation processes can be studied without interference from the more complicated nuclear interactions. Very early theoretical suggestions were made that an isomeric activity in indium, observed in charged particle bombardment, might have been produced by these long range electric interactions.[13] Prompted by these early observations the theory of "Coulomb excitation" reactions has received considerable development in recent years. In these developments it has been

found that in many cases of interest a classical treatment of the trajectory of the bombarding particle is justified and leads to simple quantitative expressions for the excitation cross sections.

It was recognized early that the Coulomb excitation reaction was particularly appropriate for studying the low lying collective excitations of nuclei, which are preferentially excited by the electric quadrupole field of the bombarding projectiles. The use of such methods developed into an especially important tool for studying the nuclear rotational and vibrational collective spectra. One of the first experimental uses of this method was discovered in an experiment on proton induced reactions in light nuclei, in which target backings of tantalum were used.[14] Background radiation observed in these experiments was later established as originating from proton induced Coulomb excitation of the tantalum nuclei.[15,16] The yield of these radiations were shown to be in complete agreement with electric quadrupole Coulomb excitation theory. It was also shown that the absolute cross sections and excitation energies could be interpreted in terms of rotational excitations.

The Coulomb excitation reaction has since been employed by many laboratories throughout the world for the study of nuclear levels. The scope of these initial investigations has been greatly expanded by the development of new instrumentation and techniques. Thus much additional information has been obtained from the successive development of NaI(Tl) detectors, surface barrier detectors, position sensitive proportional detectors, high resolution Ge(Li) detectors, and conversion spectrometers which are used in

experiments such as the measurement of internal conversion electrons, the measurement of inelastically scattered groups of projectiles, Doppler shift measurements, and the measurement of gamma-ray anisotropies.

The Coulomb excitation process itself has received extensive experimental investigation and the adequacy of the theoretical description has been tested. Thus, the excitation cross-section as a function of mass, energy, and charge of the projectile has been shown to be in good agreement with the classical theory, when the latter is appropriately modified to take into account the energy loss of the projectile.[17] On the other hand, accurate measurements of the angular distributions of gamma radiation from Coulomb excitation[18] have revealed significant deviations from the classical theory and have shown that a full quantum mechanical treatment is necessary to adequately describe the process. A full quantum mechanical treatment has been formulated which successfully describes these experiments.[19]

## B. THE CLASSICAL THEORY OF COULOMB EXCITATION

The motion of the projectile in the Coulomb field of the nucleus can be essentially characterized[20] by a dimensionless quantity $\eta$ which is defined by

$$\eta = Z_1 Z_2 e^2/\hbar v, \qquad \text{(II-1)}$$

where $Z_1e$ and $Z_2e$ are the nuclear charges of the projectile and target nucleus, respectively, and v is the velocity of the incident projectile. In order for the classical description to be valid we must always have $\eta >> 1$, which describes a strong interaction where the projectile energy is below the Coulomb barrier and the projectile will not penetrate the nucleus. For inelastic collisions the energy loss of the projectile must be small compared to the projectile energy in order for the classical description to be valid and so that the effect of the excitation on the projectile motion can be neglected. In the classical treatment of the Coulomb excitation process we consider the projectile as moving along a hyperbolic orbit in the repulsive Coulomb field of the target nucleus (see Figure 1). This scattering event may also be described by

$$\eta = a/\lambda\!\!\!^{-}, \qquad \text{(II-2)}$$

where $\lambda\!\!\!^{-}$ is the deBroglie wavelength of the projectile and a is one half the classical distance of closest approach in a head-on collision. The quantity a is given by

$$a = Z_1 Z_2 e^2/m_o v^2, \qquad \text{(II-3)}$$

where v is the incident velocity of the projectile and $m_o$ is the reduced mass of the projectile.

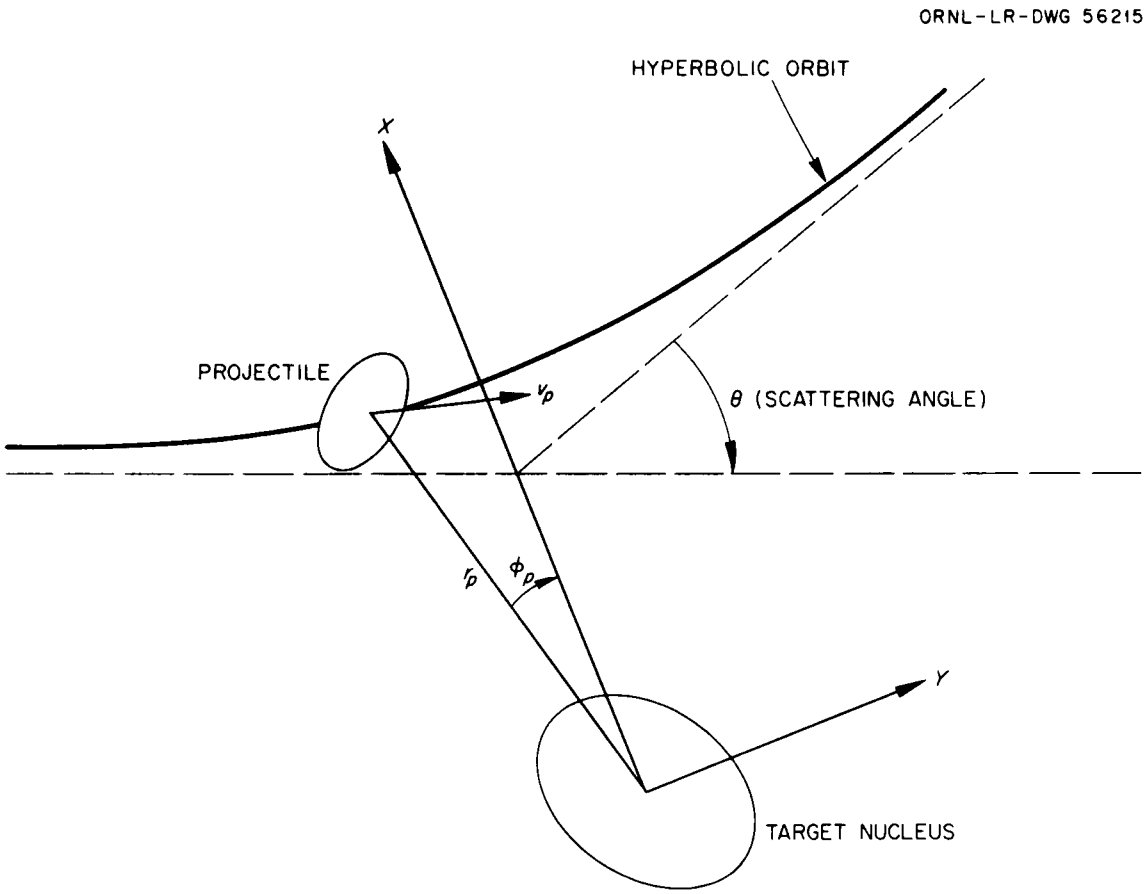


Figure 1. Classical picture of the scattering of a particle of charge $Z_1e$ and mass $A_1$ by a target of charge $Z_2e$ and mass $A_2$ via Coulomb interaction.

If the conditions for the classical scattering process are met then the classical differential cross section can be written

$$d\sigma = Pd\sigma_R, \tag{II-4}$$

where P is the probability that the nucleus is excited during a collision in which the particle is scattered into the solid angle $d\Omega$. The differential scattering cross section $d\sigma_R$ is given by the Rutherford law

$$d\sigma_R = \frac{1}{4} a^2 \sin^{-4}(\frac{\theta}{2}) d\Omega, \tag{II-5}$$

where $\theta$ is the scattering angle in the center-of-mass system.

The probability P can be expressed in terms of the amplitudes $b_{if}$ for a transition from an initial nuclear state i to the final nuclear states f. The probability P for excitation of a given energy level, irrespective of the orientation of the initial or final nuclear state can be expressed as

$$P = (2I_i + 1)^{-1} \sum_{M_i M_f} |b_{if}|^2, \tag{II-6}$$

where $M_i$ and $M_f$ are the magnetic quantum numbers of the initial and final nuclear states and where $I_i$ is the spin of the initial nuclear state.

If the projectile energy is kept well below the Coulomb barrier then the probability P for excitation in a single encounter can be

kept << 1 and first order perturbation theory is then expected to be accurate.[21] First order time dependent perturbation theory[22] may then be employed to obtain

$$b_{if} = \frac{1}{i\hbar} \int_{-\infty}^{\infty} \langle f|H(t)|i\rangle e^{i\omega t} dt \qquad \text{(II-7)}$$

where $H(t)$ is the interaction energy and

$$\omega = \frac{\Delta E}{\hbar} = \frac{E_f - E_i}{\hbar} , \qquad \text{(II-8)}$$

is the nuclear frequency associated with the excitation energy $\Delta E$.

For particle velocities small compared with that of light, the principal interaction is the Coulomb energy

$$H_E(t) = \int \rho_N(\vec{r}) \phi(\vec{r},t) d\tau, \qquad \text{(II-9)}$$

where

$$\phi(\vec{r},t) = \frac{Z_1 e}{|\vec{r} - \vec{r}_p(t)|} - \frac{Z_1 e}{\vec{r}_p(t)} \qquad \text{(II-10)}$$

and where $\rho_N(\vec{r})$ is the nuclear charge density operator. $\phi(\vec{r},t)$ is the electric potential at the point $\vec{r}$ due to the projectile. The projectile is considered as a point charge and its position vector $\vec{r}_p(t)$ is measured from the nuclear center of mass. In Equation (II-10) the interaction between the mass centers has been subtracted since

it is responsible for the scattering and does not contribute to the excitation.

$\phi(\vec{r},t)$ may then be expanded in a multipole expansion and $\rho$ expressed in terms of proton point charges and substituted into Equations (II-7) and (II-9). The $b_{if}$ obtained are used in Equations (II-6) and (II-4) to derive a relation for the electric differential cross section $d\sigma_{E\lambda}$ for a transition of multipole order $E\lambda$. The differential cross section may thus be written[11]

$$d\sigma_{E\lambda} = \left(\frac{Z_1 e}{\hbar v}\right)^2 a^{-2\lambda+2} B(E\lambda) df_{E\lambda}(\theta,\xi) \qquad \text{(II-11)}$$

where

$$B(E\lambda; I_i \rightarrow I_f) = (2I_i + 1)^{-1} |\langle I_i || M(E\lambda) || I_f \rangle|^2. \qquad \text{(II-12)}$$

Equation (IIA.18) of Alder et al.[11] further defines $B(E\lambda)$ as the reduced transition probability for an electric transition of multipole order $E\lambda$. The quantity $df_{E\lambda}(\theta,\xi)$ (the differential excitation function) is given by Equation (IIA.29) of Alder et al.[11] The dimensionless quantity $\xi$ is defined by Equation (IIA.27) of Alder et al.[11] as

$$\xi = \frac{a\Delta E}{\hbar v} = \frac{Z_1 Z_2 e^2}{\hbar v} \frac{\Delta E}{2E} \qquad \text{(II-13)}$$

where E and $\Delta E$ denote the incident energy of the projectile and the nuclear excitation energy, respectively. It is to be noted that

all of the angular dependence of P is contained in $df_{E\lambda}(\theta,\xi)$ and all of the dependence on nuclear properties in $B(E\lambda)$. The functions $df_{E\lambda}$ have been tabulated by Alder et al.,[11] for $\lambda = 1$ and 2 and presented graphically for $\lambda = 3$ and 4.[23]

The total excitation cross section of order $E\lambda$ is obtained by integration over all scattering directions and is given by

$$\sigma_{E\lambda} = \left(\frac{Z_1 e}{\hbar v}\right)^2 a^{-2\lambda+2} B(E\lambda) f_{E\lambda}(\xi) \qquad \text{(II-14)}$$

where the total excitation functions $f_{E\lambda}(\xi)$ have been evaluated classically for E1, E2, E3, and E4 excitations by Alder and Winther.[24] The effective interaction strength parameter $\eta$ is taken to be infinite in the classical case for very slow projectiles. The total excitation function $f_{E2}(\eta,\xi)$ has also been evaluated quantum-mechanically as a function of $\xi$ and $\eta$.[11,25,26,27] Alder et al. have evaluated the quantum-mechanical corrections to the classical f functions[11] and have shown that the quantal corrections are small for $\eta \gtrsim 8$. For $\eta \gtrsim 8$ the particle orbits are essentially Rutherford orbits for $\lambda = 1$ and 2. Most Coulomb excitation experiments require only the E2 (electric quadrupole) process to accurately describe the excitation. The M1 (magnetic dipole) cross section is usually several orders of magnitude smaller than the E2, and E1 and E3 modes are less frequently observed in Coulomb excitation.

For a direct E2 Coulomb excitation process the cross section can be written as

$$\sigma_{E2} = \left(\frac{Z_1 e}{\hbar v_i}\right)^2 a^{-2} B(E2; I_i \rightarrow I_f) f_{E2}(\eta_i, \xi), \qquad \text{(II-15)}$$

where,

$$a \equiv Z_1 Z_2 e^2 / m_o v_i v_f, \qquad \text{(II-16)}$$

and

$$\xi \equiv \frac{Z_1 Z_2 e^2}{\hbar} \left(\frac{1}{v_f} - \frac{1}{v_i}\right). \qquad \text{(II-17)}$$

The subscripts i and f refer to initial and final values. Alder et al.[11] have given these symmetrized definitations of a and $\xi$ to more accurately account for the energy exchange during the collision. The symmetrized total cross sections reproduce the quantum mechanical cross section to within a few percent, for values of $\eta$ as low as 3 and $\xi$ as large as 2.[11] This describes a collision in which the particle loses more than one-half its kinetic energy and for which the unsymmetrized cross sections would be in error by more than a factor of one hundred. Equation (II-15) can be cast into a more convenient form by evaluating several of the numerical factors and is given by

$$\sigma_{E2}(cm^2) = 4.782 \times 10^{24} \frac{A_1}{Z_2^2} \left(\frac{A_2}{A_1 + A_2}\right)^2 (E - \Delta E') \frac{B(E2)}{e^2} f_{E2}(\eta,\xi), \tag{II-18}$$

where E (MeV) is the energy of the projectile in the laboratory system, $A_1$ and $A_2$ (in amu) are the masses of the projectile and target, $Z_1$ and $Z_2$ are the atomic numbers of the projectile and target, $\Delta E' = (1 + A_1/A_2)\Delta E$, and $\Delta E$ (MeV) is the excitation energy of the nucleus. The quantity B(E2) is given in units of $e^2cm^4$.

## C. CALCULATION OF THE REDUCED TRANSITION PROBABILITY

In these experiments a beam of charged α particles has been used to Coulomb excite the tin nuclei. For this reaction the number of nuclear excitations can be expressed as

$$NEX = \frac{N\rho B}{A_2} \int_0^x \sigma_{E2}(E)dx', \tag{II-19}$$

where B is Avogadros' number, ρ is the mass density of the target, $A_2$ is the atomic weight of the target, N is the number of projectiles which strike the target, $\sigma_{E2}(E)$ is the Coulomb excitation cross section in $cm^2$, and x is the target thickness. Following the development of Milner[28] the integration over target thickness may be replaced by an integration over projectile energy by noting that

$$\rho dx = \frac{\rho dE}{dE/dx} = \frac{dE}{dE/d\rho x} = \frac{dE}{S(E)}, \qquad \text{(II-20)}$$

where $S(E) \equiv dE/d\rho x$ is the rate of energy loss of the projectile in the target. Substituting Equations (II-19) and (II-20) into Equation (II-18) we may express B(E2) in terms of the number of Coulomb excitations NEX of the state under consideration and an integral of the energy dependent part of the cross section over the target thickness. The expression for B(E2) is given by

$$\frac{B(E2;J_i \rightarrow J_f)}{e^2} = 5.556 \times 10^{-59} \frac{AnZ_2^2}{A_1 K^2} \frac{I(exc./\mu c)}{\int \frac{f_{E2}(\eta_i,\xi)(E - \Delta E')dE}{S(E)}}, \qquad \text{(I-21)}$$

where $K = A_2/(A_1 + A_2)$ and I(exc./μc) is the number of nuclear excitations per particle microcoulomb of projectiles. The stopping power is expressed in units of MeV·cm$^2$/mg. The atomic weight of the normal element An is used because the density of the normal element was used in the stopping power $dE/d\rho x$.

A computer program DIREKE2 has been developed by Milner[28] which numerically evaluates the thick target integral in the denominator of Equation (II-21) as well as the thick target particle parameters $(a_2)_t$ and $(a_4)_t$. The thick target particle parameters are used in the angular anisotropy section. Required

input data for the program includes tables of the functions $f_{E2}(\eta_i,\xi)$, $a_2(\eta_i,\xi)$, and $a_4(\eta_i,\xi)$ which are given in Tables II.5, II.9, and II.10 of Alder et al.[11] A table or set of parameters for the stopping power of the projectile in the target is also required.

## D. ANGULAR DISTRIBUTION OF THE DE-EXCITATION GAMMA-RAYS

The angular distribution to be described refers to a correlation of the de-excitation $\gamma$ rays with the direction of the incident beam of projectiles. This is similar to the case in which the direction of emission of the first member of a pair of cascade $\gamma$ rays defines the quantization axis about which the second $\gamma$ ray is correlated as illustrated in Figure 2. The theory of this angular correlation process has been well developed by Biedenharn and Rose[30] and by Rose and Brink[31] among others. In this process unless $\eta_i$ is very large ($\gtrsim 20$),[29] the angular distribution of the de-excitation gamma radiation must be treated quantally. The work of McGowan and Stelson[18] has demonstrated experimentally that the semi-classical calculation of the $\gamma$ ray angular distribution is not always accurate. An accurate and complete quantum-mechanical derivation of this angular distribution has been formulated by Biedenharn et al.,[32] Breit et al.,[33] and by Alder et al.[11] Anisotropies in the radiation pattern arise from the fact that certain magnetic substates of the nucleus are preferentially populated in the excitation process. The relative population of

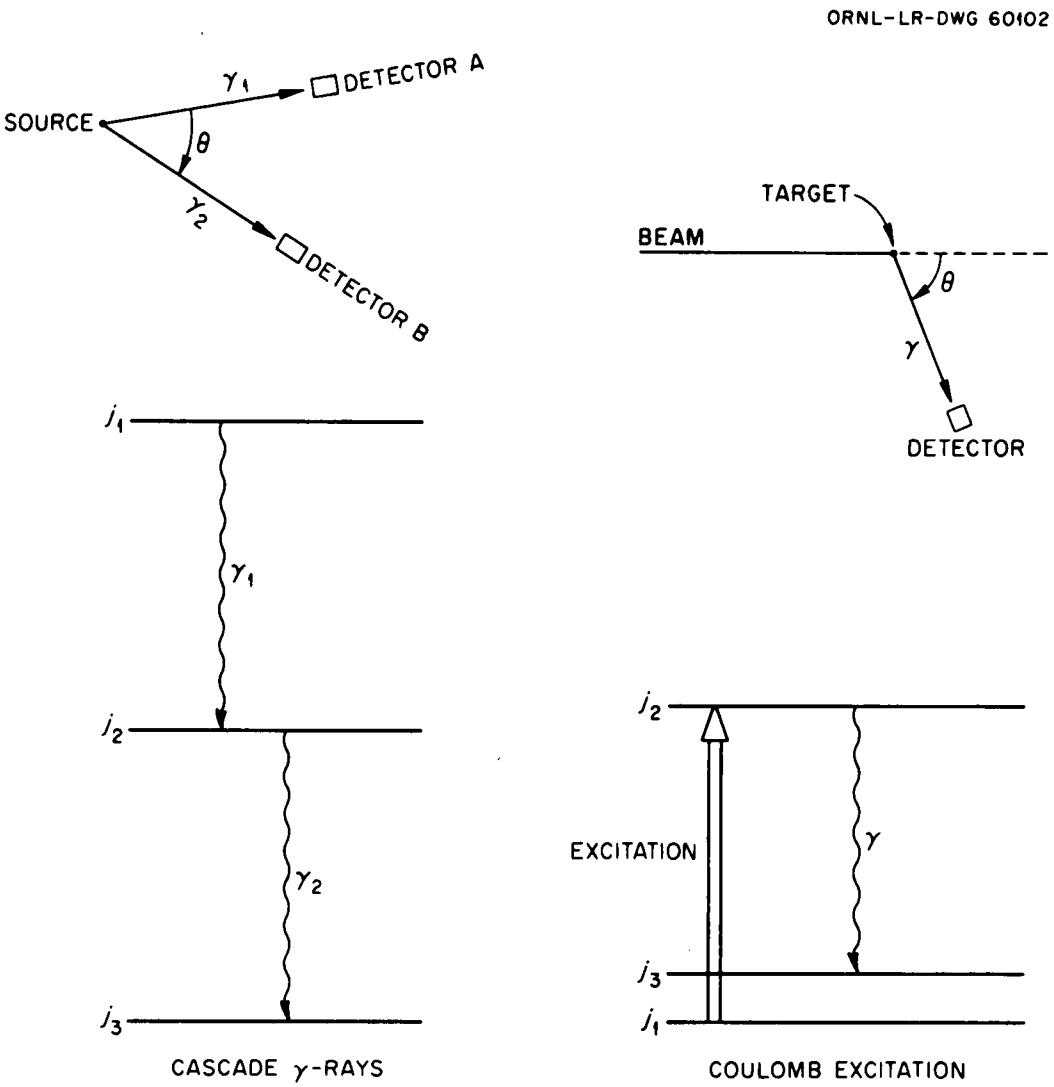


Figure 2. Analogy between cascade γ-ray and Coulomb excitation angular distributions.

the magnetic substates depends on the multipolarity of the excitation process. The observed radiation intensity distribution is then a result of the weighted sum of the patterns from all of the various radiating substates.

If the first transition has a pure multipolarity $\lambda$, the $\gamma$-$\gamma$ correlation may be written

$$W(\theta) = \sum_k A_k^{(\lambda)} P_k(\cos\theta), \qquad \text{(II-22)}$$

where the $A_k^{(\lambda)}$ are coefficients which depend on the spins ($j_1$, $j_2$, and $j_3$) and the multipolarities of $\gamma_2$ and where the $P_k(\cos\theta)$ are Legendre polynomials.

If the scattered projectiles are not observed then the angular distribution of the de-excitation $\gamma$ rays following direct E2 Coulomb excitation can be expressed as (Equation IIB.83, Alder et al.[11])

$$W(\theta_\gamma) = 1 + a_2^{E2}(\eta_i,\xi)A_2^{(2)}P_2(\cos\theta_\gamma) + a_4^{E2}(\eta_i,\xi)A_4^{(2)}P_4(\cos\theta_\gamma). \qquad \text{(II-23)}$$

The $a_k^{E2}$ are the particle parameters which characterize the Coulomb excitation process and the $A_k^{(2)}$ are the same coefficients that appear in Equation (II-22). For the practical case where large detectors and thick targets are involved the angular distribution of Equation (II-23) can be expressed as

$$W(\theta) = 1 + (a_2)_t A_2 g_2 P_2(\cos\theta) + (a_4)_t A_4 g_4 P_4(\cos\theta), \qquad (II\text{-}24)$$

where $(a_2)_t$ and $(a_4)_t$ denote particle parameters averaged over the thick target and $g_2$ and $g_4$ are the finite solid angle correction factors which account for the fact that the detector extends over a finite solid angular range. Milner's program DIREKE2[28] calculates the thick target particle parameters using a quantum mechanically correct particle parameter table from Alder et al.[11] Milner[28] has also developed a program for calculating the $g_2$ and $g_4$ using detector geometry input data.

The Coulomb excitation of a given level is usually by the pure E2 process. The de-excitation $\gamma$ rays are mixtures of M1 and E2 radiations if the selection rules permit both multipolarities. For mixed radiation the $A_2$ and $A_4$ are functions of the amplitude ratio $\delta = (E2/M1)^{1/2}$ in addition to the spins.

# CHAPTER III

## NUCLEAR MODELS

### A. THE COLLECTIVE MODEL

The tin isotopes are particularly well suited to provide information about the 50-82 neutron shell. In tin, the protons form a closed shell (Z = 50) thus making the neutron spectrum relatively simple. The large number of tin isotopes provide many nuclei for study, so that trends can be observed as the neutron shell is filling. In addition the tin isotopes are typical spherical vibrational nuclei and are thus particularly interesting to study from a shell model point of view.

For the idealized case of a nucleus with constant density and a sharp surface, the coordinates $a_{\lambda\mu}$ would define the nuclear surface by

$$R(\theta,\phi) = R_o \{1 + \sum_{\lambda\mu} a_{\lambda\mu} Y_{\lambda\mu}(\theta,\phi)\}, \qquad \text{(III-1)}$$

where $\theta$ and $\phi$ are polar angles with respect to arbitrary axes, $R_o$ is the equilibrium radius, and $Y_{\lambda\mu}(\theta,\phi)$ are the normalized spherical harmonics, of order $\lambda,\mu$. The nuclear collective coordinates $a_{\lambda\mu}$ describe the spatial distribution of the nucleon density which, in turn, defines the nuclear field. For this nuclear system, which is assumed to have small compressibility, the collective degrees of freedom which have the lowest energies are associated with deformations in shape with approximate preservation of volume.

Any collective motions are expressed by letting $a_{\lambda\mu}$ vary with time. In the quadratic approximation, the kinetic energy is of the form[34]

$$T = \frac{1}{2} \sum_{\lambda,\mu} B_\lambda |\dot{a}_{\lambda\mu}|^2, \tag{III-2}$$

where the coefficient $B_\lambda$ is associated with the mass transported by the collective flow and depends on the velocity field. Also the potential energy may be written

$$V = \frac{1}{2} \sum_{\lambda\mu} C_\lambda |a_{\lambda\mu}|^2. \tag{III-3}$$

Thus the surface Hamiltonian may be written

$$H_s = \sum_{\lambda\mu} \left\{ \frac{1}{2} B_\lambda |\dot{a}_{\lambda\mu}|^2 + \frac{1}{2} C_\lambda |a_{\lambda\mu}|^2 \right\}, \tag{III-4}$$

where the deformation energy has been expanded around the equilibrium ($a_{\lambda\mu} = 0$). In the first approximation, the Hamiltonian, $H_s$, represents a set of harmonic oscillators with frequencies

$$\omega_\lambda = \sqrt{\frac{C_\lambda}{B_\lambda}}. \tag{III-5}$$

For oscillations of the surface described by Equation (III-1) the collective flow has the same velocity field as for the oscillations of an incompressible classical liquid drop. In this case[35]

$$a_{\lambda\mu} = \frac{4}{3}\frac{\pi}{A}\sum_{p=1}^{A}\left(\frac{r_p}{R_o}\right)^{\lambda} Y^*_{\lambda\mu}(\theta_p,\phi_p) \qquad \text{(III-6)}$$

for the collective parameters in terms of the polar coordinates $(r_p, \theta_p, \phi_p)$ of the individual particles. For pure surface oscillations described by the coordinates of Equation (III-6), one obtains the classical hydrodynamical expression

$$(B_\lambda)_{\text{irrotational}} = \frac{1}{\lambda}\frac{3}{4\pi} AMR_o^2, \qquad \text{(III-7)}$$

where M is the nucleon mass.

The coefficient $C_\lambda$ has been given by Lord Raleigh[36] for the classical liquid drop under surface tension as

$$C_\lambda^{(1)} = SR_o^2(\lambda - 1)(\lambda + 2), \qquad \text{(III-8)}$$

where S is the surface tension. For a charged liquid drop, the Coulomb energy is reduced by the distortion and a modified $C_\lambda$ is given by

$$C_\lambda = (\lambda - 1)(\lambda + 2)R_o^2 S - \frac{3}{2\pi}\frac{\lambda - 1}{2\lambda + 1}\frac{Z^2e^2}{R_o}, \qquad \text{(III-9)}$$

where Ze is the nuclear charge. The coefficient $C_\lambda$ represents the nuclear deformability. An analysis of the nuclear binding energies leads to the estimate[35] $4\pi R_o^2 S = 15.4A^{2/3}$ MeV. It will be noted

that $\omega_\lambda = 0$ for $\lambda = 0$ (where $B_\lambda \to \infty$) and for $\lambda = 1$ (where $C_\lambda = 0$). A $\lambda = 1$ oscillation (dipole) corresponds to a mode in which the neutrons and protons move with respect to each other. These oscillations are of special interest for the nuclear photo-effect, but because of their large frequencies, are unimportant for the low energy phenomena considered here. The $\lambda = 0$ corresponds to a nuclear breathing mode of higher energy. These $\lambda = 0, 1$ modes will not be considered further. Spherical nuclear shape oscillations, which have been described here, may be classified according to their multipole order $\lambda$. The excitation quanta, $\hbar\omega_\lambda$, called phonons, have total angular momentum $\lambda$, parity $(-1)^\lambda$ and may be further described by their component of angular momentum $\mu$ along a space fixed axis.

For the low energy spectrum of an odd-A nucleus, such as $^{115}Sn$, one must consider the intrinsic degrees of freedom of the nucleons as well as the collective motion. The intrinsic motion possesses a nonvanishing angular momentum which must be combined with the collective angular momentum. In addition, low-lying intrinsic excitations may arise from the change of orbital of the last odd nucleon. In this phenomena, the intrinsic nucleonic degrees of freedom are coupled to the collective oscillations, since the latter involve variations in the nuclear field. The effect of the coupling of intrinsic degrees of freedom to the quadrupole vibrations depends on the parameter[11]

$$q = \left(\frac{5}{16\pi}\right)^{1/2} \frac{k}{(\hbar\omega_2 c_2)^{1/2}}, \qquad \text{(III-10)}$$

where k is the coupling constant of the order of magnitude of the average potential energy of a nucleon. Thus the coupling is expected to increase, as one moves away from closed shell regions, as a consequence of the decrease of the effective surface tension and of the vibrational frequencies.

If the coupling of intrinsic to collective motion could be neglected, one would obtain for each intrinsic state, a collective spectrum corresponding to the phonon excitations. The collective states most strongly excited in the Coulomb excitation[11] are the one phonon quadrupole excitations of the ground state configuration. For a ground state spin of $I_o$ the excited states would have spins $I_o + 2$, $I_o + 1$, ... $|I_o - 2|$ and energies of the same order of magnitude as the first excited state in the neighboring even-even nuclei.

The vibrational excitations are characterized by enhanced electric transition probabilities. These transition probabilities can be expressed directly in terms of the parameters $B_\lambda$ and $C_\lambda$. Thus, for the one phonon excitation one obtains[11]

$$B(E\lambda;\ I = 0 \rightarrow I = \lambda)_{ph} = (2\lambda + 1)\left(\frac{3}{4\pi}ZeR_o^{\lambda}\right)^2 \frac{\hbar}{2(B_\lambda C_\lambda)^{1/2}} . \qquad \text{(III-11)}$$

The reduced transition probability for the excited states of the coupled system is given by[11]

$$B(E2;\ I_o \rightarrow I_f) = \frac{1}{5}\frac{2I_f + 1}{2I_o + 1} B(E2)_{ph}, \qquad \text{(III-12)}$$

where $B(E2)_{ph}$ is the quadrupole phonon excitation given by Equation (III-11).

Alder et al.[11] have calculated the coupling q for a wide range of nuclei based on empirical vibrational parameters and have found values between 1 and 3 for most nuclei. With such values of the coupling parameter the stationary states represent a rather complicated superposition of individual particle and collective motions. In a few nuclear regions ($A \sim 20$, 75, 105, 150, and 192), one obtains especially strong couplings of $q \gtrsim 4$. For such strong coupling, the last odd nucleon may appreciably polarize the nuclear shape with a resulting approach to the rotational coupling scheme characteristic of deformed nuclei.[11]

For the cases of very weak or very strong coupling the dominant quadrupole transitions are associated with a few simple excitations. In the case of intermediate coupling the spectrum is more complex, but there exists an approximate sum rule which is useful in the analysis of such spectra. The rule states that the summed quadrupole strength $\sum_f B(E2;\ I_o \rightarrow I_f)$ obtained by adding all the low energy transitions (i.e. with energies less than a few times $\hbar\omega_2$) is proportional to the average value of $\beta^2$ in the nuclear ground state, aside from a small contribution due to the quadrupole

transitions of the last odd nucleon, where the quantity $\beta^{34}$ is a measure of the total deformation of the nucleus. The sum is, therefore, expected to be approximately the same in odd-A nuclei as in neighboring even-even nuclei, except insofar as the last particle polarizes the nucleus and thereby increases the sum. When the sum for an odd A nucleus is appreciably smaller than the B(E2; $0 \rightarrow 2$) for the first excited state of an adjacent even-even nucleus, one may conclude that there exists strong quadrupole transitions which have yet to be detected. A sum greatly exceeding this value implies an appreciable polarization produced by the last particle.

## B. SHELL MODEL CALCULATIONS

Guided by many successes in the description of the periodic nature of the chemical properties of the elements in terms of the shell model of the atom, early nuclear physics workers applied this type of model to nuclei. For the nucleus there is a strong similarity and at the same time an important difference with the atomic case. For on the one hand, the nuclear constituents are neutrons and protons which are Fermi-Dirac particles, but on the other hand no single interaction acts on all the nucleons so strongly that their mutual interactions can be neglected. It happens that a considerable body of experimental evidence has accumulated which strongly suggests that nuclei do possess a shell structure of some kind. In the nuclear shell model it is assumed to first order that the nucleons move independently in a mean nuclear

potential produced by all the other nucleons. This model has been modified in many different ways in order to improve the model predictions. The simple shell model is able to account for many nuclear phenomena, many of which are periodic with nucleon number. The main properties which show such a variation are the absolute abundances of the various nuclides, the magnitudes of the electric quadrupole moments, the nuclear stability, and the distribution of the lowest-lying nuclear excited states.[37] These properties show significant variations with the nucleon number Z (protons) or N (neutrons) and have pronounced variations at the "magic" nucleon numbers 2, 8, 20, 50, 82, and 126. In one model which will produce these "magic" numbers each nucleon is assumed to move inside a spherically symmetric square-well potential due to the average affects of all the remaining nucleons. In order to obtain the magic numbers this simple potential was modified by the addition of a spin-orbit potential at the suggestion of Meyer[38] and Haxel, Jensen, and Suess.[39] This results in a splitting of the $j = \ell \pm 1/2$ levels. The choice of the sign of the radial part f(r) of the spin orbit potential

$$- f(r)(\vec{\ell} \cdot \vec{s}), \qquad \text{(III-13)}$$

where $\vec{s}$ is the intrinsic nucleon spin, and $\vec{\ell}$ the orbital angular momentum, is such that the $j = \ell + 1/2$ level is depressed relative to the $j = \ell - 1/2$ level.

Meyer and Jensen[40] have calculated the effect of spin-orbit coupling on the level system of a well of a shape intermediate between the square and oscillator wells. The results are plotted in Figure 3, which displays the shell closures at the magic numbers 2, 8, 20, 50, 82, and 126.

Kuo and Baranger[3] have used a shell model Hamiltonian with a residual two-nucleon interaction of Gaussian form to calculate the states of the odd-mass tin isotopes. In their work the Bogolyubov-Valatin quasi-particle transformation was made and the residual interaction diagonalized in a one- and three-quasi-particle space with spurious states being projected out. Various approximations to this procedure, such as perturbation theory and a phonon approximation were studied. Perturbation theory was found to be adequate for the low energy states. The phonon approximation was found to be correct qualitatively, but not quantitatively. The parameters of the residual interaction and the single-particle energies were determined by requiring good agreement with the experimental energies. Magnetic moments, electromagnetic transition rates and spectroscopic factors were calculated and found to be in good agreement with experimental values. These calculations would have been prohibitively complicated if accomplished using standard shell model calculations. What made them possible was the use of ideas borrowed from the BCS theory of superconductivity.

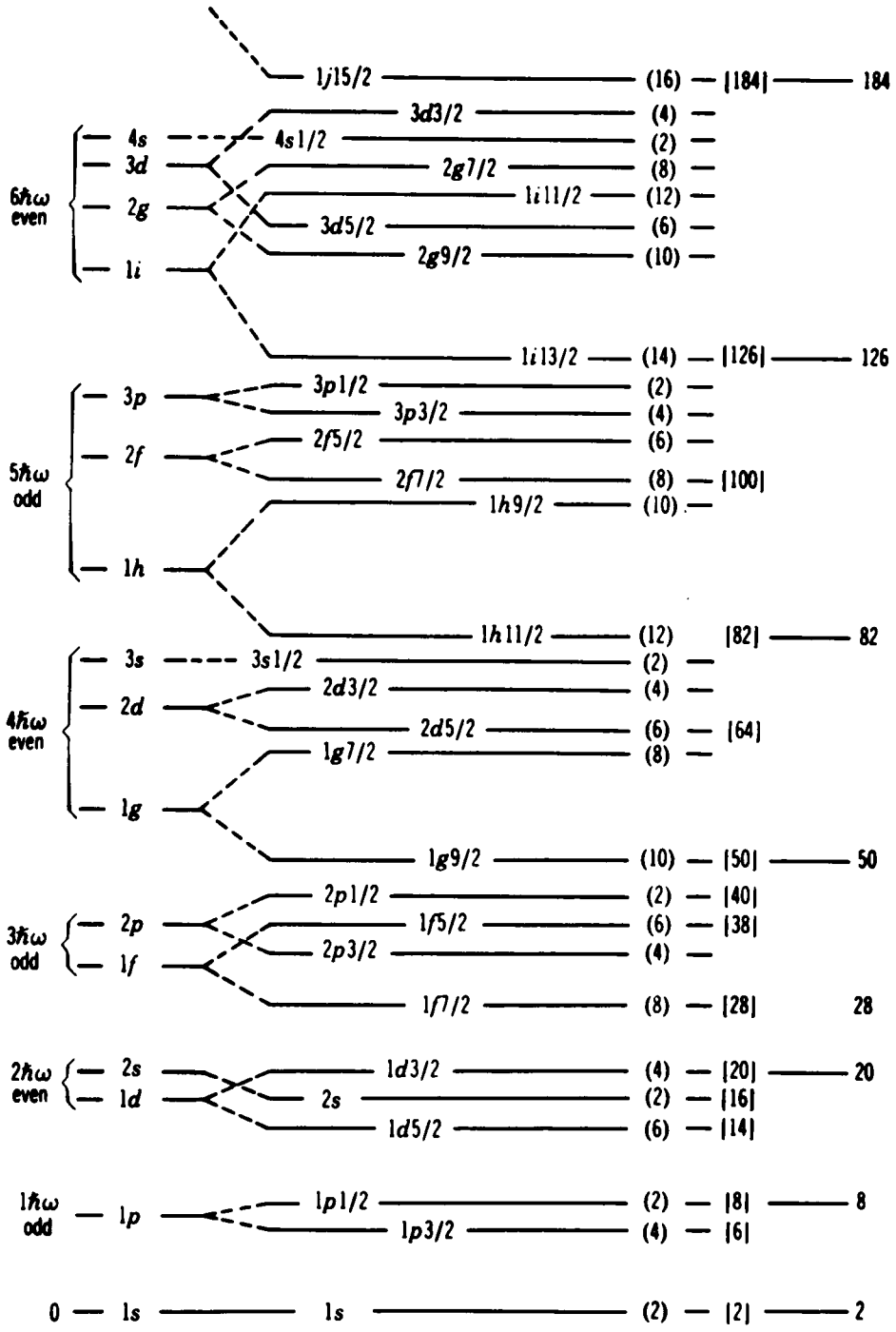


Figure 3. Effect of spin-orbit coupling on the level system of a well of a shape intermediate between the square and oscillator wells. The number of particles of one kind (neutrons or protons) in the various shells are indicated in parenthesis. The accumulating numbers are given in square brackets (Mayer and Jensen[40]).

# CHAPTER IV

## EXPERIMENTAL ARRANGEMENT AND PROCEDURE

Gamma-ray singles, $\gamma$-ray angular anisotropy, $\gamma$-$\gamma$ coincidence, and inelastic alpha scattering experiments were performed in this research. The $\gamma$-ray singles experiments included yields, angular anisotropies, and Doppler shifted peak shape lifetimes for the Coulomb excitation study. All of the research was carried out using the ORNL MODEL EN Tandem Van de Graaff accelerator. Section A describes the tandem Van de Graaff facility and associated experimental computer data handling facilities. Section B describes the Enge split pole magnetic spectrograph facility, which was used to measure the inelastic $\alpha$ spectrum from the $^{115}Sn(\alpha,\alpha')^{115}Sn$ reaction in order to provide an independent measurement of the $B(E2)_{ex}$. Section C describes the germanium lithium-drifted (Ge(Li)) detectors which were used in the $\gamma$-ray measurements. Section D describes the $\gamma$-ray singles experiments for yield determinations. Section E describes the $\gamma$-ray angular anisotropy measurements which were used in determining the spin and parity values for the $^{115}Sn$ states measured. Section F describes the $\gamma$-$\gamma$ coincidence measurements which were used in establishing the $^{115}Sn$ level structure. Section G describes the Doppler shift lifetime measurements on the $^{115}Sn$ states. And finally, Section H describes the target preparation techniques and equipment used in the fabrication of the high purity $^{115}Sn$ targets.

## A. TANDEM VAN DE GRAAFF BEAM FACILITY AND COMPUTER DATA HANDLING EQUIPMENT

All of this research was carried out using the ORNL Tandem Van de Graaff accelerator. This accelerator is a standard model EN Tandem designed and fabricated by the High Voltage Engineering Corporation. Oxygen-16 and α particle beams from this accelerator were used to Coulomb excite the isotopically enriched $^{115}Sn$ targets. Figure 4 shows a schematic illustration of the arrangement for Coulomb excitation with the Tandem accelerator. For the production of α particle beams, positive ions are produced in a duoplasmatron ion source[41] and are then accelerated to some tens of kilovolts before being passed through a Ca vapor electron donor canal. The $\alpha^+$ ions collide with the neutral Ca vapor which supplies electrons to a small fraction of the α-ions forming $\alpha^-$ ions. These high speed $\alpha^-$ ions are then further accelerated by some 70 keV and then transported to the entrance of a 20° analyzing magnet. The 20° analyzing magnet is set to select the $\sim$ 90 keV $\alpha^-$ beam and focus it on the entrance to the low energy terminal of the Tandem Van de Graaff. Oxygen -16 negative ions were produced directly by a thermionic cesium sputter ion source. Cesium ions were produced thermionically from a hot sintered tungsten surface and then accelerated to some 20 keV. This high speed beam of $Cs^+$ ions then struck a sputter cone of $Al_2O_3$ where $^{16}O^-$ ions were sputtered off and then accelerated. Again, the mixed beam of ions was analyzed by

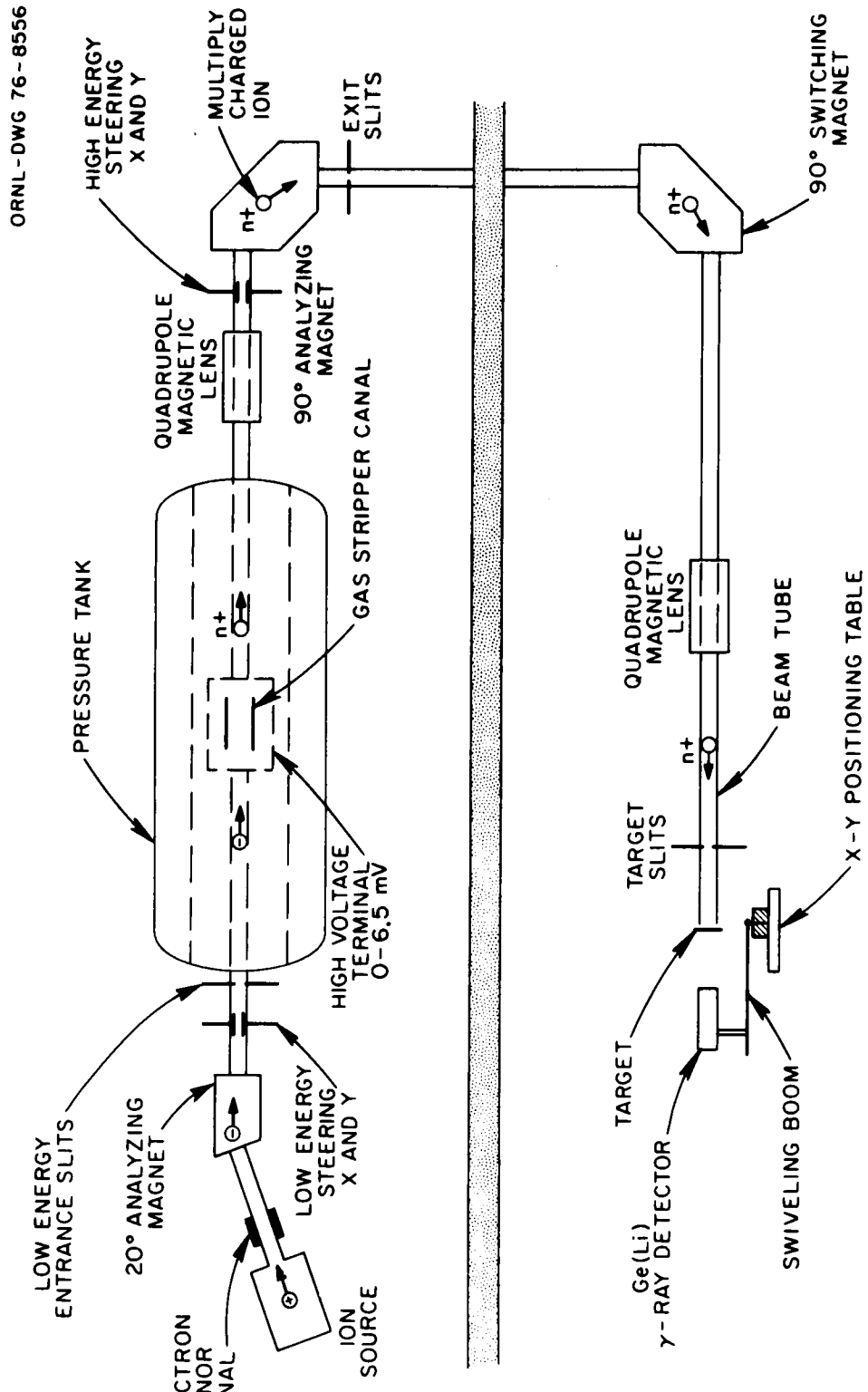


Figure 4. Schematic illustration of the arrangement for Coulomb excitation with the Tandem accelerator.

the 20° magnet and transported and focused onto the low energy terminal of the Van de Graaff accelerator.

From the low energy terminal the singly charged negative ions are further accelerated by some +3.3 MV for the $\alpha^-$ particles and +6.4 MV for $^{16}O^-$ particles. These high speed ions then pass through a low-pressure Ar gas-filled stripper at the Tandem high voltage terminal where several electrons are removed thus producing a spectrum of positively charged ions. These positive ions are then further accelerated by the terminal voltage to the ground potential high energy terminal. The correct charge state is selected by the precision field regulated 90° analyzing magnet. In our case it was $\alpha^{++}$ at 10 MeV and $^{16}O^{6+}$ at 45 MeV. The terminal voltage is regulated by the Corona current method and by adjusting the charging current on the Van de Graaff charging belt. A differential current signal from the 90° analyzing magnet exit slits is amplified and used to vary the charging current to keep the beam centered on the exit slits.

A 90° switching magnet is used to deflect the high energy beam onto the target. Good ion optical adjustments are very important for getting high current beams and for minimizing slit scattering off of defining aperatures and other beam line structure. Low energy optical adjustments are provided by the ion source electrode potentials and arc discharge parameters, by low energy steering, and by the low energy entrance slits. High energy optical adjustments are provided by the two quadrupole magnetic lenses, by the exit slits, and by the high energy X and Y steering. The beam was

generally transported to the target with the target slits open and maximized. The target slits were then pulled in and the beam refocused to maximize the current on target. Generally the target slits were then withdrawn to minimize the 136.25 keV $\gamma$-ray production on the tantalum slits for $\gamma$-ray work and to minimize slit scattering and thus greatly raise the peak to background values for the Enge inelastic spectrum. Peak to background values of $\sim$ 10,000 were raised to $\sim$ 50,000 on one Enge inelastic spectrum by spending several hours on optical alignment. Another experimental leg similar to the one illustrated in Figure 4 was selected by rotating the 90° switching magnet through $\sim$ 120°. This leg directed the beam into the scattering chamber of the Enge split pole magnetic spectrograph. The ion exit slits at the analyzing magnet were generally adjusted so that the beam energy was known to within $\sim$ 0.2%.[29] The 90° analyzing magnet was previously calibrated using known reaction threshholds, and its magnetic field was monitored continuously with a nuclear magnetic resonance probe.

The data handling facilities at the Tandem accelerator consist of a PDP-11/45 based Tennecomp PACE analyzer system which is linked to a local CDC-3200 computer. The PDP-11/45 system is equipped with several stretchers for simultaneously gathering singles or for multiparameter spectra. It is equipped with a light-pen oscilloscope viewer so that spectra can be viewed and analyzed as they are being collected. Spectral lengths of from 512 to 8 K words can be collected through the use of hardware

plugs and software definitions. Completed runs are dumped from the PDP-11/45 system onto the CDC-3200 master disk file from where they are periodically transferred to master tape file storage. The CDC-3200 has a complete library of spectral analysis routines for analyzing run data. Temporary dumps of collecting spectra may be made for immediate analysis. The facility has four IBM tape compatible tape transports. Data can be outputed on magnetic tape for analysis with the ORNL computing facility IBM-75 and 91 computers.

## B. ENGE SPECTROGRAPH APPARATUS

Measurements of the inelastic $\alpha$ spectrum from the reaction $^{115}Sn(\alpha,\alpha')^{115}Sn$ have been made in order to provide an independent measurement of the reduced electric quadrupole transition probability for excitation, $B_{ex}(E2)$. These measurements are to be compared with the more involved in-beam $\gamma$-ray measurements of $B_{ex}(E2)$ which have also been made as part of this study.

An Enge split-pole magnetic spectrograph[42] was used in conjunction with a position sensitive proportional detector of the Borkowski-Kopp type.[43,44] The magnetic spectrograph energy analyzed the scattered $\alpha$ particles which were produced by a $\sim$ 10 MeV $\alpha$ particle beam bombardment of a 75 $\mu g/cm^2$ thin $^{115}Sn$ target. The proportional detector was located in the focal plane of the magnet and in conjunction with the electronics provided real time data display and reduction.

Enge Magnet

Figure 5 shows a schematic illustration of the Enge slit-pole magnetic spectrograph. The target is located in a small scattering chamber located on a different experimental beam leg from that shown in Figure 4. This beam leg is selected by rotating the 90° swtiching magnet. The Enge slit-pole magnetic spectrograph was developed to provide a spectrograph with a resolving power commensurate with the Van de Graaff high energy stability which is of the order of one part in $10^4$ or better.

The instrument shown in Figure 5 is called a slit-pole spectrograph because it has two separate pole pieces enveloped by a single coil. The purpose of the split between the poles of what would normally be a conventional sector magnet is to provide second-order double focusing over a broad range of energies. Vertical (transverse) ion focusing is provided in the fringing-field zones, particularly the entrance fringing field to the first pole gap. The split between the pole pieces is designed in such a way that the high-momentum particles experience larger focusing forces in moving across the split than do the low-momentum particles. In this manner it is possible to provide approximate first-order vertical focusing over a full range of momenta. With this type of magnet arrangement a larger solid angle of acceptance can be achieved which maintains resolving power by using two-directional focusing and, at the same time, second order focusing. This means that the terms of second order in the angles of acceptance vanish in the expression for the abberation at the image. The rest of the spectrograph was

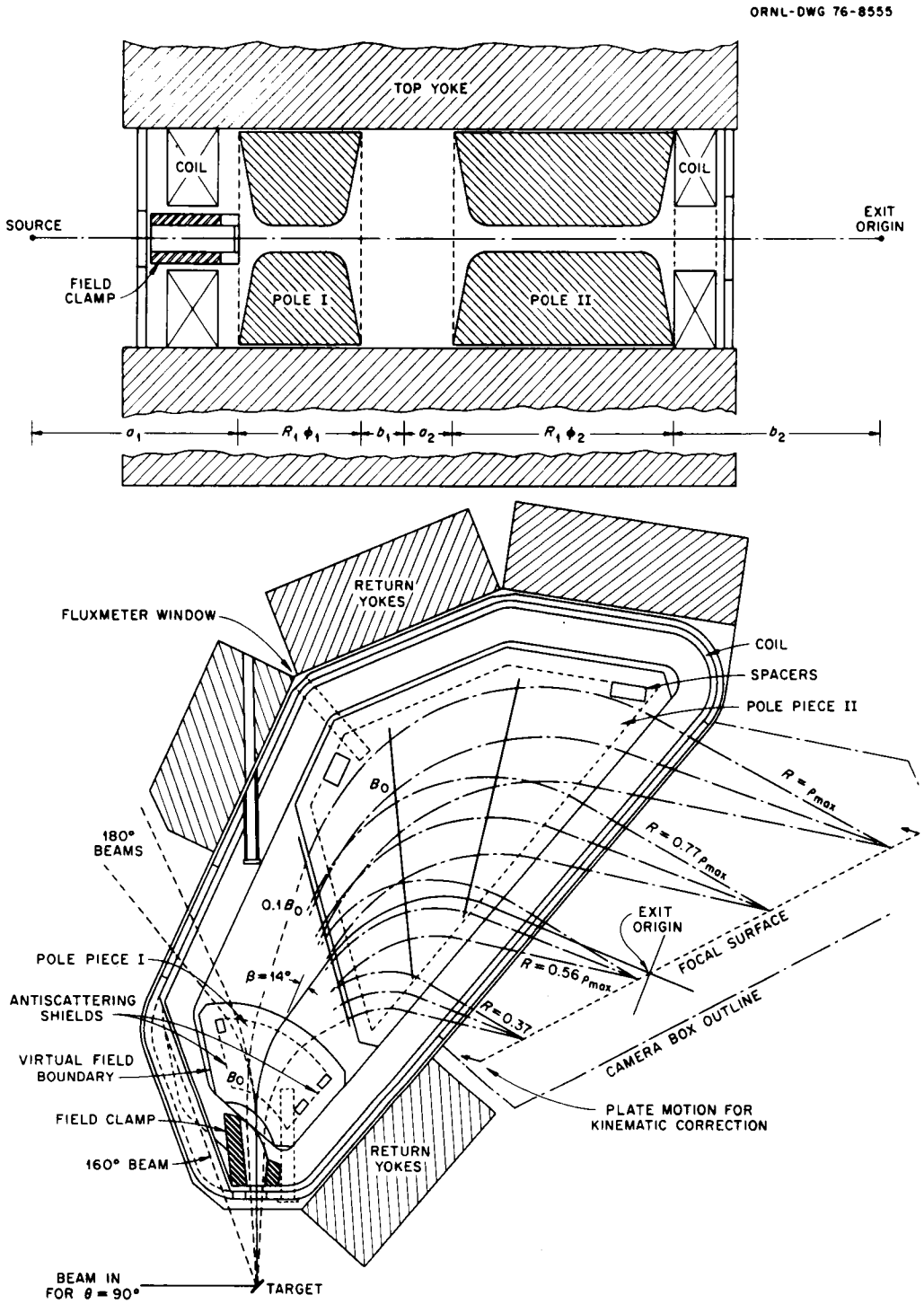


Figure 5. Schematic illustration of the Enge split-pole magnetic spectrograph.

designed to give the desired first-order focusing properties and then by a final adjustment of the position and orientation of the exit pole boundary, the second-order median-plane abberation was made exactly zero for two points on the focal surface. In the final design, the second-order abberations were quite small for the entire range of momenta. The return yoke was so designed that externally piped beams can be used to look at scattering angles up to $\theta_{lab} = 160°$. Momentum ranges of $p_{max}/p_{min} \approx 2.8$ (energy range $E_{max}/E_{min} \approx 8$) are accommodated by the spectrograph. A resolving power of better than $p/\Delta p = 5000$ has been demonstrated in the $^{106}Pd(d,p)^{107}Pd$ reaction with a 50 $\mu g/cm^2$ target and a solid angle of acceptance of 0.8 msterad.

Magnet currents, detector focal plane settings, and other parameters for initial magnet setup for a particular experimental situation were obtained using the subroutine RHO of the computer program FATRUMP.[45]

Gas Proportional Particle Detector

Several types of detectors have been used with magnetic spectrographs for recording particle spectra. The most widely used are nuclear emulsion plates, position sensitive semiconductor detectors, spark chambers, and wire proportional counters.

Nuclear (and photographic) emulsion plates have excellent position resolution and will cover the focal plane, but suffer from several disadvantages in the present type of experiment: (1) The events must be human tabulated which is very tedious and inefficient

for the large number of events required to get good statistical accuracy, and (2) the experimenter cannot observe the progress of data collection and hence change the experiment design which is in progress.

Semiconductor detectors are limited in countrate and ability to cover much of the focal plane, but do have good position resolution.

Spark chambers and multiwire proportional counters are severely limited in countrate, require a substantial electronics setup, and have poorer position resolution.

The detectors used in these experiments were a 20 cm single wire proportional counter and a 60 cm single wire proportional counter, both of the Borkowski-Kopp design.[43,44] Figure 6 is a schematic illustration of the 20 cm gas flow position sensitive proportional counter detector. The 60 cm detector is of similar design. The Borkowski-Kopp detector uses a high resistance central wire which acts as a distributed RC line. The central wire is held at ground potential and the body of the gas chamber is the cathode at $\sim$ -850 vdc potential. High gain voltage sensitive FET preamps are attached to each end of the wire inside the vacuum chamber. An aluminized Mylar window, with the three sides of the body, defines the electric field region. A second Mylar window is used to maintain the low pressure gas mixture to vacuum difference to keep from distorting the electric field. A 90% argon, 10% methane mixture is kept flowing continuously through the detector.

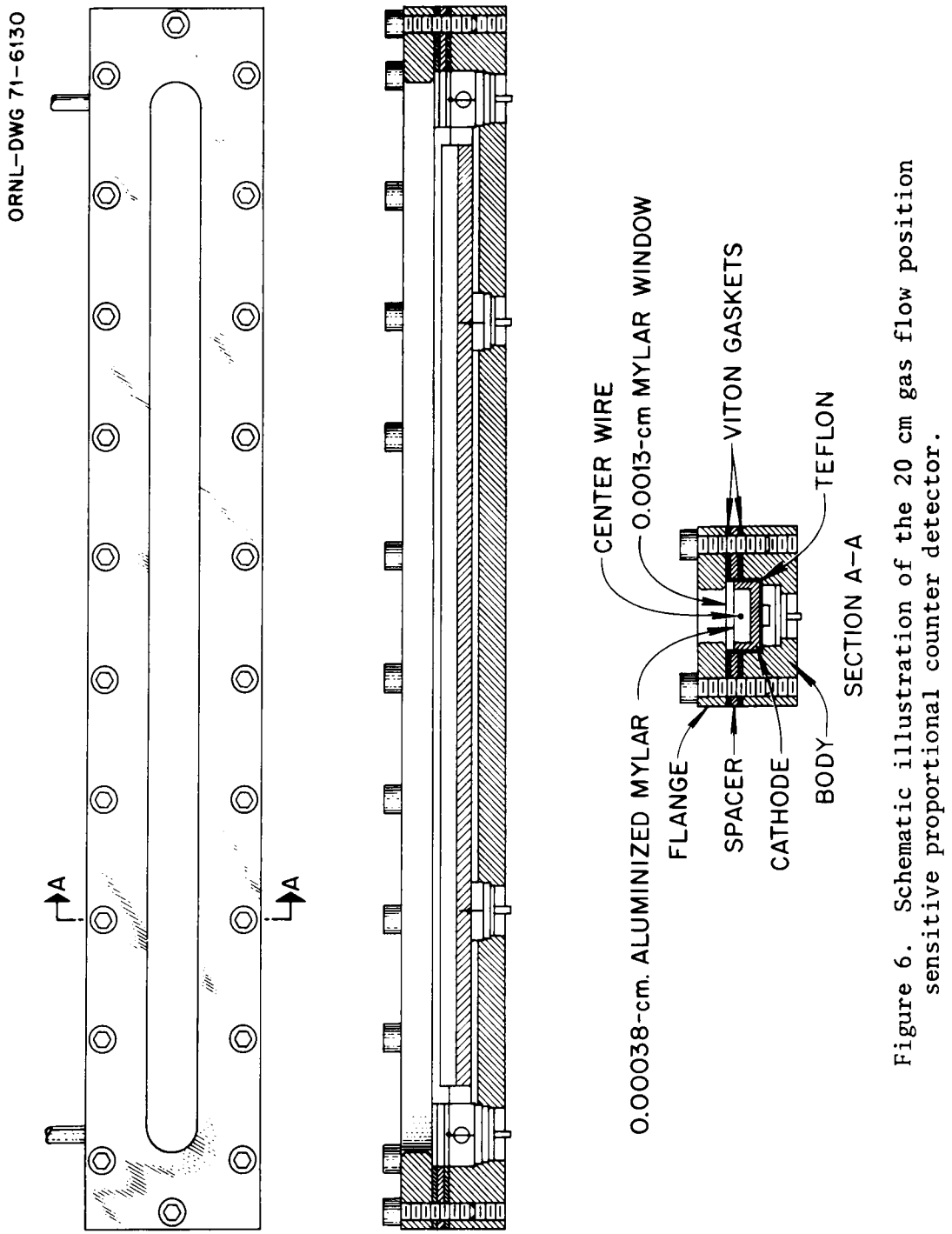


Figure 6. Schematic illustration of the 20 cm gas flow position sensitive proportional counter detector.

The electrical pulses which are generated at the point of particle impact travel to each end of the detector and have rise times that are proportional to the distances between the ends of the detector and the point of impact of the particle. The difference in rise times is measured by crossover timing to obtain the position information. In this detector a change in position of 1 mm corresponds to a change in crossover time of 30 nanoseconds. The difference in crossover time is fed to a time-to-amplitude converter. This amplitude pulse is then available for immediate analysis and storage in the multichannel analyzer. References 46 and 47 should be consulted for a detailed explanation of the theory of operation of the detector.

Figure 7 shows the schematic for the Enge magnet detector electronics which is used for measuring inelastically scattered particles in conjunction with the 20 and 60 cm detectors and Enge magnet. The pulses from the different ends of the detector are amplified and their travel time difference, which is a measure of position and thus energy, is measured by the crossover timing technique. The pulses from both ends of the detector are also summed and a window is set, via a timing single channel analyzer, on the distribution of summed pulses. Summed pulses which have the correct energy thus trigger an enabling gate for the linear gate which passes the TAC pulses. This technique reduces background contributions due to x-ray and neutron events produced by the beam stopping in the detector walls. Gated and ungated TAC signals are

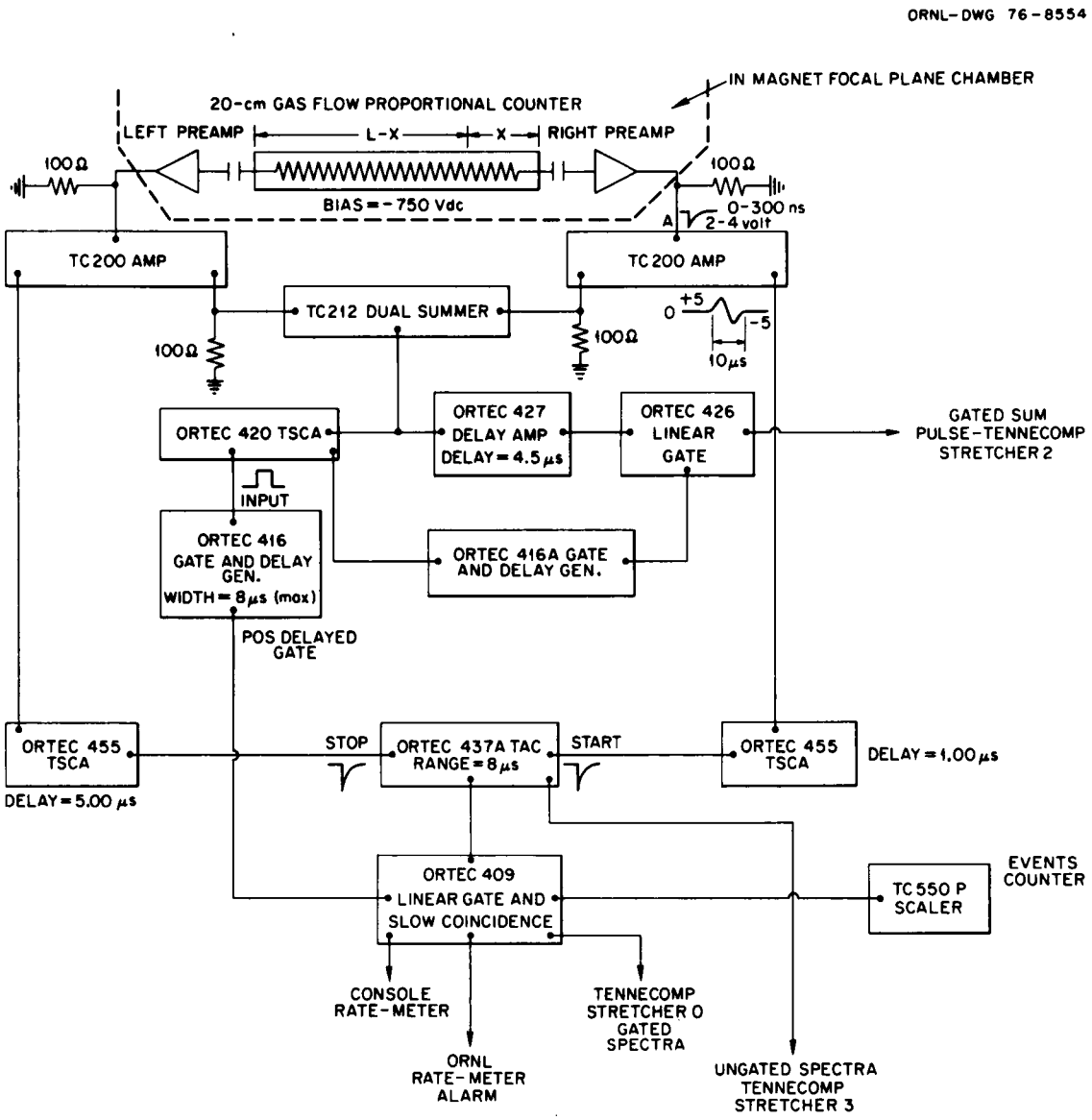


Figure 7. Enge magnet detector electronics for measuring inelastically scattered particles for the 20 and 60 cm detectors.

routed to the PACE multichannel analyzer system. The gated signal should have a better peak to background ratio, but the ungated signal is also important to test for any incorrect gating techniques.

This detector system has been used with an incident beam energy of 15 MeV and has produced a resolution of about 10 keV for scattering from a 10 $\mu g/cm^2$ $^{197}Au$ target.[43] The $\alpha$ particle spectrum from a $^{244}Cm$ source was stepped along the counter by varying the magnetic field of the Enge magnet in order to measure the linearity of the detector.[43] Figure 8 shows a plot of the peak channel number versus the distance along the detector. The maximum integral nonlinearity observed was about 3% and was generally much less than this over most of the detector. Ford et al.[43] have observed no count rate limitations due to the proportional counter. Measurements with radioactive sources outside the magnet indicate that count rates up to several tens of thousands of counts per second may be used before the position resolution is worse than 0.5 mm.

## C. GAMMA-RAY DETECTORS

Three true coaxial Ge(Li) type ORTEC $\gamma$-ray detectors were used in this study. These detectors are of the type which have the detecting crystal cooled by a cold finger immersed in a liquid nitrogen dewar. Efficiencies of these detectors were rated as 10%, 13%, and 23% of the efficiency of a 3 inch by 3 inch NaI crystal, when both are located 25 cm from the target. A full width

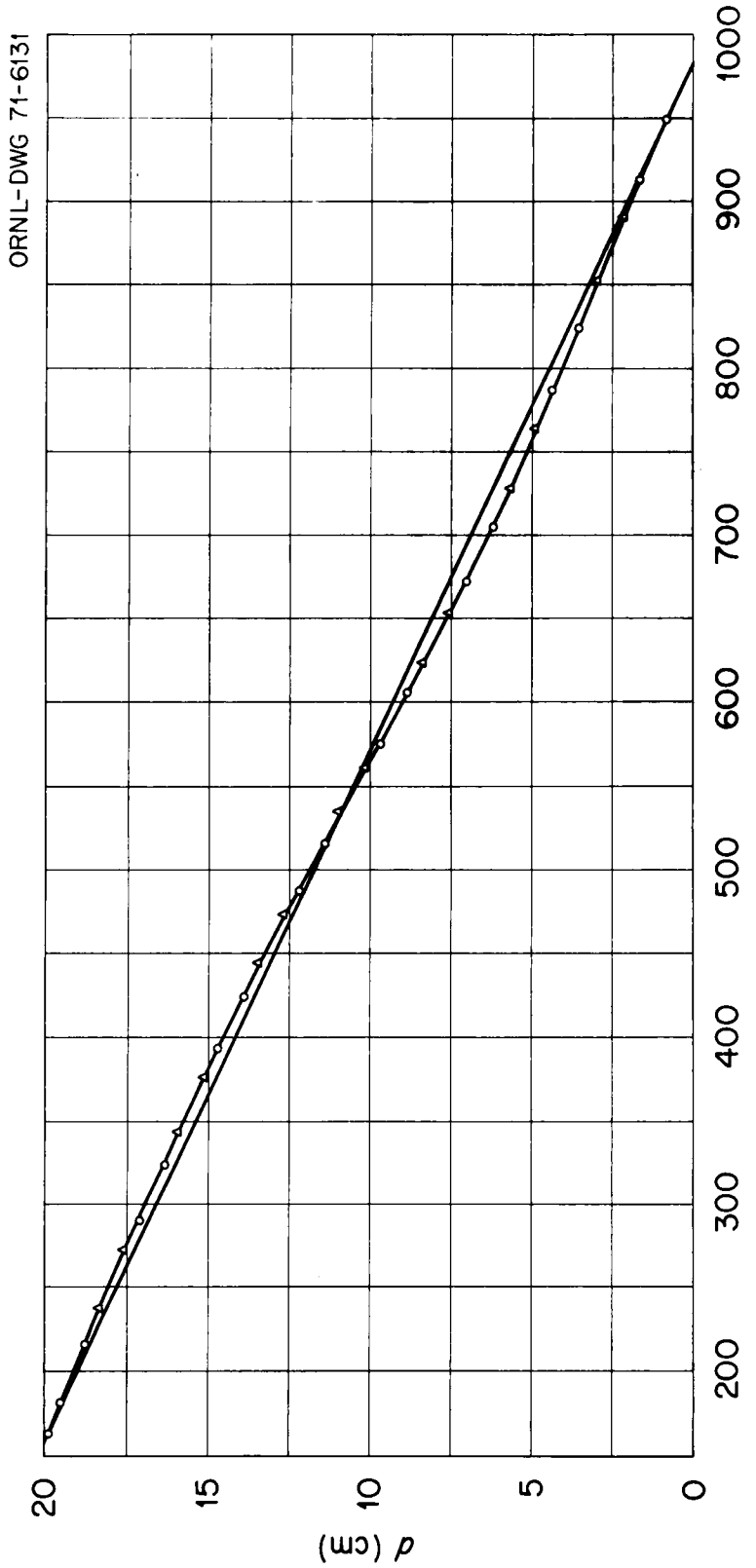


Figure 8. Linearity of the 20 cm gas flow proportional detector.

half maximum resolution of 2.20, 2.15, and 2.40 keV respectively for the 10%, 13%, and 23% Ge(Li) detectors was measured for the 1332 keV transition from $^{60}Co$. The large 100 $cm^3$ 23% detector had sustained some neutron damage which had degraded its resolution. Graded shields of 0.0089 cm Mo and 0.0127 cm Cu were placed in front of the detectors in order to suppress x-rays generated by the beam stopping in the target.

Efficiency Calibration

The details of the interaction of $\gamma$-rays with the Ge(Li) crystal have not been studied nearly as extensively as for the NaI crystal and hence cannot be used to calculate crystal efficiencies. In addition, the size and shape of the active volume may not be very well defined. As a result the efficiency of each detector was measured for each experimental setup by using a series of $\gamma$-ray sources of known strength.

Four separate sets of calibrated $\gamma$-ray sources were used for detector efficiency calibration in this study. One set of six $^{226}Ra$ sources of graded strength were used as the working set of sources. Each one of these sources had been calibrated against accurately known IAEA standard sources which had been calibrated in a "$4\pi$" $\gamma$ ionization chamber. This calibration is thought to be good to $\pm$ 4%. In addition each of these six sources has also been calibrated against an accurate National Bureau of Standards source and found to be within stated uncertainties.

As a check against these earlier efficiency calibrations, a second National Bureau of Standards (NBS) source was obtained which had recently been calibrated. This source was also used as a working standard in order to get calibration points in the 115 keV energy region where the $^{226}$Ra source had no points.

This second NBS source consisted of cobalt-57, cobalt-60, strontium-85, yttrium-88, cadmium-109, tin-113-indium-113m, cessium-137-barium-137m, cerium-139, and mercury-203, deposited as chlorides and sulfides, on polyester tape approximately 0.006 cm thick and covered by another layer of the same tape. The solutions used in the preparation of the mixture were measured in the National Bureau of Standards calibrated "4$\pi$" $\gamma$ ionization chamber, and the $\gamma$-ray emission rates calculated using published nuclear-decay parameters, where necessary. The total uncertainty in each of the $\gamma$-ray emission rates is the linear sum of 0.1%, which is the limit of the random error of the relative measurements using the ionization chamber, at the 99% confidence level (2.7 Sm, where Sm is the standard error computed from 4 sets of 20 measurements), and the estimated upper limits of conceivable systematic error in the preparation of this source and the calibration of the "4$\pi$" $\gamma$ ionization chamber. The total uncertainty for the second NBS source ranged from 1.2% to 3.0% for the different $\gamma$-rays.

Figure 9 shows a plot of the absolute efficiency of the 60 $cm^3$ coaxial Ge(Li) detector as a function of $\gamma$-ray energy. The source to detector distance was 6 cm and the efficiency was calculated using data measured from a $^{226}$Ra source of nominal strength of

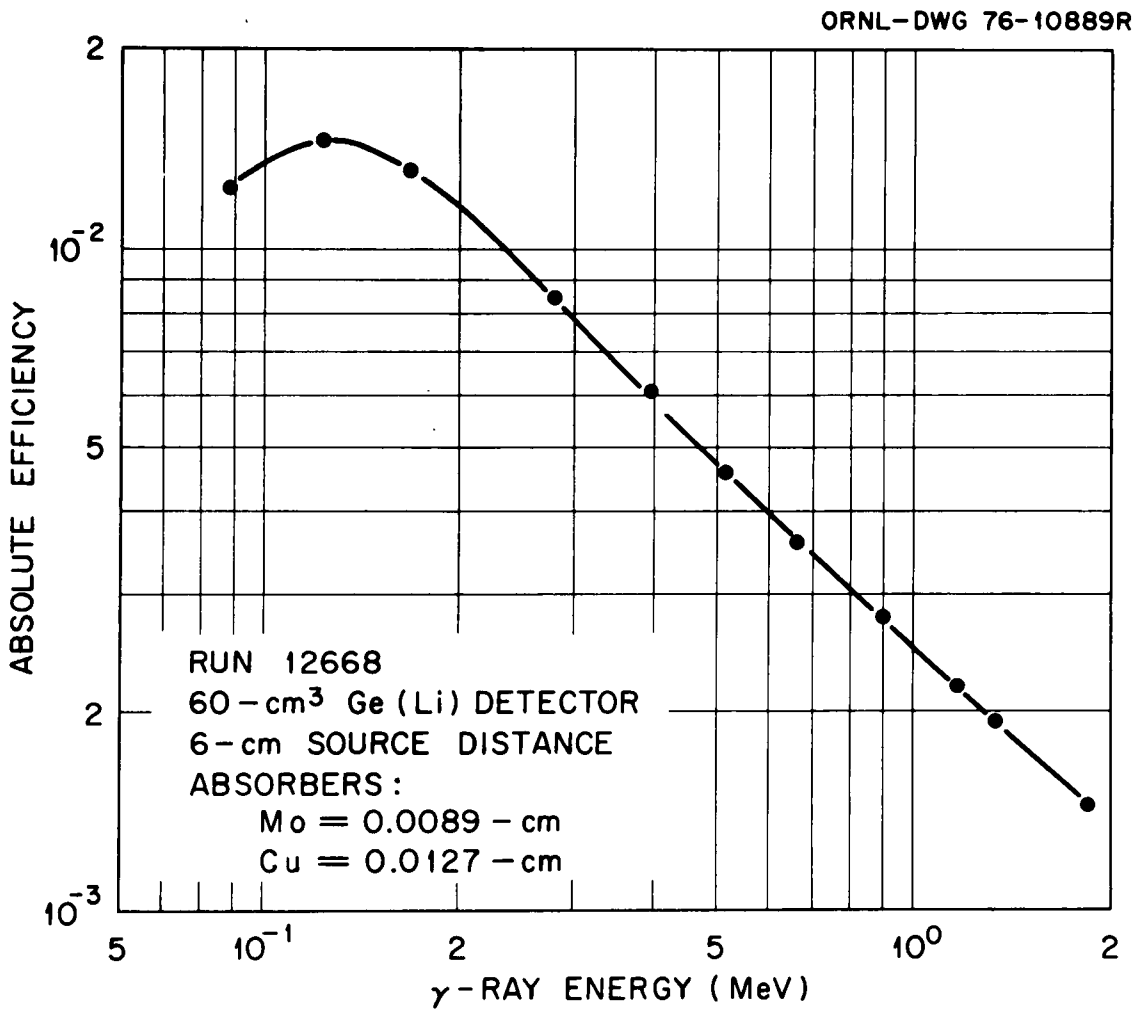


Figure 9. Absolute efficiency of the 60 $cm^3$ coaxial Ge(Li) detector as a function of γ-ray energy.

4,000 cps with this geometry. Figure 10 shows an efficiency curve measured for the 100 $cm^3$ coaxial Ge(Li) detector as a function of $\gamma$-ray energy. The bottom curve is fitted through data measured using the second NBS source with solid squares representing measured data points and open squares representing curve fitted points. As can be seen, the curve is quite smooth for a third order log-log curve fit. The NBS source was placed as close to the point of beam impact on the $^{115}Sn$ targets as possible. This curve was measured primarily to get the shape of the efficiency curve in the 115 keV region. This curve would then be normalized to the $^{226}Ra$ measured efficiency curve to get absolute efficiencies.

The top curve in Figure 10 represents data from the bottom curve measured with the NBS source and the efficiency as measured with the $^{226}Ra$ sources. The open circles are absolute efficiencies measured using the $^{226}Ra$ source and open circles with a flag are these data points which have less than a 1% statistical error. The solid circles are curve fitted points to the $^{226}Ra$ data and are used down to 279 keV. Both the $^{226}Ra$ fitted curve and the NBS fitted curve were brought into agreement by multiplying the NBS curve by 0.9959! An excellent agreement in absolute intensities. Solid triangles represent 0.9959 times the NBS experimental points between 88 and 1836 keV. Open triangles represent the fitted NBS curve times 0.9959 between 88 and 279 keV. Thus the NBS and $^{226}Ra$ source determined Ge(Li) efficiencies agree to within 0.41%. An uncertainty of $\lesssim \pm 3\%$ has been assigned to the Ge(Li) efficiency determination.

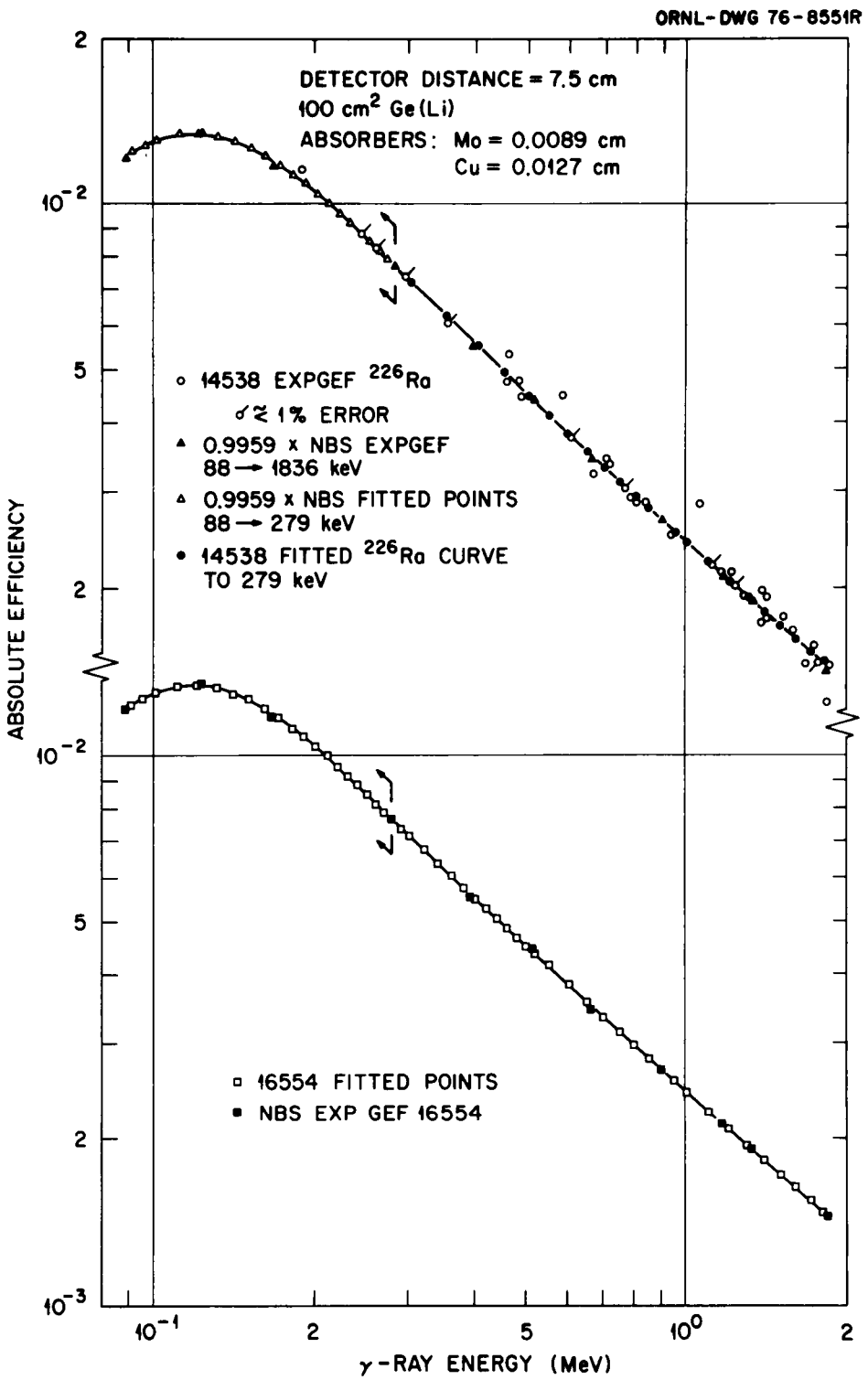


Figure 10. Absolute efficiency of the 100 $cm^3$ coaxial Ge(Li) detector as a function of γ-ray energy.

In practice a $^{226}Ra$ Ge(Li) efficiency was measured for each different experimental setup. The $^{226}Ra$ was placed at the position where the α beam struck the $^{115}Sn$ target and was mounted on the same weight nickel spinning so that backing absorption would be the same. The number of γ's per second measured in the full energy peak were then divided by the total given absolute disintegration rate in γ's per second to get the absolute efficiency for each γ-ray measured in the calibration source. A curve fitting routine provided a least squares fit to the data and outputed an interpolation table. Program SUPERTIZZ[45] was used to automatically strip out the number of counts in the full energy peaks. Output from SUPERTIZZ was then automatically made available for program RADICAL[45] which was used to calculate the $^{226}Ra$ efficiencies and provide interpolated output tables. All NBS calculations and stripping were done manually.

## D. GAMMA-RAY SINGLES EXPERIMENTS

Figure 11 shows the Ge(Li) detector positions for γ-ray yield and angular anisotropy measurements. Figure 11 is a plan view of the apparatus at the target location as shown in Figure 4 (page 33). Yield measurements were usually made with the detector at an angle of 55° where $P_2(\cos\theta)$ is very nearly zero and the yield measurement is thus approximately an angle independent one.

The beam tube is constructed of 0.0127 cm thick stainless steel. The targets are mounted on a 0.0127 cm thick nickel spinning which

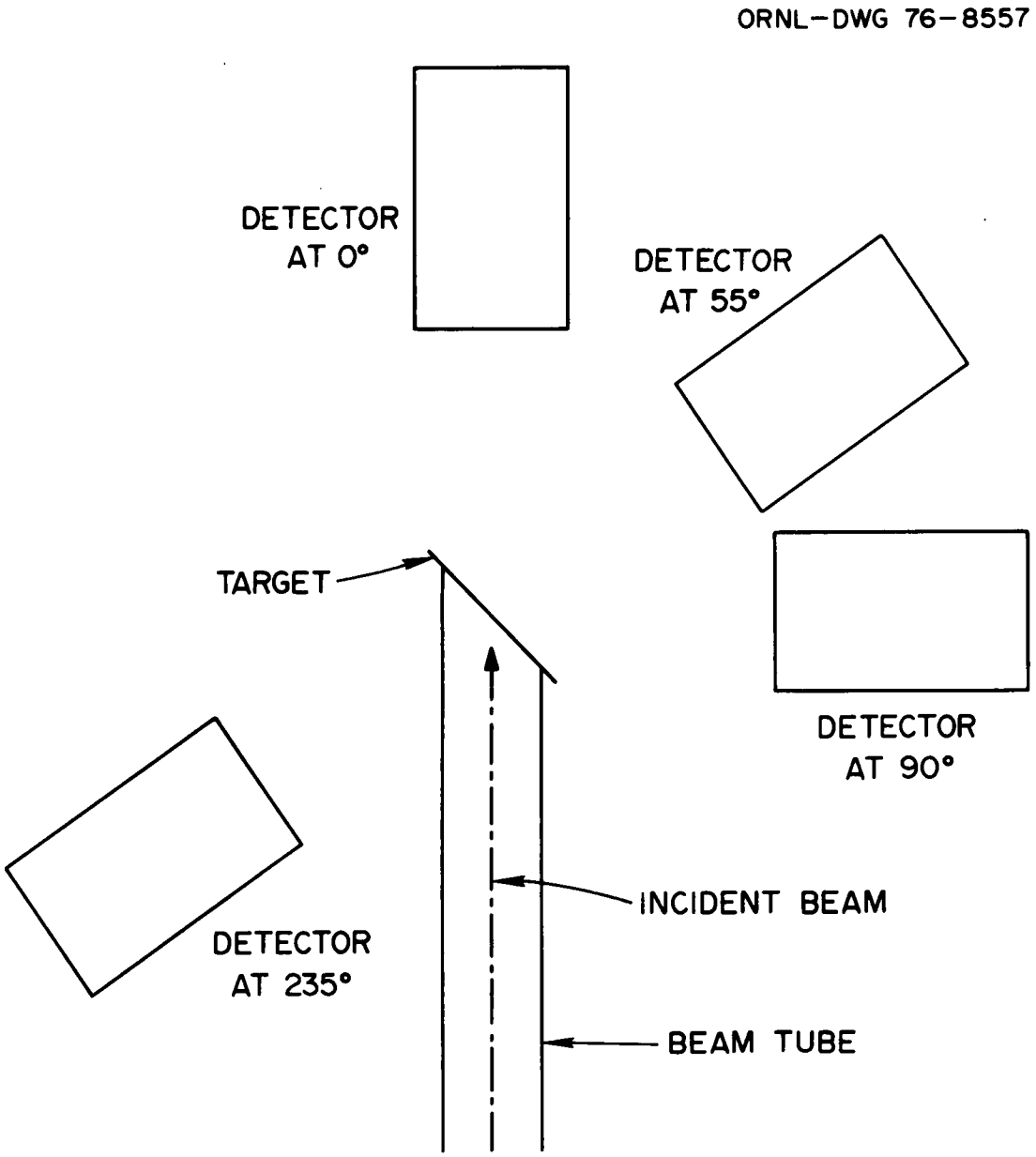


Figure 11. Ge(Li) detector positions for γ-ray yield and angular anisotropy measurements (top view).

has very nearly the same $\gamma$-ray attenuation coefficient as the steel beam tube.

Figure 12 is a diagram of the electronics setup used in $\gamma$-$\gamma$ coincidence measurements on $^{115}Sn$. For yield measurements this system is operated in the singles mode using the large 23% 100 $cm^3$ detector. The number of $^4He^{++}$ ions striking the target are measured by using an ORTEC current to pulse converter and then counting the total number of pulses during live beam time for each experiment. Initial setup included placing a radioactive source near the detector and adjusting gain settings to obtain the desired energy range. Adjustments were then made in the integral and differential time constants, pole-zero potentiometer, and base line restoration settings in order to obtain the best peak shape and minimum full width at half maximum for the anticipated count rate. Note the use of the TC212 dual summers on the cables between the main amplifier which was located in the experimental area and the Tennecomp PACE system which was located some 30 meters away. One cable is grounded to the amplifier chassis and is cabled to one dual summer input and contains only pickup noise. The second cable carries the signal plus pickup noise. The dual summer sums the two inputs and effectively cancels out the noise at the PACE system analog to digital converter input.

## E. GAMMA-RAY ANGULAR ANISOTROPY EXPERIMENTS

The $\gamma$-ray detector used in the angular anisotropy measurements was mounted on a movable boom at the target location as shown in

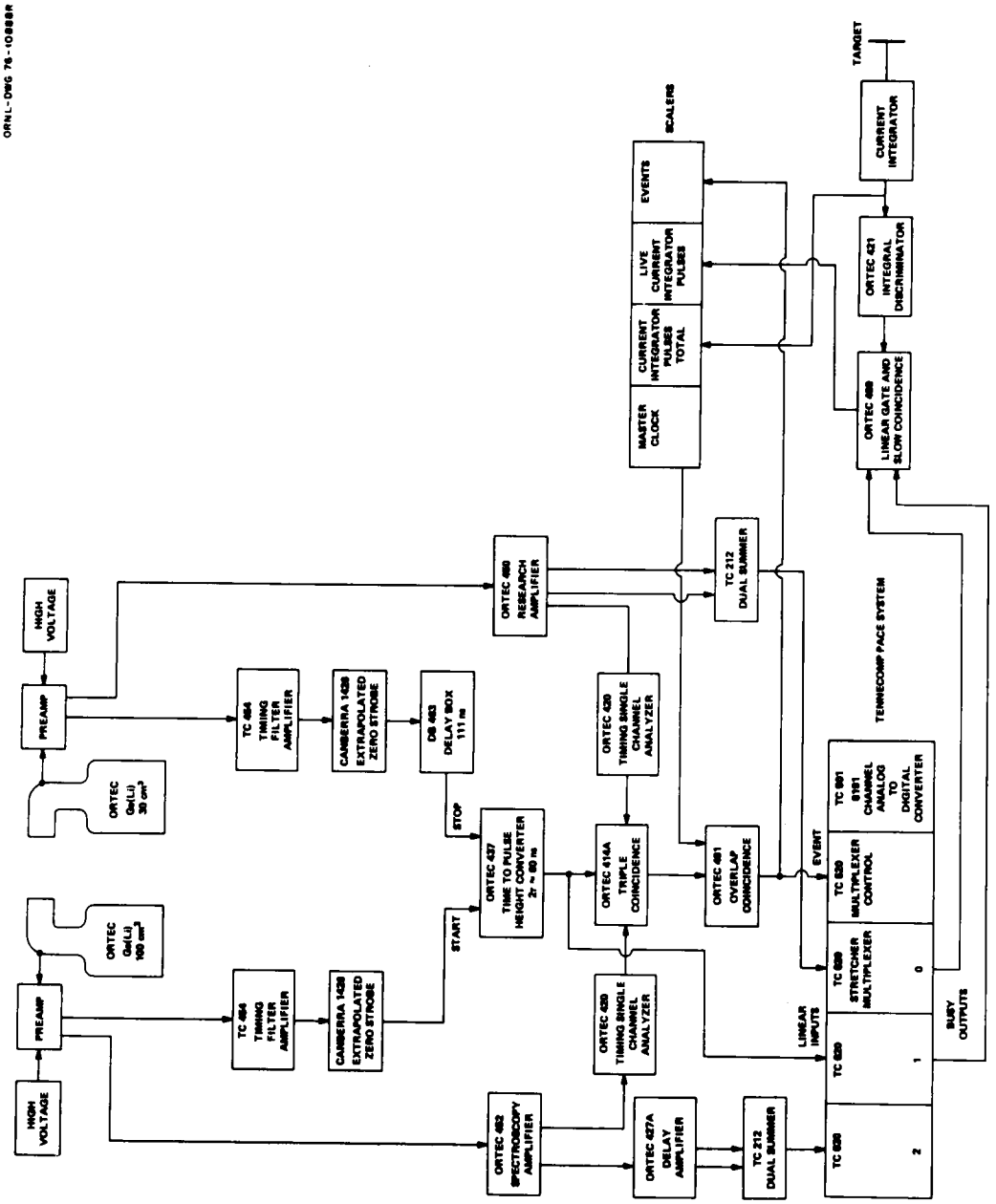


Figure 12. Diagram of the electronics setup used in $\gamma$-$\gamma$ coincidence measurements on $^{115}$Sn.

Figure 4 (page 33). This boom was rotated about the center of a heavy x-y adjustable machine table. An adjustment screw on the boom permitted the target to detector distance adjustments of 0 to 30 cm. Relative detector distances could be read to 0.1 mm with an estimated reproducibility of 0.1 mm. The angular position of the boom was continuously variable from 0 to ± 180°, but this angular travel was limited by interference between the detector and beam line tube as shown in Figure 11. The angle could be read to ± 0.1°. Two boom arms existed for mounting both detectors used in the $\gamma$-$\gamma$ coincidence runs.

Both detectors were securely shock mounted to the moveable boom tables. An alignment procedure was initiated before the experiment to insure that the beam axis was the same as the Ge(Li) detector axis when the detector was located at 0°, that the detector rotated in a plane perpendicular to the plane of the target, and that the center of rotation of each boom was the spot where the beam hit the target.

Figure 12 shows the detector electronics setup for use in the $\gamma$-$\gamma$ coincidence measurements which was used in the singles mode for the $\gamma$-ray angular anisotropy experiments.

## F. GAMMA-GAMMA COINCIDENCE EXPERIMENTS

The two Ge(Li) detectors used in the $\gamma$-$\gamma$ coincidence experiment were set up with one at 90° and one at 0°. They were run in as close to the target as possible to provide maximum coincidence

efficiency. Figure 12 shows a diagram of the electronics setup used in the $\gamma$-$\gamma$ coincidence measurements on $^{115}$Sn. Data was analyzed by program MEGASTRIP[45] on the PDP-11/45 using the Tennecomp PACE analog to digital converter system which processed data in a two-parameter mode.

The procedure for taking data with the PACE system is as follows. First each channel is set up to take 4096 channels of singles data with detectors "0" and "1." Data from the two singles channels are stored in the PDP-11/45 in a two-dimensional 4K x 4K event by event format. Sources are then positioned near the detector and the gain of each timing filter amplifier is adjusted for the energy range desired (typically 3 MeV $\rightarrow$ 10 Vdc conversion). An $^{241}$Am source is then placed in front of the detectors and the levels on the constant fraction discriminators are adjusted to allow the 60 keV $\gamma$-ray to pass. The objective is to set the level as low as possible, but above the noise. Then the two detectors are repositioned, one at 0° and the other at 90° and a $^{60}$Co source is placed in front of them. The output of the leading edge single channel is opened all the way, putting its output into the stretcher multiplexor. A singles spectrum is then taken for two different delay settings in order to obtain a time per channel calibration. The delay is then adjusted to $\sim$ 111 nsec and the leading edge single channel is adjusted to obtain the desired window width.

The two regular single channel analyzers feeding the triple coincidence box are then adjusted to pass the $\gamma$-rays of interest.

One must then check for overlap at the triple coincidence box. Next adjust the system so that the event pulse comes before the linear energy signal leaves the baseline and so that the gate pulse continues past the peak of the linear energy signal.

When the system is taking data, the PDP-11/45 will take 1024 4K x 4K events then dump them onto a special disk file on the CDC-3200 computer. When this file contains $\sim$ 500,000 events or by manual initiation a program PUSSE[45] is initiated which then updates the spectra by processing the raw event-by-event data. This raw data is sorted into a 1K x 1K two-dimensional spectrum and a series of up to 50 gated 4K spectra. At the conclusion of each run one should dump and save the summed "x" and "y" gates to assist in setting $\gamma$-ray and background gates in the 1K x 1K spectra. Also, one should make efficiency measurements before repositioning the detectors. Program GATOR[45] is used to process gated spectra from the 1K x 1K data. A $^{4}$He beam at 10.6 MeV was used to Coulomb excite the $^{115}$Sn in these coincidence runs.

## G. DOPPLER SHIFT LIFETIME MEASUREMENTS

Doppler shift lifetime measurements were performed at 0° and 90° positions as shown in Figure 11 (page 52). In some cases the Doppler shifted part of the peak for the 0° case was obscured by contaminant $\gamma$-rays. For these cases the 90° Doppler shifted peak was used to determine the lifetime.

Program DOPCO[48] in conjunction with program TUTTLAID[48] both on the CDC-3200 were used in analyzing the Doppler shifted peaks for the lifetime of the excited states.

Program DOPCO

In many nuclear reactions the residual nucleus recoils with a velocity which is sufficient to produce a significant Doppler shift in the energy of the emitted γ-ray, as observed with a Ge(Li) detector. The γ-ray energy $E_L$ measured by a detector is related to the unshifted energy $E_{cm}$ by

$$E_L = E_{cm} \frac{[1 - (v/c)^2]^{1/2}}{1 + (v/c)\cos \theta_L}, \qquad \text{(IV-1)}$$

where c is the velocity of light, v is the velocity of the γ-ray source, and $\theta_L$ denotes the angle of γ-ray emission relative to the direction of motion of the source in the laboratory.

For the case where the velocity of the recoiling nucleus is uniform, all γ-rays which are emitted at a given angle will be shifted in energy by the same amount. If, on the other hand, the recoiling nucleus is slowed down, as it is in a thick target, the observed γ-ray energy will depend on the time of emission. Thus, in principle, if the rate of energy loss of the recoil nucleus is known then its decay rate or lifetime can be deduced from an analysis of the distribution of γ-ray energies emitted at some particular angle $\theta_L$. The experimental situation considered involves the use of a thick target and a γ-ray detector which subtends a large solid angle.

A computer program, DOPCO, has been written which calculates the complete Doppler shifted line shape that is observed from the

in-flight decay of a nucleus excited by a direct E2 or E3 Coulomb excitation event. The program, DOPCO, is designed to take the following effects into account:

1. The energy loss of the projectile in the thick target.
2. The differential cross-section of the reaction.
3. The distribution of recoil velocities.
4. The energy loss of the recoiling nucleus in the thick target.
5. The lifetime of the nuclear state.
6. The effect of cascade feeding for up to 9 higher lying states (not used in the present calculations).
7. The angular correlation of the emitted $\gamma$-rays.
8. The variation of the detector efficiency with the angle of incidence of the $\gamma$-rays.
9. The energy resolution of the detector.

DOPCO was operated in the singles mode with no restriction on the scattering angle of the projectile. The $\gamma$-ray was defined to be incident on the flat face of a true coaxial Ge(Li) crystal.

A comparison of the experimental and calculated shapes (by DOPCO) is carried out using program TUTTLAID[48] as follows. The experimental spectrum is read from magnetic tape or the CDC-3200 master data file by TUTTLAID during execution. Input data cards specify the number of channels on each side of the Doppler shifted peak being fitted and how much background to subtract from the experimental peak. A peak position (for the unshifted spectrum) and a detector

resolution are chosen from the input list. The detector resolution is folded into the calculated spectrum and the resulting spectrum is shifted to the assumed peak position and normalized to the same area (between the upper and lower channels specified) as the experimental spectrum. The quality of the fit, QFN, is calculated for the fit of the calculated to the experimental shape. This comparison is repeated for all lifetimes in the list with the peak position and detector resolution held fixed. The best lifetime and its uncertainty is then estimated from the QFN vs. lifetime curve. A printer plot of the experimental spectrum and the three best calculated spectra are outputed in the form of a three cycle semilog plot. Each run with DOPCO typically takes approximately 25 minutes while a run with TUTTLAID takes a few minutes on the CDC-3200.

## H. TARGET PREPARATION TECHNIQUES

### Thick Targets

In beam $\gamma$-ray spectroscopy measurements have been performed using two isotopically enriched thick $^{115}$Sn targets.

Isotopic enrichments for these two targets were performed in the Isotopes Division, Oak Ridge National Laboratory calutron isotope separators during this study. In this process feed material for the first pass isotope separation consisted of natural abundance SnS material. This material was heated in the isotope separator ion source oven to $\sim$ 500°C to form SnS vapor. This vapor then passed

into the ion source arc chamber where Sn+ ions were formed by electron bombardment in the ∿ 3 ampere, 100 volt arc discharge. The charged particles were then accelerated from the ion source using a +35 kV accelerating voltage. The charged ion beam, which consisted of many different complex positive ion species, was then passed into an analyzing magnetic field of the 180° type. The Sn+ part of the ion spectrum was magnetically focused onto the ion receiver after 180° of travel in the ∿ 61 cm radius focusing field. Each isotope was caught in a separate purified graphite pocket. To recover the isotopically enriched isotopes the pockets were first burned to remove the carbon and then the residue was chemically purified.[49] Table I gives the natural abundance of the tin feed material and the isotopic composition of the enriched product of a first pass.

Isotopically enriched $^{115}Sn$ was obtained from this first pass separation in order to test out a previously developed target plating method[50] with this relatively inexpensive material. High isotopic purity second pass $^{115}Sn$ was expected to be very scarce and hence would require a high efficiency target plating method for its use.

Product from the first pass isotope separation formed the charge material for a second pass isotope separation. The prime difference in a second pass separation is that a premium is placed on chemically recovering unprocessed (∿ 90%) valuable charge material. Table I gives the isotopic composition of the product from the second pass isotope separation.

TABLE I

Mass analysis of thick $^{115}Sn$ targets
(Ni substrate = 0.013 cm, electrodeposited)

| Mass | Natural Abundance | Target 1 | Target 2 |
|---|---|---|---|
| 112 | 0.96 | 0.40 | 0.11 |
| 114 | 0.66 | 1.23 | 0.16 |
| 115 | 0.35 | 28.52 | 92.31 |
| 116 | 14.30 | 35.05 | 3.89 |
| 117 | 7.61 | 7.41 | 0.41 |
| 118 | 24.03 | 14.09 | 1.66 |
| 119 | 8.58 | 2.83 | 0.27 |
| 120 | 32.85 | 8.34 | 0.77 |
| 122 | 4.92 | 1.04 | 0.20 |
| 124 | 5.94 | 1.10 | 0.23 |
| Thickness | --- | 43 $mg/cm^2$ | 24 $mg/cm^2$ |

Thick electroplated targets were prepared using both the 28.52% and 92.31% $^{115}Sn$ material. The Appendix gives the details of preparing the target plating solution and the target plating apparatus. Table II gives a brief set of specifications on the thick Sn targets. The $^{115}Sn$ was electroplated onto 0.013 cm thick nickel spinnings. Table II lists the chemical contaminants which have been identified based mostly on measured $\gamma$-ray spectrum. Unfortunately the emphasis on the second target had to be on high electroplating efficiency and this resulted in a higher contaminant level of low Z impurities as observed by the $\gamma$-ray spectrum.

Figure 13 is a volume ion microprobe scan of the 28.52% $^{115}Sn$ target showing the impurities which are present in this target. Enough material was available for chemical purification of the 28.52% $^{115}Sn$ so that this probably represents the lowest contaminant level available with the present chemical purification method. A higher level of contaminants was measured in the $\gamma$-ray spectrum for the rare 92.31% target. In the ion microprobe measurement a beam of ions (any of the gases) is directed onto the target where they sputter material from the surface. A certain fraction of the sputtered atoms are charged depending on their chemical species. These secondary ions are then mass analyzed by a second analyzer to identify the species which are being sputtered from the surface. Thus this process has the highest sensitivity for those atoms which are most easily ionized.

TABLE II

Specifications for the thin and thick targets

---

Thin target of $^{115}Sn$

Target substrate - 90 $\mu g/cm^2$ carbon

Target size - 1.5 mm x 1.27 cm

Target thickness - 75 $\mu g/cm^2$

Substrate chemical contaminants[a]: Si, Ca, K, P, Cl, O, Al, S

Target chemical contaminants[a]: Cr, Fe, Cu, Mn?

Thick targets of $^{115}Sn$

Target substrate - .013 cm nickel

Target size - 1.270 cm diameter

Target thickness of electrodeposition: 28.52% $^{115}Sn$ - 43 $mg/cm^2$

92.31% $^{115}Sn$ - 24 $mg/cm^2$

Target chemical contaminants[b]: S, Al, Ni, F, Cu, O, Na, Cr, Zn, Ca, N, Fe, Mg, Si, K

---

[a] Based on ion $\mu$ probe spectrum and $(\alpha,\alpha')$ spectrum at 10.2 MeV. Assignment of contaminant to substrate or target is based on knowledge of preparation process.

[b] Based on $\gamma$-ray spectrum.

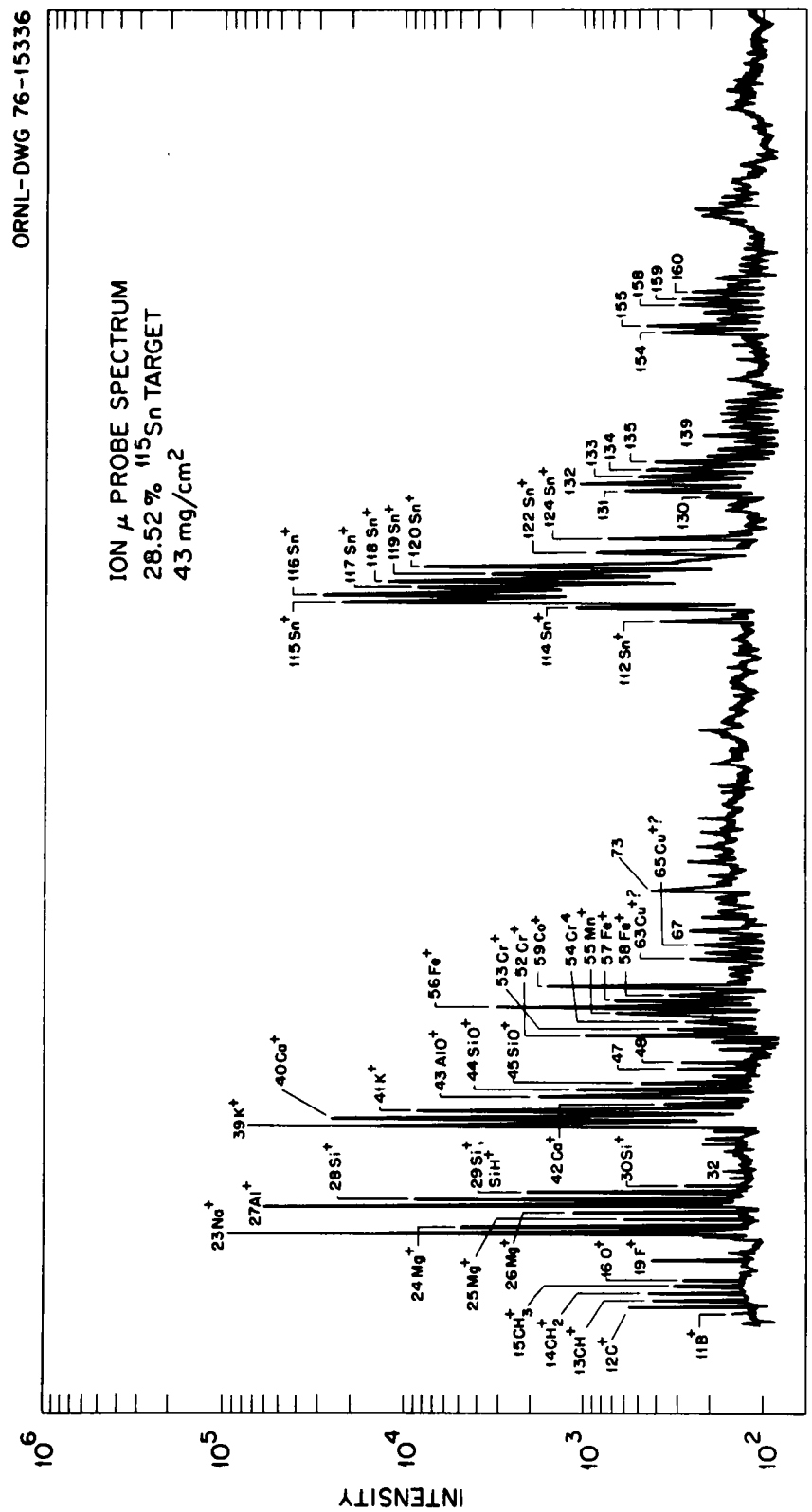


Figure 13. Volume ion microprobe scan of the 28.52% $^{115}Sn$ target showing impurities.

Thin Targets

High purity thin targets of $^{115}Sn$ were required for use with the Enge spectrograph apparatus described in Chapter IV Section B. These targets were required to have higher than 99% isotopic abundance and a chemical purity such that elastic scattering peaks from the contaminants did not interfere with the $^{115}Sn$ weak inelastic peaks. These targets were prepared by the method of direct beam deposition using the 180° Oak Ridge Sector Isotope Separator[52] (ORSIS) to thicknesses of $\sim$ 25 $\mu g/cm^2$ and $\sim$ 75 $\mu g/cm^2$.

The 180° ORSIS is shown schematically in Figure 14 and pictorially in Figure 15. This is an isotope separator of the sector focusing type with the source and receiver outside the main magnetic field at a focal distance of 254 cm. Ions are formed in a modified calutron ion source of the Nier type, are accelerated to 40 keV and travel 254 cm to the magnetic sector field. Here the ions are deflected through 180° and focused by the n = 0.8 (field inhomogeniety), r = 71 cm, inhomogenous magnetic sector field. They leave the sector field and travel 254 cm in straight line trajectories to the deceleration collector.

A high vacuum of $\sim 1 \times 10^{-6}$ Torr is maintained in the separator magnet and receiver region in order to minimize gas scattering and charge exchange isotopic contamination. The receiver region is pumped by $LN_2$ cooled cryopanels and a $LN_2$ trapped oil diffusion pump. The beam line oil diffusion pumps are also trapped with $LN_2$. Santovac-5, a completely hydrocarbon based

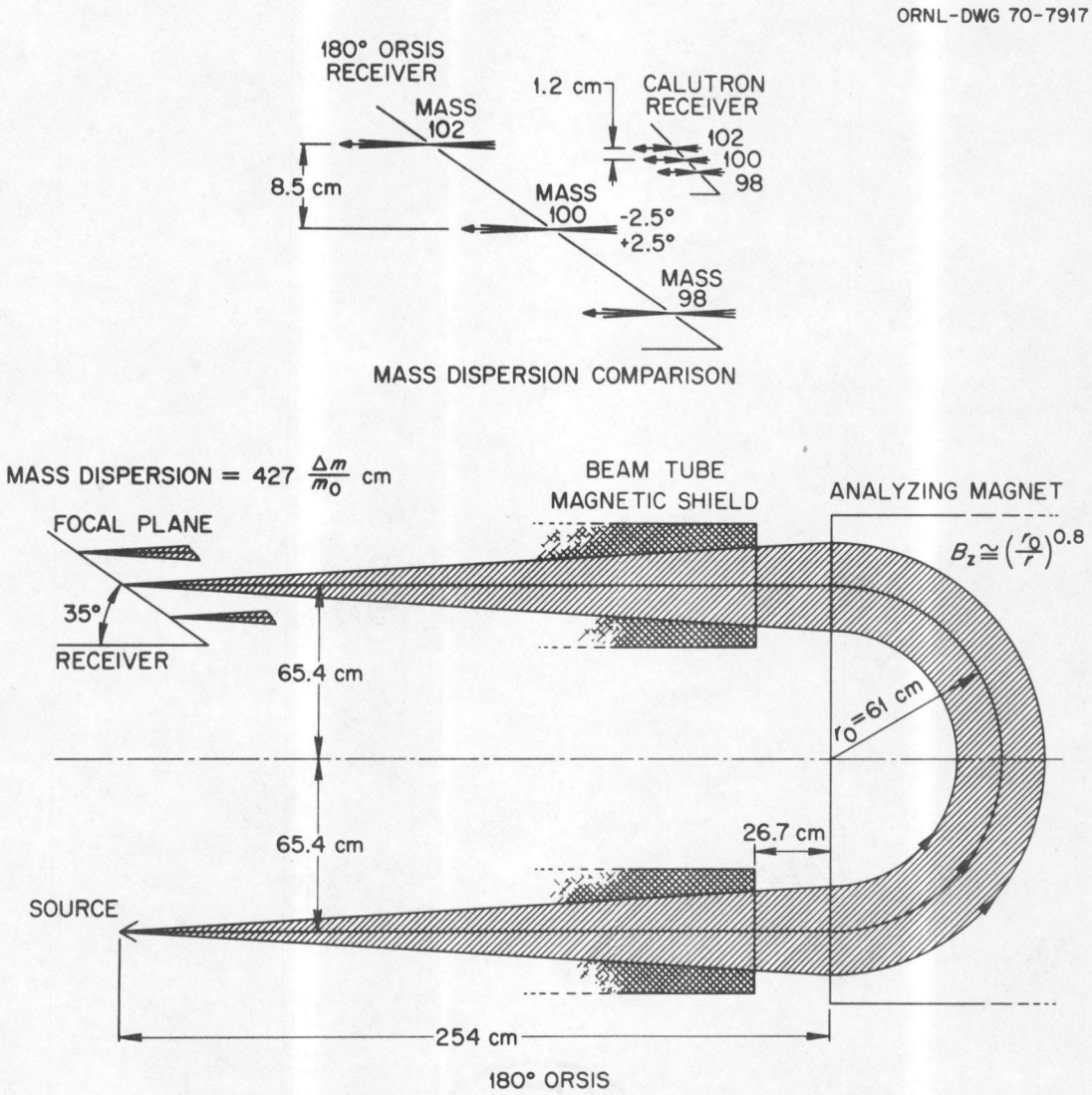


Figure 14. Schematic of the 180° Oak Ridge Sector Isotope Separator ion optic system.

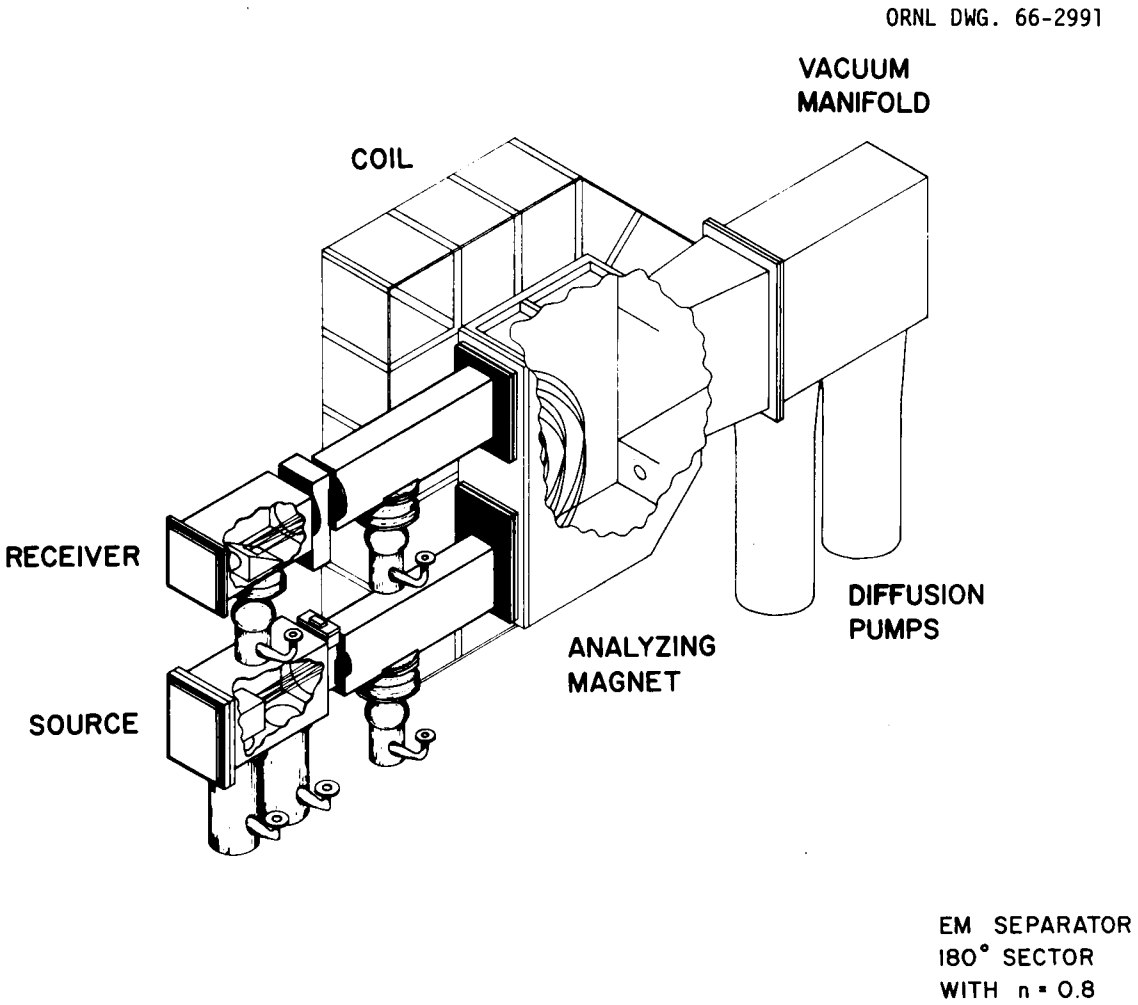


Figure 15. Schematic of the 180° Oak Ridge Sector Isotope Separator used to prepare the high purity thin tin targets.

low vapor pressure oil, is used in all diffusion pumps. The large oil diffusion pumps of the magnet vacuum manifold are trapped by freon cooled baffles and the source pumps use water cooled baffles.

Figure 16 shows a picture of the latest deflection target receiver used in the 180° ORSIS to prepare the last uncontaminated thin targets. Figure 17 shows a schematic of the earlier version of the target apparatus (shown in Figure 16) used to collect the targets which were actually used during this research. During the collection of $^{115}$Sn the $^{116}$Sn mass beam was centered on the beam positioner probes. A differential current signal was taken from the beam positioner probes and amplified to provide a feedback signal to the ion beam accelerating voltage. This feedback loop effectively stabilized the ion beam position against magnet drift or accelerating voltage drift and kept the $^{115}$Sn beam centered in the collection slot.

The $^{115}$Sn beam passed through the grounded electrode where it was defined and then deflected slightly up or down as needed by the second set of electrodes to center the beam on the target. The $\sim$ 39.8 kV retarding field between the second set of electrodes and the target box slowed the beam down to $\sim$ 200 eV energy and focused the $\sim$ 13 cm long beam down to a $\sim$ 1.5 x 44 mm line. The target substrate was shielded from stray ions so that it accurately (within $\pm$ 10%) monitored target beam current. The low 200 eV energy was necessary for Sn whose self sputtering ratio is one at $\sim$ 400 eV. This means that only $\sim$ 50% of the Sn ions striking the surface at 200 eV are actually collected on the target.

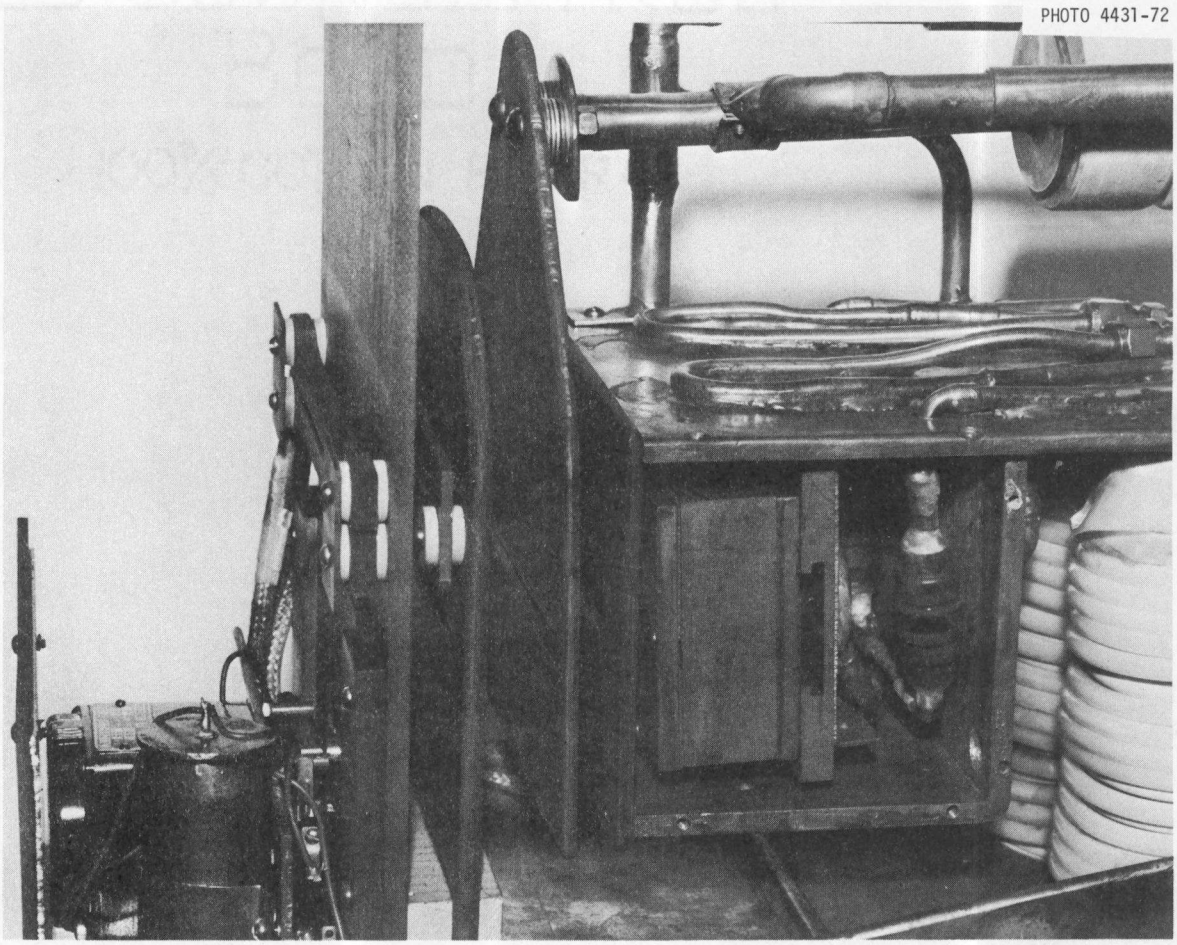


Figure 16. Photograph of the 180° Oak Ridge Sector Isotope Separator target apparatus.

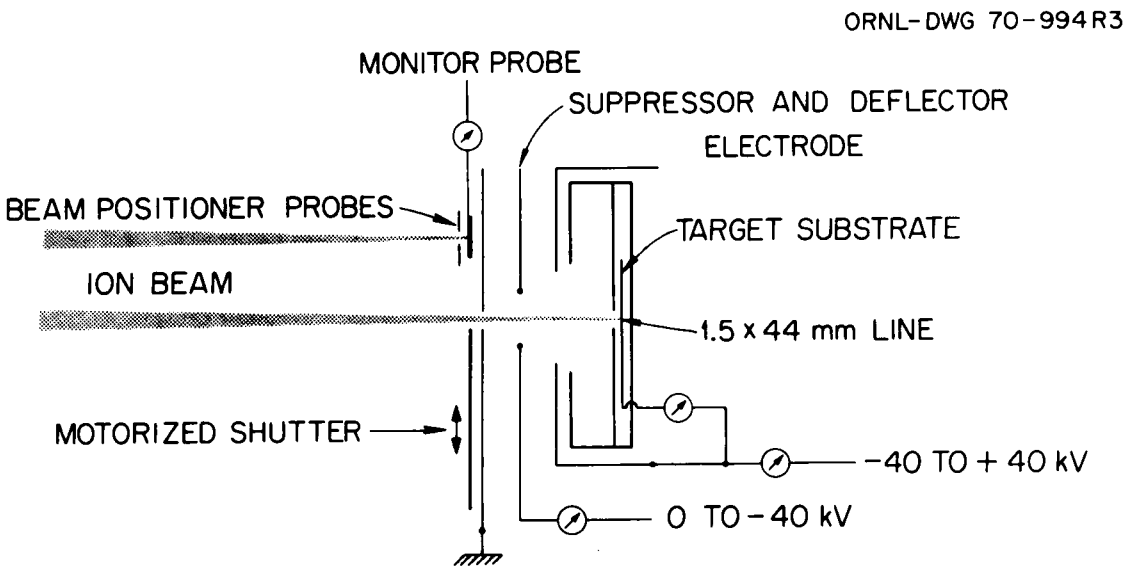


Figure 17. Schematic of the target apparatus used on the 180° Oak Ridge Sector Isotope Separator to prepare the high purity thin tin targets.

A significant benefit of collecting isotopes at this low energy is that the isotopic contamination is greatly reduced. This benefit occurs because low energy ions formed by residual gas scattering, ion source sparking, charge exchange, etc., are effectively filtered out at the receiver. The receiver acts as a high pass energy filter which excludes all ions which have energies more than 200 eV less than the main beam. For example, lowering the $^{116}Sn$ beam into the $^{115}Sn$ mass position at constant magnetic field would require a change of accelerating voltage from +40.000 kV down to +39.652 kV. These ions would be repelled because they need 39.800 keV to enter the receiver. In this manner an isotopic enrichment was obtained for the thin Sn targets which exceeded values obtained in two passes through the calutron. The total isotopic enrichment, $\mu$, for $^{115}Sn$ was $\sim$ 32,000 as opposed to $\sim$ 114 for the calutron single pass. The isotopic enrichment is defined as

$$\mu = \frac{100 - A_c}{A_c} \times \frac{A_p}{100 - A_p}, \qquad \text{(IV-2)}$$

where $A_c$ = mass assay of the charge material and $A_p$ = mass assay of the separated isotope.

Table II (page 64) gives the specifications for the thin $^{115}Sn$ targets and lists the target chemical contaminants. The chemical contaminants were determined from an ion microprobe spectrum and from the $(\alpha,\alpha')$ spectrum obtained on the Tandem Van de Graaff.

Most of the chemical contaminants in the target material itself are thought to have been sputtered onto it from surfaces near the front of the receiver. Future targets can reduce this effect by deflecting the ion beam away from these neutral particles before decelerating it. This has been successfully done, but unfortunately time did not permit running the target to see if the contamination had really been reduced.

Figure 18 shows an ion microprobe scan of the $^{115}Sn$ target surface and that the $^{116}Sn$ abundance is very low. Table III is a mass assay calculated from the scan of Figure 18. The best probable assay shown in the last column of Table III is calculated using contamination profiles from other isotopic separations in which complete mass assays were available. Hydride formation subtraction in the ion microprobe analysis is not expected to raise the 99.12% $^{115}Sn$ assay to more than 99.35%. This last column also gives the distribution of mass contaminants expected.

Figure 19 shows a wide spectrum ion microprobe scan of the 99.12% direct beam deposited thin $^{115}Sn$ target. This spectrum is to be compared with that of Figure 13 (page 65) which shows the same scan for the 28.52% $^{115}Sn$ electrodeposited target. Note the great reduction in target contaminants. The Na+ peak is almost a factor of 100 less when compared to the $^{115}Sn$ peak. It appears that thick isotopic targets of any element could be built up in this manner by direct beam deposition and at much higher isotope and chemical purities than by other methods.

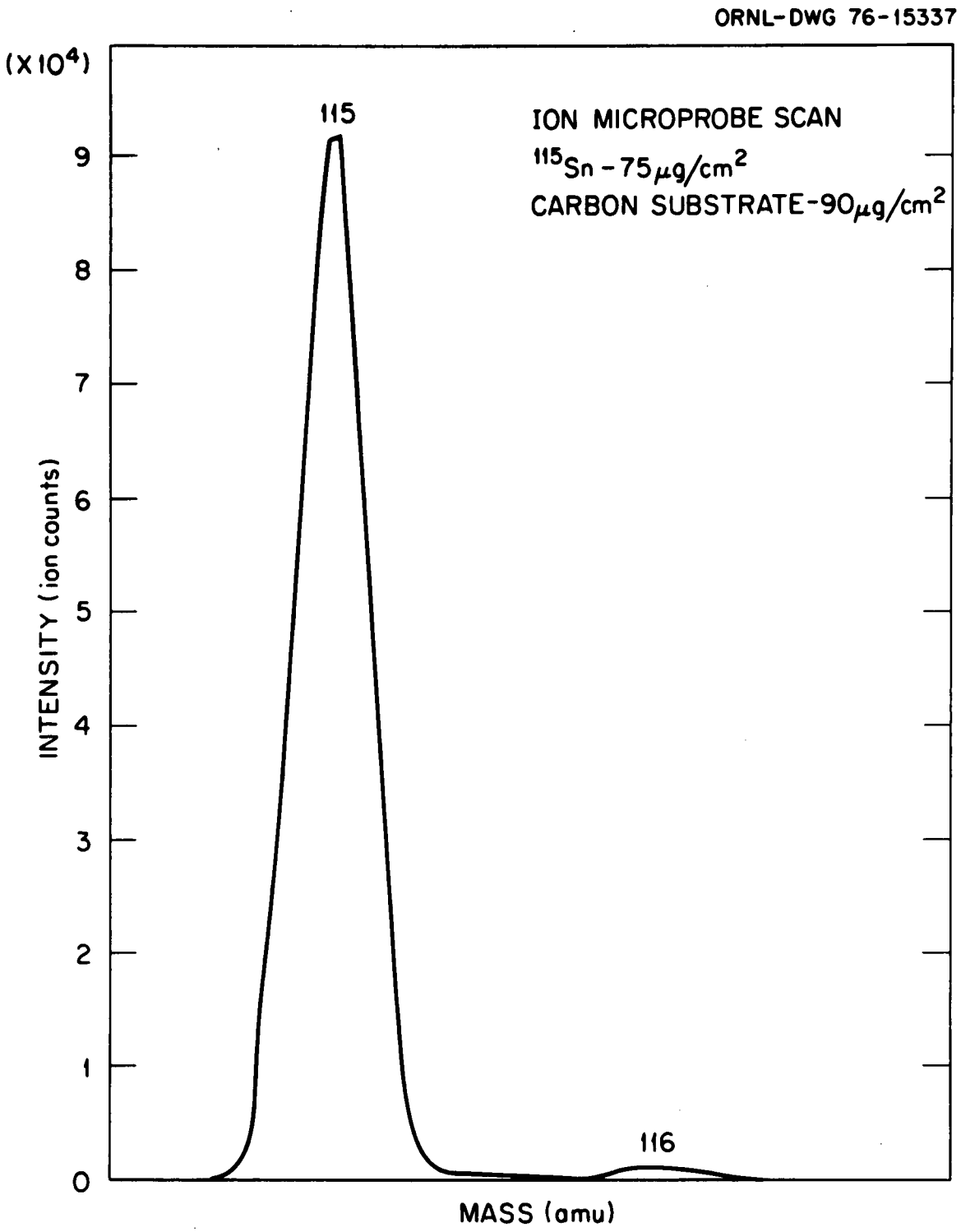


Figure 18. Ion microprobe scan of the 99.12% $^{115}Sn$ thin target (thickness 75 $\mu g/cm^2$).

TABLE III

Mass assay for the $^{115}Sn$ thin target from the ion microprobe spectrum

| Mass | Natural Abundance (%) | Target Assay | |
|---|---|---|---|
| | | Ion μ Probe (%) | Best Probable Assay, Calculated from Ion μ Probe Data[a] (%) |
| 112 | 0.96 | --- | 0.002 |
| 114 | 0.66 | --- | 0.023 |
| 115 | 0.35 | > 99.12 | 99.345 |
| 116 | 14.30 | < 0.88[b] | 0.509 |
| 117 | 7.61 | --- | 0.049 |
| 118 | 24.03 | --- | 0.050 |
| 119 | 8.58 | --- | 0.007 |
| 120 | 32.85 | --- | 0.014 |
| 122 | 4.92 | --- | 0.001 |
| 124 | 5.94 | --- | 0.000 |

[a] Based on contamination profiles from other isotopic separations.

[b] Amount of $^{115}Sn^{1}H$ which appears in mass 116 position is unknown.

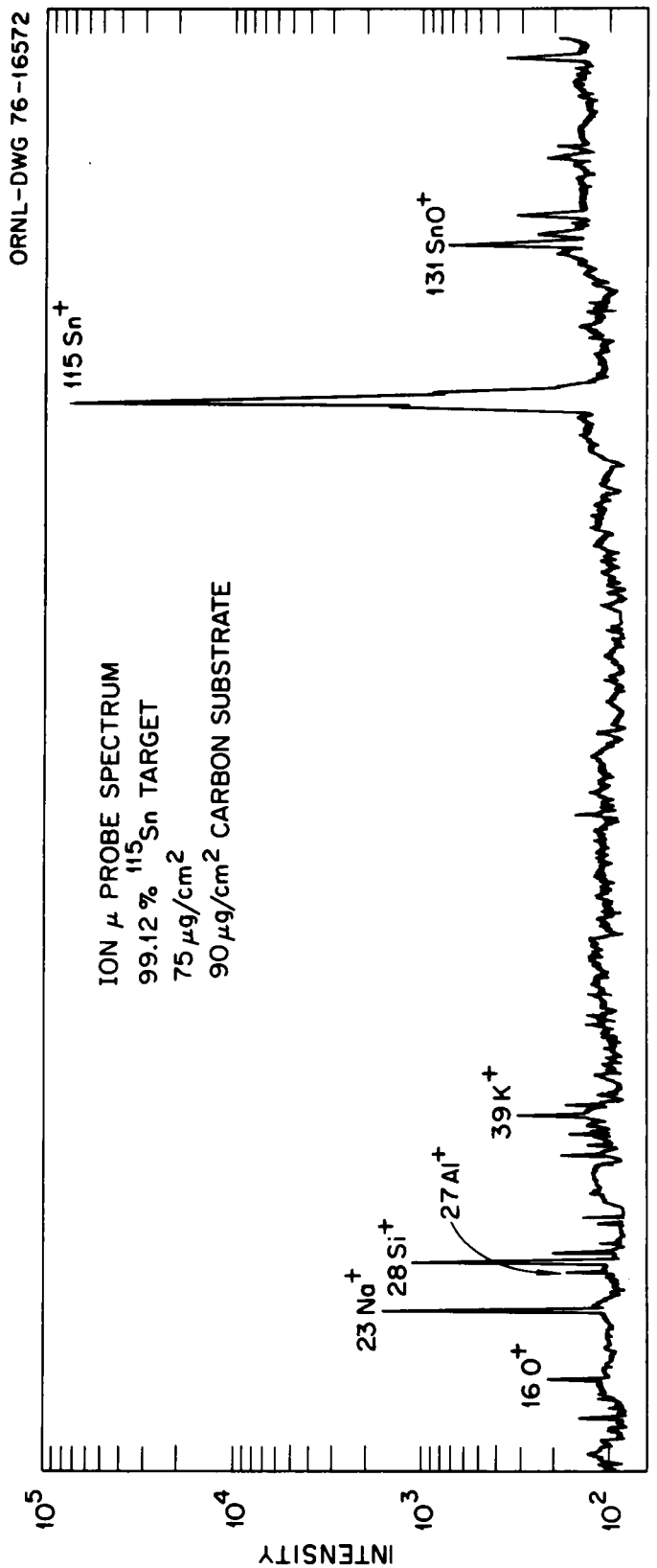


Figure 19. Ion microprobe scan of the 99.12% $^{115}Sn$ thin target showing impurities.

# I. REDUCTION OF GAMMA-RAY SPECTRA AND $(\alpha,\alpha')$ SPECTRA

The reduction, or stripping, of a pulse height spectrum refers to the extraction of full-energy peak areas for the $\gamma$-rays or inelastic peaks of interest. For $\gamma$-rays division of the peak areas by the detector efficiency gives the $\gamma$-ray intensities. The discussion of this section will be done in three parts, reduction of the singles spectrum, reduction of the coincidence spectrum, and reduction of the $(\alpha,\alpha')$ Enge spectrum. Both the peak areas of the calibration source $\gamma$-rays from the efficiency calibration and the peak areas of the de-excitation $\gamma$-rays were important for the determination of $\gamma$-ray intensities from Ge(Li) spectra taken during a Coulomb excitation experiment. Because of this all peak areas were extracted in a consistent manner in order to minimize reading errors.

## Singles Spectra

Gamma-ray spectra were reduced by several different methods, whenever possible. These methods were by in-house computer programs TIZZY,[45] NASTY,[45] and SUPERTIZZ,[45] by light pen programs used in conjunction with the PDP-11/45 data system,[45] and by hand stripping methods. Programs TIZZY, NASTY, and SUPERTIZZ are CDC-3200 peak stripping programs with varying degrees of automatic operation. Program SUPERTIZZ, which was used mostly, provides peak location, summed areas, Gaussian fitted areas, and associated stastistical errors to these quantities. The light pen programs provide

atuomatic printout of hand-guided light pen stripped areas. Some peaks were manually stripped from computer printout of the peak channel count distributions. By manual stripping it is meant that a number of channels above and below the peak are summed and normalized for a background calculation which is then substracted from the total counts in the peak.

The gross counts, $N_G$, for the peak are defined as

$$N_G = N_1 \pm \sqrt{N_1} \ , \qquad \text{(IV-3)}$$

where $N_1$ is the total number of counts in the peak. The background counts, $N_B$, are defined as

$$N_B = f \times (N_2 \pm \sqrt{N_2}), \qquad \text{(IV-4)}$$

where

$$f = \frac{\text{number of channels in the peak}}{\text{number of channels in the background}} \ , \qquad \text{(IV-5)}$$

and where $N_2$ is the total number of counts in the background. The net counts, $N_N$, are expressed as

$$N_N = (N_1 - fN_2) \pm \sqrt{N_1 + f^2 N_2} = N \pm \varepsilon_N \ . \qquad \text{(IV-6)}$$

The expression for the error, $\epsilon_N$, comes from statistical considerations, and corresponds to one standard deviation.

With the light pen, each peak was stripped several times, and a best estimate obtained with an associated error which was due to inconsistency in resolution of a doublet or triplet or due to inconsistency in background determination. The final full energy peak area was an average of the values obtained by the three peak area determining methods.

Coincidence Spectra

All coincidence data was taken in the 1K x 1K, event by event format. Gates are set on this data by examining the 1K one-dimensional X and Y summed spectra. The summed spectra was also examined to determine suitable background gates above and below the peak gate of interest. Program GATOR[45] was then used to generate the gated spectra, which were obtained by subtracting the weighted background gate from the $\gamma$ gate. Coincidence intensities were then determined for each $\gamma$ gate by stripping out these singles spectra.

$^{115}Sn(\alpha,\alpha')^{115}Sn$ Spectra

Peaks in these spectra were stripped by all three methods, but only the hand method was used for the final calculations. In some cases where the background was parabolic shaped, a curve fitting routine was used to get background counts versus channel. This curve was then used for background subtraction.

# CHAPTER V

## EXPERIMENTAL RESULTS

In this chapter results from the Coulomb excitation $\gamma$-ray and $^{115}Sn(\alpha,\alpha')^{115}Sn$ experiments will be presented. Comments and discussion will be made on the analysis of the data and deduction of the final form of the data when appropriate. Discussion of the individual levels will be deferred until Chapter VI.

### A. GAMMA-RAY SINGLES

Figure 20 shows the $\gamma$-ray spectrum observed with a 60 $cm^3$ Ge(Li) detector when 10.5 MeV $\alpha$-particles Coulomb excited an isotopically enriched $^{115}Sn$ target whose enrichment was 28.52% $^{115}Sn$. Figure 21 shows the $\gamma$-ray spectrum observed with a 100 $cm^3$ Ge(Li) detector when 10.6 MeV $\alpha$-particles Coulomb excited an isotopically enriched $^{115}Sn$ target whose enrichment was 92.31% $^{115}Sn$. Arrows with small solid circles at the top identify $^{115}Sn$ $\gamma$-rays. The energy uncertainty of the $^{115}Sn$ $\gamma$-rays and levels are given later in the energy level diagram. Table IV and Table V present a detailed list of the $\gamma$-rays which are plotted in Figures 20 and 21 for the 28.52% and 92.31% $^{115}Sn$ targets respectively. The $\gamma$-ray raw intensities are derived from the automatic spectrum stripping routine SUPERTIZZ.[45] These raw intensities are divided by the detector efficiency to get the true intensity and then normalized to 100 for the 497.34 keV $\gamma$-ray.

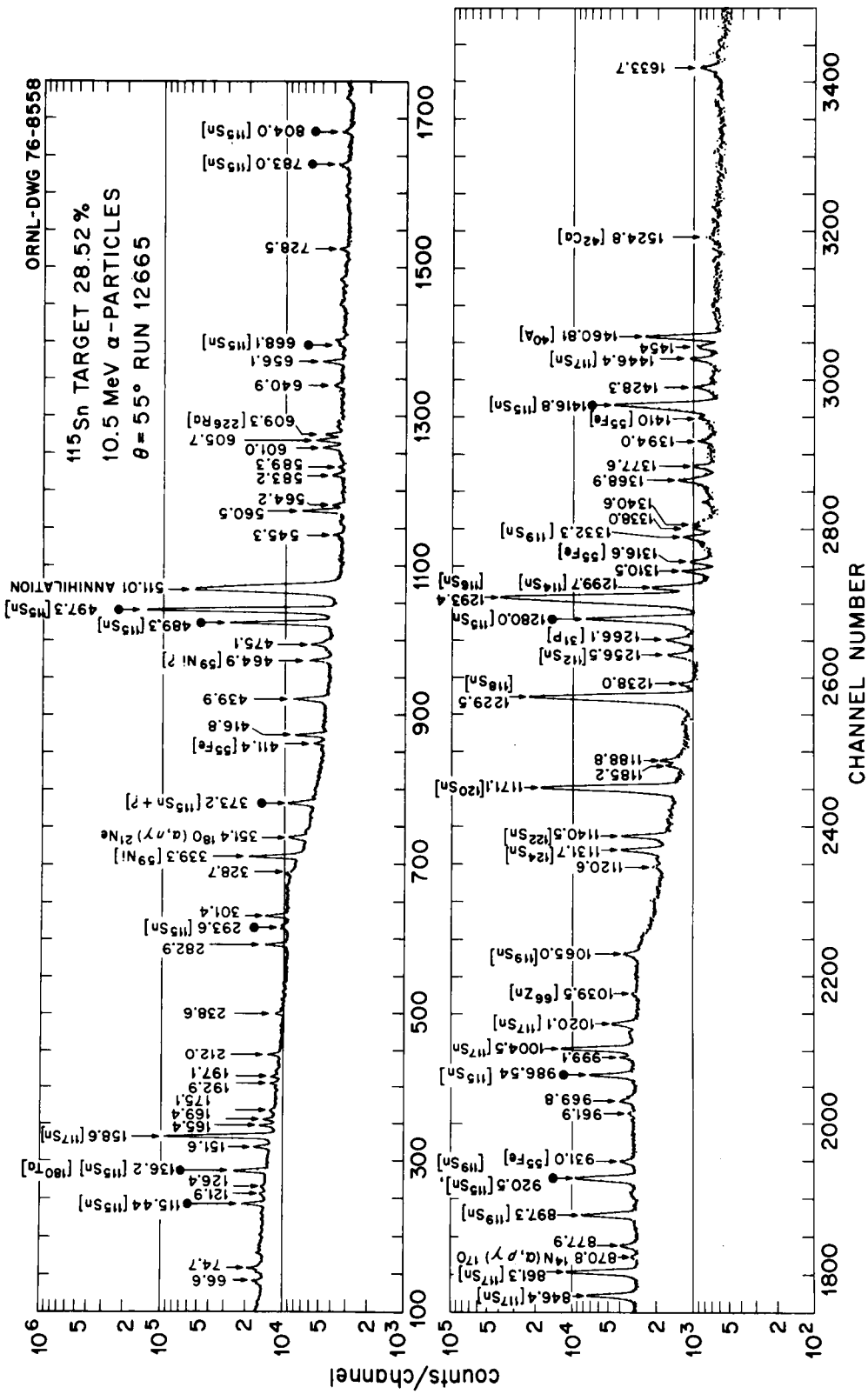


Figure 20. Gamma-ray spectrum observed with a 60 $cm^3$ Ge(Li) detector when 10.5 MeV α-particles Coulomb excited an isotopically enriched $^{115}Sn$ target whose enrichment was 28.52% $^{115}Sn$.

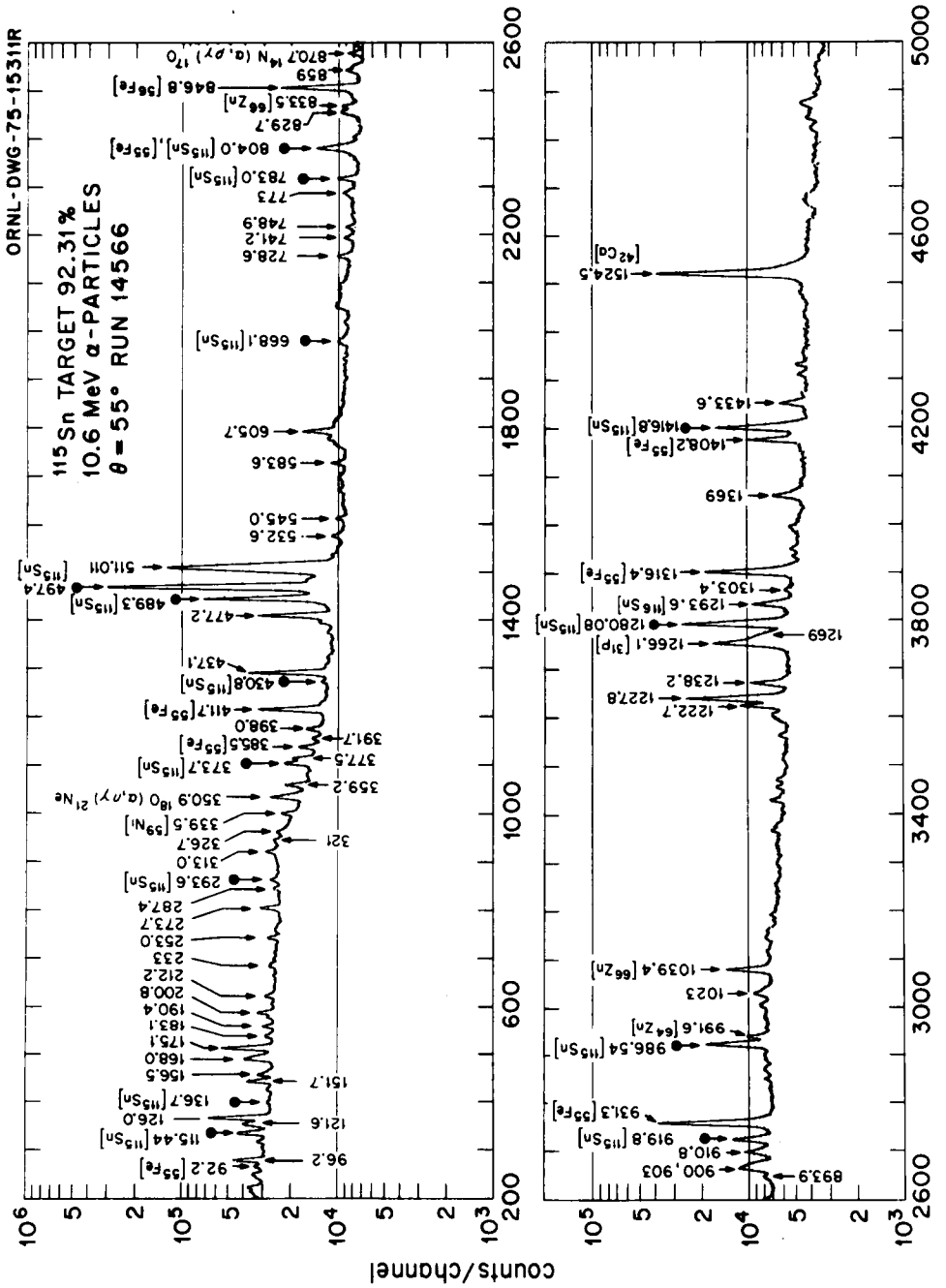


Figure 21. Gamma-ray spectrum observed with a 100 $cm^3$ Ge(Li) detector when 10.6 MeV α-particles Coulomb excited an isotopically enriched $^{115}Sn$ target whose enrichment was 92.31% $^{115}Sn$.

TABLE IV

List of γ-rays from the $^{115}Sn(\alpha,\alpha'\gamma)^{115}Sn$ reaction with identification of contaminant and $^{115}Sn$ lines for the 28.52% $^{115}Sn$ target

| Number | Energy (keV) | Intensity | Identification |
|---|---|---|---|
| 1 | 28.17 | 3619.63 ± 0.0 | |
| 2 | 66.62 | 11.35 ± 0.57 | |
| 3 | 74.68 | 10.20 ± 0.29 | |
| 4 | 76.78 | 2.01 ± 0.25 | |
| 5 | 84.77 | 1.38 ± 0.17 | |
| 6 | 87.79 | 0.99 ± 0.11 | |
| 7 | 90.37 | 0.89 ± 0.12 | |
| 8 | 96.32 | 0.23 ± 0.13 | |
| 9 | 115.44 | 2.90 ± 0.08 | $^{115}Sn$ |
| 10 | 121.86 | 0.45 ± 0.06 | |
| 11 | 126.47 | 0.33 ± 0.06 | |
| 12 | 136.24 | 3.45 ± 0.06 | $^{181}Ta, ^{115}Sn$ |
| 13 | 151.56 | 1.40 ± 0.05 | |
| 14 | 158.63 | 21.37 ± 0.04 | $^{117}Sn$ |
| 15 | 165.37 | 0.74 ± 0.04 | |
| 16 | 169.37 | 0.67 ± 0.04 | |
| 17 | 175.13 | 0.34 ± 0.05 | |
| 18 | 192.54 | 0.47 ± 0.04 | |
| 19 | 197.52 | 0.47 ± 0.04 | $^{19}F$ |
| 20 | 211.97 | 0.78 ± 0.05 | |
| 21 | 238.59 | 0.51 ± 0.05 | |
| 22 | 241.91 | 0.22 ± 0.05 | |
| 23 | 257.86 | 0.14 ± 0.06 | |
| 24 | 282.90 | 2.01 ± 0.07 | $^{61}Ni$ |
| 25 | 294.17 | 0.87 ± 0.07 | $^{115}Sn$+? |
| 26 | 301.39 | 2.09 ± 0.07 | |
| 27 | 328.75 | 0.39 ± 0.07 | |
| 28 | 339.26 | 6.29 ± 0.08 | |
| 29 | 351.39 | 2.04 ± 0.07 | |
| 30 | 373.16 | 2.74 ± 0.07 | $^{115}Sn, ^{43}Ca$? |
| 31 | 411.39 | 0.58 ± 0.06 | $^{52}Cr(\alpha,n)^{55}Fe$ |
| 32 | 416.77 | 2.15 ± 0.06 | $^{23}Na(\alpha,n)^{26}Al$ |
| 33 | 439.86 | 3.34 ± 0.07 | $^{23}Na$ |
| 34 | 464.94 | 1.43 ± 0.07 | |
| 35 | 475.09 | 2.26 ± 0.07 | |
| 36 | 489.22 | 20.45 ± 0.08 | $^{115}Sn$ |

TABLE IV (continued)

| Number | Energy (keV) | Intensity | Identification |
|---|---|---|---|
| 37 | 497.34 | 100.00 ± 0.10 | $^{115}Sn$ |
| 38 | 511.01 | 78.71 ± 0.08 | Annihilation |
| 39 | 544.98 | 0.45 ± 0.08 | |
| 40 | 560.53 | 3.74 ± 0.07 | |
| 41 | 564.22 | 0.51 ± 0.06 | $^{53}Cr$ |
| 42 | 583.26 | 0.78 ± 0.08 | $^{19}F(\alpha,n)^{22}Na$ |
| 43 | 600.96 | 1.35 ± 0.08 | |
| 44 | 605.73 | 1.92 ± 0.07 | |
| 45 | 609.37 | 0.85 ± 0.08 | $^{226}Ra$ |
| 46 | 640.89 | 0.62 ± 0.09 | |
| 47 | 656.08 | 1.67 ± 0.09 | $^{61}Ni$ |
| 48 | 669.26 | 0.81 ± 0.09 | $^{115}Sn, ^{63}Cu$ |
| 49 | 693.44 | 0.47 ± 0.09 | |
| 50 | 728.55 | 0.62 ± 0.09 | |
| 51 | 782.65 | 1.08 ± 0.10 | $^{115}Sn$ |
| 52 | 804.07 | 0.84 ± 0.10 | $^{115}Sn, ^{52}Cr(\alpha,n)^{55}Fe, ?$ |
| 53 | 825.97 | 0.58 ± 0.10 | |
| 54 | 846.44 | 8.27 ± 0.12 | $^{117}Sn$ |
| 55 | 861.33 | 15.10 ± 0.12 | $^{117}Sn$ |
| 56 | 870.77 | 0.31 ± 0.10 | $^{14}N(\alpha,p)^{17}O$ |
| 57 | 877.91 | 2.03 ± 0.11 | $^{56}Fe(\alpha,n)^{59}Ni$ |
| 58 | 897.27 | 9.95 ± 0.12 | $^{119}Sn$ |
| 59 | 920.49 | 13.54 ± 0.12 | $^{115}Sn, ^{119}Sn$ |
| 60 | 931.04 | 1.79 ± 0.12 | $^{52}Cr(\alpha,n)^{55}Fe$ |
| 61 | 961.92 | 0.43 ± 0.12 | |
| 62 | 969.84 | 1.82 ± 0.10 | |
| 63 | 972.84 | 0.53 ± 0.10 | |
| 64 | 986.54 | 7.95 ± 0.13 | $^{115}Sn$ |
| 65 | 999.16 | 1.71 ± 0.12 | |
| 66 | 1004.46 | 18.12 ± 0.14 | $^{117}Sn$ |
| 67 | 1020.10 | 3.96 ± 0.13 | $^{117}Sn$ |
| 68 | 1039.28 | 0.52 ± 0.13 | $^{63}Cu(\alpha,p)^{66}Zn$ |
| 69 | 1065.04 | 2.52 ± 0.13 | $^{119}Sn$ |
| 70 | 1099.58 | 0.24 ± 0.11 | |
| 71 | 1120.80 | 0.38 ± 0.11 | |
| 72 | 1131.66 | 5.29 ± 0.12 | $^{124}Sn$ |
| 73 | 1140.47 | 4.93 ± 0.11 | $^{122}Sn$ |
| 74 | 1171.13 | 44.92 ± 0.13 | $^{120}Sn$ |
| 75 | 1185.17 | 0.45 ± 0.07 | |
| 76 | 1186.70 | 0.25 ± 0.03 | |
| 77 | 1188.87 | 1.57 ± 0.08 | $^{56}Fe(\alpha,n)^{59}Ni$ |

TABLE IV (continued)

| Number | Energy (keV) | Intensity | Identification |
|---|---|---|---|
| 78 | 1229.50 | 63.53 ± 0.19 | $^{118}$Sn |
| 79 | 1238.09 | 0.59 ± 0.09 | |
| 80 | 1256.53 | 2.03 ± 0.09 | $^{112}$Sn |
| 81 | 1266.11 | 1.68 ± 0.09 | $^{28}$Si(α,p)$^{31}$P |
| 82 | 1279.90 | 18.93 ± 0.13 | $^{115}$Sn |
| 83 | 1293.35 | 124.69 ± 0.25 | $^{116}$Sn |
| 84 | 1299.78 | 3.39 ± 0.09 | $^{114}$Sn |
| 85 | 1310.36 | 1.42 ± 0.08 | |
| 86 | 1316.59 | 0.99 ± 0.08 | |
| 87 | 1331.95 | 1.37 ± 0.08 | $^{119}$Sn,$^{60}$Ni |
| 88 | 1337.99 | 0.62 ± 0.06 | |
| 89 | 1341.09 | 0.81 ± 0.06 | |
| 90 | 1366.99 | 0.66 ± 0.07 | |
| 91 | 1368.91 | 1.39 ± 0.07 | $^{24}$Mg |
| 92 | 1377.67 | 0.62 ± 0.08 | |
| 93 | 1394.02 | 0.56 ± 0.08 | |
| 94 | 1409.92 | 0.93 ± 0.08 | |
| 95 | 1416.78 | 13.06 ± 0.12 | $^{115}$Sn |
| 96 | 1428.29 | 0.80 ± 0.08 | |
| 97 | 1446.40 | 1.08 ± 0.09 | $^{117}$Sn |
| 98 | 1454.32 | 1.00 ± 0.08 | $^{58}$Ni |
| 99 | 1460.82 | 5.60 ± 0.09 | $^{40}$K decay |
| 100 | 1524.81 | 0.43 ± 0.09 | $^{42}$Ca |
| 101 | 1633.66 | 0.94 ± 0.09 | $^{17}$O(α,n)$^{20}$Ne |
| 102 | 1678.06 | 0.62 ± 0.09 | |
| 103 | 1732.17 | 0.80 ± 0.09 | |
| 104 | 1764.56 | 0.62 ± 0.09 | |
| 105 | 1778.65 | 2.51 ± 0.09 | $^{28}$Si |
| 106 | 1781.66 | 0.73 ± 0.08 | |
| 107 | 1806.15 | 1.72 ± 0.10 | |
| 108 | 1808.60 | 2.78 ± 0.09 | $^{23}$Na |

TABLE V

List of γ-rays from the $^{115}Sn(\alpha,\alpha'\gamma)^{115}Sn$ reaction with identification of contaminant and $^{115}Sn$ lines for the 92.31% $^{115}Sn$ target

| Number | Energy (keV) | Intensity | Identification |
|---|---|---|---|
| 1 | 52.11 | 5.87 ± 0.94 | |
| 2 | 54.70 | 3.73 ± 0.69 | |
| 3 | 67.55 | 5.34 ± 0.26 | $^{61}Ni$ |
| 4 | 74.98 | 2.75 ± 0.14 | |
| 5 | 77.96 | 1.39 ± 0.12 | |
| 6 | 84.01 | 0.27 ± 0.08 | |
| 7 | 86.74 | 1.13 ± 0.07 | |
| 8 | 91.93 | 0.79 ± 0.07 | |
| 9 | 96.33 | 1.73 ± 0.06 | |
| 10 | 109.46 | 0.30 ± 0.04 | |
| 11 | 115.44 | 1.99 ± 0.04 | $^{115}Sn$ |
| 12 | 121.87 | 1.78 ± 0.03 | |
| 13 | 125.93 | 5.51 ± 0.03 | |
| 14 | 137.03 | 0.19 ± 0.03 | $^{115}Sn$ |
| 15 | 146.08 | 0.10 ± 0.03 | |
| 16 | 151.53 | 1.72 ± 0.03 | |
| 17 | 156.21 | 0.80 ± 0.02 | |
| 18 | 158.58 | 0.21 ± 0.02 | $^{117}Sn$ |
| 19 | 167.09 | 1.11 ± 0.02 | |
| 20 | 170.33 | 0.21 ± 0.02 | |
| 21 | 174.94 | 2.11 ± 0.02 | |
| 22 | 183.10 | 0.25 ± 0.02 | |
| 23 | 190.14 | 0.27 ± 0.02 | |
| 24 | 197.45 | 0.28 ± 0.02 | $^{19}F$ |
| 25 | 200.64 | 0.49 ± 0.02 | |
| 26 | 211.95 | 0.64 ± 0.03 | |
| 27 | 234.39 | 0.53 ± 0.03 | |
| 28 | 238.26 | 0.20 ± 0.03 | $^{16}O(\alpha,n)^{19}Ne$ |
| 29 | 252.92 | 0.25 ± 0.03 | |
| 30 | 273.49 | 1.17 ± 0.03 | |
| 31 | 287.31 | 0.19 ± 0.04 | |
| 32 | 293.59 | 0.48 ± 0.04 | $^{115}Sn$ |
| 33 | 312.84 | 1.44 ± 0.04 | |
| 34 | 320.89 | 0.14 ± 0.04 | |
| 35 | 326.51 | 0.45 ± 0.04 | |
| 36 | 339.33 | 0.76 ± 0.04 | |
| 37 | 350.70 | 2.92 ± 0.04 | $^{18}O(\alpha,n)^{21}Ne$ |

TABLE V (continued)

| Number | Energy (keV) | Intensity | Identification |
|---|---|---|---|
| 38 | 359.00 | 0.99 ± 0.04 | |
| 39 | 374.07 | 1.88 ± 0.03 | $^{115}Sn$ |
| 40 | 377.52 | 1.40 ± 0.03 | |
| 41 | 385.51 | 1.12 ± 0.04 | |
| 42 | 391.53 | 0.23 ± 0.04 | |
| 43 | 397.80 | 0.62 ± 0.04 | |
| 44 | 411.60 | 7.76 ± 0.04 | $^{52}Cr(\alpha,n)^{55}Fe$ |
| 45 | 415.12 | 0.63 ± 0.03 | |
| 46 | 437.02 | 8.32 ± 0.04 | |
| 47 | 472.56 | 0.65 ± 0.04 | |
| 48 | 477.25 | 6.18 ± 0.04 | |
| 49 | 489.30 | 17.74 ± 0.05 | $^{115}Sn$ |
| 50 | 497.38 | 100.00 ± 0.10 | $^{115}Sn$ |
| 51 | 500.81 | 1.43 ± 0.04 | |
| 52 | 511.00 | 17.39 ± 0.05 | Annihilation |
| 53 | 533.00 | 0.63 ± 0.04 | |
| 54 | 564.99 | 0.20 ± 0.04 | |
| 55 | 583.72 | 0.39 ± 0.04 | |
| 56 | 605.67 | 0.68 0.05 | |
| 57 | 667.86 | 0.48 0.04 | $^{115}Sn$ |
| 58 | 670.60 | 0.42 ± 0.04 | $^{63}Cu$ |
| 59 | 692.87 | 0.60 ± 0.04 | |
| 60 | 695.51 | 0.37 ± 0.04 | |
| 61 | 706.52 | 0.18 ± 0.04 | |
| 62 | 709.10 | 0.14 ± 0.04 | $^{27}Al(\alpha,n)^{30}P$ |
| 63 | 728.63 | 0.94 ± 0.05 | |
| 64 | 741.36 | 0.55 ± 0.05 | |
| 65 | 749.21 | 0.60 ± 0.05 | |
| 66 | 772.75 | 0.71 ± 0.05 | |
| 67 | 783.08 | 1.31 ± 0.05 | $^{115}Sn$ |
| 68 | 800.22 | 0.42 ± 0.05 | |
| 69 | 804.09 | 3.18 ± 0.05 | $^{115}Sn, ^{52}Cr(\alpha,n)^{55}Fe$ |
| 70 | 806.37 | 1.08 ± 0.05 | |
| 71 | 829.38 | 1.31 ± 0.04 | |
| 72 | 831.84 | 0.35 ± 0.03 | |
| 73 | 834.40 | 0.40 ± 0.04 | |
| 74 | 846.76 | 9.12 ± 0.06 | $^{117}Sn$ |
| 75 | 858.80 | 0.82 ± 0.04 | |
| 76 | 861.54 | 0.37 ± 0.04 | $^{117}Sn$ |
| 77 | 870.57 | 0.41 ± 0.05 | $^{14}N(\alpha,p)^{17}O$ |

TABLE V (continued)

| Number | Energy (keV) | Intensity | Identification |
|---|---|---|---|
| 78 | 877.18 | 0.29 ± 0.05 | |
| 79 | 900.22 | 4.98 ± 0.06 | |
| 80 | 910.64 | 1.77 ± 0.05 | |
| 81 | 913.28 | 0.37 ± 0.05 | |
| 82 | 919.77 | 2.58 ± 0.06 | $^{115}Sn$,$^{119}Sn$ |
| 83 | 931.28 | 19.68 ± 0.08 | $^{52}Cr(\alpha,n)^{55}Fe$ |
| 84 | 991.48 | 1.54 ± 0.06 | |
| 85 | 986.54 | 6.76 ± 0.07 | $^{115}Sn$ |
| 86 | 991.51 | 1.20 ± 0.06 | |
| 87 | 1014.18 | 0.54 ± 0.06 | $^{24}Mg(\alpha,p)^{27}Al$ |
| 88 | 1022.73 | 1.31 ± 0.06 | |
| 89 | 1025.18 | 0.91 ± 0.05 | |
| 90 | 1039.45 | 3.37 ± 0.06 | $^{63}Cu(\alpha,p)^{66}Zn$ |
| 91 | 1157.06 | 1.64 ± 0.06 | |
| 92 | 1171.31 | 0.43 ± 0.06 | $^{120}Sn$,$^{62}Ni$ |
| 93 | 1202.00 | 0.64 ± 0.06 | |
| 94 | 1215.62 | 1.10 ± 0.06 | |
| 95 | 1222.78 | 2.90 ± 0.07 | |
| 96 | 1227.56 | 18.92 ± 0.09 | |
| 97 | 1238.16 | 3.02 ± 0.06 | |
| 98 | 1240.66 | 0.63 ± 0.05 | |
| 99 | 1266.21 | 3.89 ± 0.07 | $^{28}Si(\alpha,p)^{31}P$ |
| 100 | 1269.88 | 1.25 ± 0.06 | |
| 101 | 1279.90 | 15.52 ± 0.08 | $^{115}Sn$ |
| 102 | 1282.99 | 0.81 ± 0.06 | |
| 103 | 1293.48 | 2.99 ± 0.06 | |
| 104 | 1296.13 | 0.42 ± 0.06 | $^{116}Sn$ |
| 105 | 1303.23 | 0.47 ± 0.06 | |
| 106 | 1316.39 | 12.66 ± 0.08 | |
| 107 | 1332.62 | 0.26 ± 0.06 | $^{60}Ni$ |
| 108 | 1347.22 | 0.85 ± 0.06 | |
| 109 | 1369.27 | 2.42 ± 0.05 | $^{24}Mg$ |
| 110 | 1372.20 | 0.79 ± 0.05 | |
| 111 | 1408.26 | 4.08 ± 0.07 | |
| 112 | 1416.78 | 9.77 ± 0.08 | $^{115}Sn$ |
| 113 | 1433.88 | 1.80 ± 0.06 | |
| 114 | 1454.22 | 0.46 ± 0.05 | $^{58}Ni$ |
| 115 | 1460.66 | 0.68 ± 0.05 | $^{40}K$ decay |
| 116 | 1508.98 | 0.32 ± 0.04 | |
| 117 | 1511.27 | 0.44 ± 0.04 | |
| 118 | 1524.49 | 43.29 ± 0.13 | $^{42}Ca$ |

TABLE V (continued)

| Number | Energy (keV) | Intensity | Identification |
|---|---|---|---|
| 119 | 1529.72 | 2.37 ± 0.05 | |
| 120 | 1533.06 | 0.27 ± 0.05 | |
| 121 | 1572.69 | 0.32 ± 0.05 | |
| 122 | 1575.88 | 0.89 ± 0.05 | |
| 123 | 1603.67 | 0.40 ± 0.05 | |
| 124 | 1626.27 | 0.32 ± 0.05 | |
| 125 | 1643.87 | 1.41 ± 0.06 | |
| 126 | 1697.89 | 0.47 ± 0.05 | |
| 127 | 1728.16 | 0.47 ± 0.04 | |
| 128 | 1730.06 | 0.46 ± 0.03 | |
| 129 | 1732.29 | 0.93 ± 0.04 | |
| 130 | 1734.59 | 0.70 ± 0.04 | |
| 131 | 1736.59 | 0.37 ± 0.05 | |
| 132 | 1778.44 | 5.44 ± 0.07 | $^{28}Si$ |
| 133 | 1780.99 | 0.99 ± 0.05 | |
| 134 | 1784.41 | 0.41 ± 0.06 | |
| 135 | 1814.53 | 0.45 ± 0.05 | |
| 136 | 1815.81 | 0.20 ± 0.04 | |

The γ-ray spectrum was divided into three parts and two calibrated γ-rays in each section were used to adjust the gain slope converting channels to keV. The 115.44, 511.01, 986.54, and 1460.81 keV γ-rays were used for these calibration points. The energy location of the other γ-rays is expected to be better than ± 0.5 keV in all cases. The energies of all Sn γ-rays were determined individually and are expected to be good to within the one standard deviation values quoted.

Identification of the $^{55}$Fe contaminant γ-rays is based on the coincident observation of all γ-rays from this element. This contaminant probably resulted from the $^{52}$Cr(α,n)$^{55}$Fe reaction on chrome contaminants in the target. This contaminant was particularly troublesome for the 804 keV $^{115}$Sn γ-ray which was almost coincident with an $^{55}$Fe γ-ray. A high yield of the 136.25 keV γ-ray was observed on the first run with the 28.52% target because the α beam was striking the Ta defining slits near the detector causing this Coulomb excited γ-ray. The $^{115}$Sn γ-ray energy is 136.70 keV. The second run with the 92.31% target was made with these slits withdrawn. Several of these identified contaminant γ-rays are listed in the section on Coulomb Excitation by McGowan and Stelson in Nuclear Spectroscopy and Reactions, Part C.[53]

## Energy Levels

Figure 22 shows the energy level diagram deduced for $^{115}$Sn from the experimental evidence collected in this study. Note

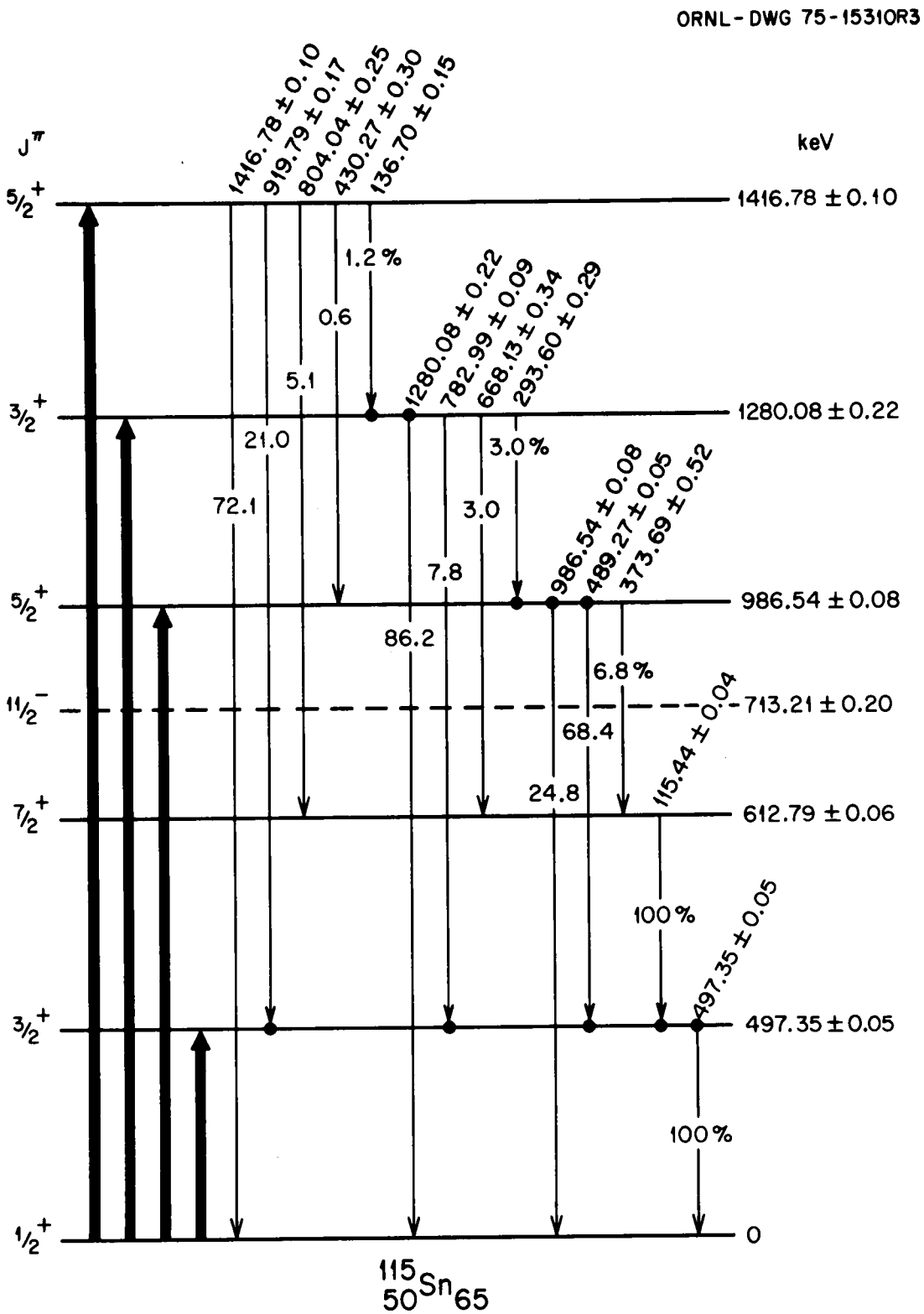


Figure 22. Energy level diagram of $^{115}$Sn with branching ratios.

particularly that the heavy vertical arrows point to levels that are Coulomb excited. Descending arrows represent decay γ-rays. A dot on the top of an arrow indicates a coincidence was observed with γ-rays feeding the level from which it decays. A dot on the bottom of an arrow indicates a coincidence was seen with γ-rays decaying from the level the γ-ray feeds. The numbers contained within the arrow breaks are the branching ratios in percent from that level. The $11/2^-$ level at 713.21 keV was not Coulomb excited, but has been included for completeness from the reaction work of Schwengler,[9] Cavanagh et al.,[7] Fleming et al.,[6] Schneid et al.,[5] and from Nuclear Data Sheets.[55]

Internal Conversion Coefficients

Table VI presents the $^{115}$Sn γ-rays observed in the present study and a listing of the total internal conversion coefficients for pure E2 and M1 transitions. Also listed are the mixing ratios deduced during this study for these γ-rays and the total internal conversion coefficient for these mixtures. These internal coefficients are derived from the work of Sliv and Band.[54]

Reduced Transition Probability

Table VII presents a summary of the reduced transition probabilities for excitation, $B_{ex}(E2)$ deduced for $^{115}$Sn. Also listed are the $J^\pi$ values for these levels. The $B_{ex}(E2)$ values for the 497 and 1416 keV levels were also confirmed by a $^{115}$Sn$(\alpha,\alpha')^{115}$Sn measurement to be presented in a subsequent section.

TABLE VI

Gamma-ray energies and internal conversion coefficients for $^{115}Sn$

| $E_\gamma$ (keV) | $\alpha_T(E2)$ | $\beta_T(M1)$ | $\delta$ | $\alpha_T(E2 + M1)$ [a] |
|---|---|---|---|---|
| 1416.78 | 0.00060 | | $\infty$ | 0.00060 |
| 1280.08 | 0.00074 | 0.00089 | $0.09 \pm 0.01$ | 0.00089 |
| | | | $-2.2 \pm 0.2$ | 0.00077 |
| 986.54 | 0.00129 | | $\infty$ | 0.00129 |
| 919.79 | 0.00151 | 0.00192 | $0.17 \pm 0.03$ | 0.00191 |
| | | | $-8.2 \pm 2.3$ | 0.00152 |
| 804.04 | 0.00207 | 0.00261 | | 0.00207 |
| 782.99 | 0.00221 | 0.00278 | $0.77^{+0.83}_{-0.46}$ | 0.00257 |
| 668.13 | 0.00329 | 0.00402 | | 0.00329 |
| 497.35 | 0.00751 | 0.00817 | $0.21 \pm 0.02$ | 0.00814 |
| | | | $-3.0 \pm 0.3$ | 0.00758 |
| 489.27 | 0.00786 | 0.00850 | $0.040 \pm 0.023$ | 0.00850 |
| | | | $-4.0 \pm 0.35$ | 0.00790 |
| 430.27 | 0.01145 | 0.01170 | $0.55^{+1.65}_{-0.55}$ | 0.01164 |
| 373.69 | 0.01759 | 0.01663 | $-0.265 \pm 0.062$ | 0.01669 |
| 293.60 | 0.03817 | 0.03072 | $0.38^{+0.25}_{-0.16}$ | 0.03166 |

TABLE VI (continued)

| $E_\gamma$ (keV) | $\alpha_T$(E2) | $\beta_T$(M1) | $\delta$ | $\alpha_T$(E2 + M1)[a] |
|---|---|---|---|---|
| 136.70 | 0.5282 | 0.2375 | $0.17 \pm 0.15$ | <u>0.2457</u> |
| | | | $-7.8^{+4.1}_{-\infty}$ | 0.5235 |
| 115.44 | 0.9672 | | $\infty$ | <u>0.9672</u> |

[a] Values underlined are adapted values for this study.

[b] $\alpha_T$(E2) is the E2 total internal conversion coefficient
$\beta_T$(M1) is the M1 total internal conversion coefficient
$\alpha_T$(E2 + M1) is the total internal conversion coefficient
$\delta$ is the mixing ratio, E2/M1.

TABLE VII

Summary of the $B_{ex}(E2)$ values obtained for $^{115}Sn$ from in-beam $\gamma$-ray measurements

| E (keV) | $J^{\pi}$ | $B_{ex}(E2)$ $(e^2 \cdot fm^4)$ |
|---|---|---|
| 497.35 | $3/2^+$ | 140 ± 8 |
| 986.54 | $5/2^+$ | 227 ± 10 |
| 1280.08 | $3/2^+$ | 444 ± 37 |
| 1416.78 | $5/2^+$ | 598 ± 33 |

Doppler Shift Measurements

Table VIII presents the values taken for the effective stopping power of tin atoms in tin used to calculate Doppler broadened $\gamma$-ray peak shapes using programs DOPCO and TUTTLAID mentioned earlier in Chapter IV Section G. The Dagenhart/Stelson values are the values of Stelson et al.[4] where defined by their work. The Dagenhart values are very close to the optimum values used in the Doppler shift line studies by Tuttle[56] on $^{113,115}$In. The Dagenhart values give a slightly better line shape fit.

Figure 23 shows a plot of the 1280.1 keV and 1416.8 keV Doppler broadened $\gamma$-ray peaks observed when $^{115}$Sn was Coulomb excited with 45 MeV $^{16}$O projectiles. The detector was located at 0° to the beam. Figure 24 shows a plot of the 986.5 keV Doppler broadened $\gamma$-ray peak observed when $^{115}$Sn was Coulomb excited with 45 MeV $^{16}$O projectiles. The detector was located at 90° to the beam. The contaminant $\gamma$-ray line at $\sim$ 991 keV prevented the use of the 0° data for this $\gamma$-ray. The fit was determined mostly by using the lower shoulder of the peak and the peak itself. The different curves are calculated using programs DOPCO and TUTTLAID for different values of the mean-life, $\tau$, in psec.

Table IX presents the calculated lifetimes for $^{115}$Sn states using Dagenhart and Dagenhart/Stelson stopping power tables and the $^{115}$Sn$(\alpha,\alpha'\gamma)^{115}$Sn Doppler shift measurements.

TABLE VIII

Values taken for the effective stopping power of tin atoms in tin used to calculate Doppler broadened γ-ray peak shapes

| E (meV) | S(E) ($MeV \cdot cm^2 \cdot mg^{-1}$) Dagenhart | Dagenhart/Stelson |
|---|---|---|
| 0.01 | 100 | 100 |
| 0.02 | 69.0 | 69.0 |
| 0.04 | 48.5 | 48.5 |
| 0.07 | 36.5 | 36.5 |
| 0.100 | 30.5 | 26.0 |
| 0.200 | 22.0 | 22.0 |
| 0.400 | 15.5 | 15.5 |
| 0.700 | 10.5 | 10.5 |
| 1.0 | 7.70 | 7.70 |
| 2.0 | 4.32 | 4.80 |
| 4.0 | 4.77 | 4.00 |
| 7.0 | 5.49 | 3.80 |
| 10.0 | 6.39 | 4.30 |
| 20 | 9.00 | 6.40 |
| 40 | 13.6 | 13.6 |
| 70 | 18.5 | 18.5 |
| 100 | 21.8 | 21.8 |
| 200 | 26.5 | 26.5 |
| 400 | 27.1 | 27.1 |
| 700 | 25.2 | 25.2 |

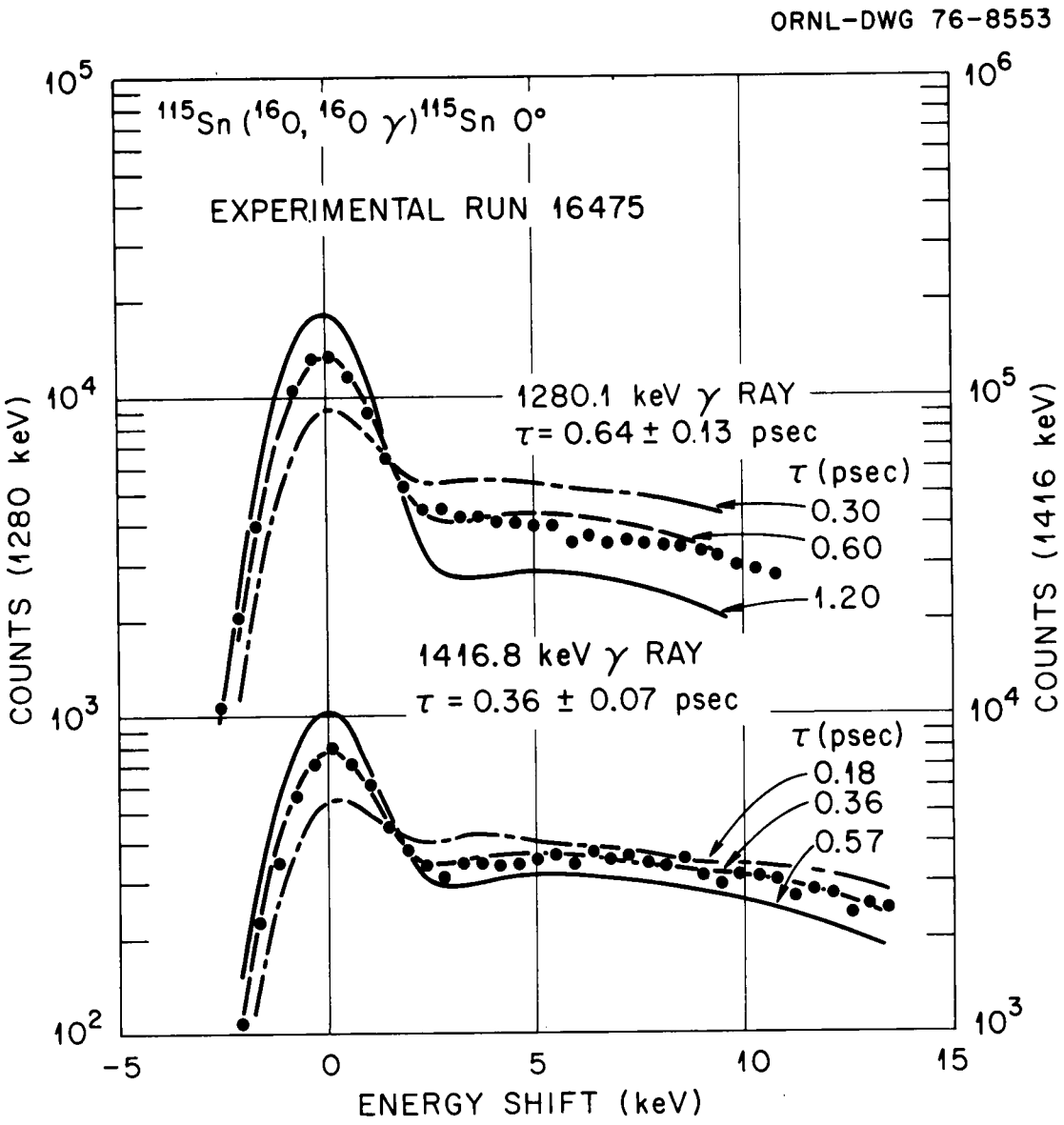


Figure 23. Doppler broadened $\gamma$-ray peaks observed when $^{115}$Sn was Coulomb excited with 45 MeV $^{16}$O projectiles. The detector was located at 0° to the beam. The curves are calculated for different values of the mean-life, $\tau$, in psec.

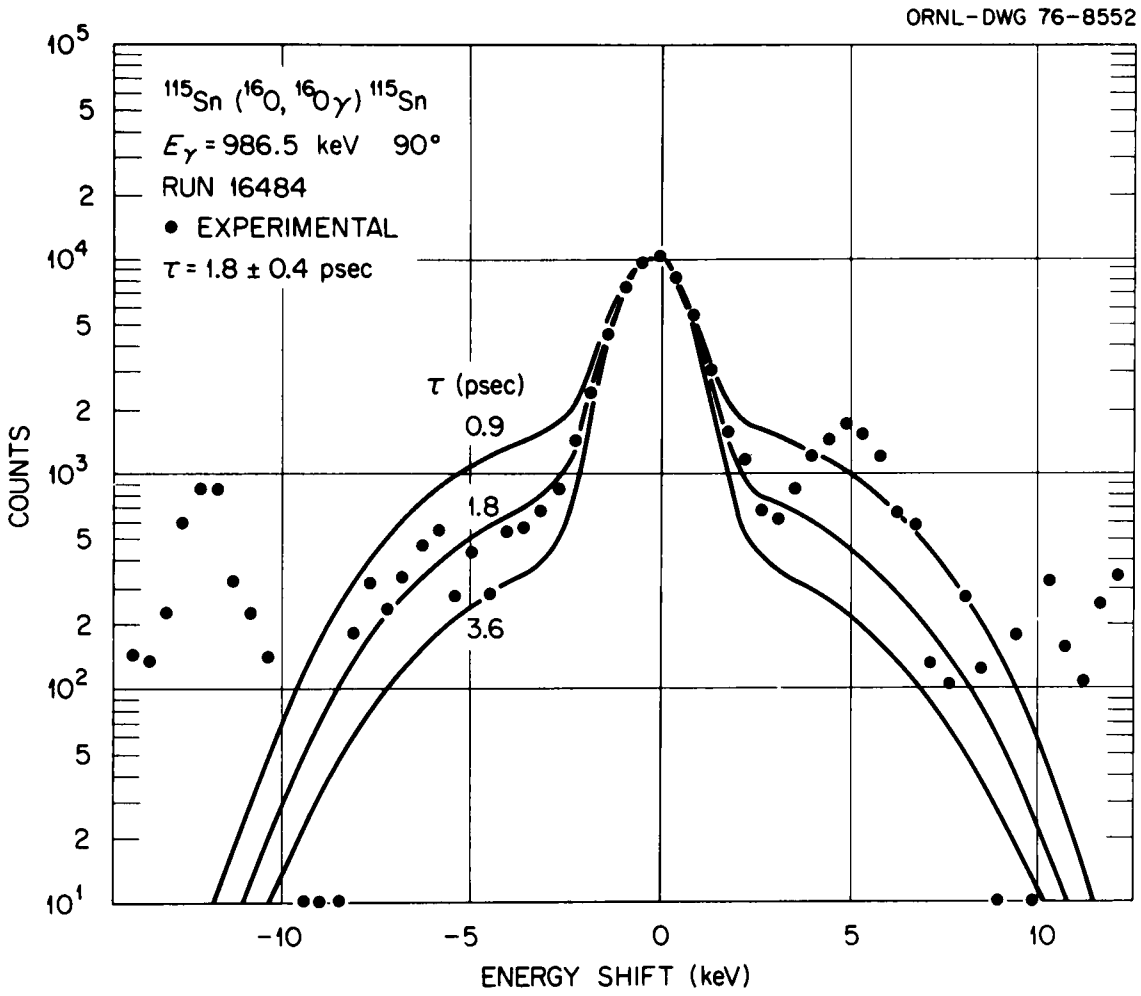


Figure 24. Doppler broadened $\gamma$-ray peak observed when $^{115}$Sn was Coulomb excited with 45 MeV $^{16}$O projectiles. The detector was located at 90° to the beam. The curves are calculated for different values of the mean-life, $\tau$, in psec.

TABLE IX

Calculated lifetimes for $^{115}Sn$ states using Dagenhart and Dagenhart/Stelson stopping power tables and the $^{115}Sn(\alpha,\alpha'\gamma)^{115}Sn$ Doppler shift measurements

| E (meV) | τ (psec) Dagenhart S(E) | τ (psec) Dagenhart/Stelson S(E) |
|---|---|---|
| 1416.78 | 0.36 ± 0.07[b] | 0.35 ± 0.07[a] |
| 1280.08 | 0.64 ± 0.13[a],[b] | 0.66 ± 0.13 |
| 986.54 | 1.8 ± 0.4[a],[b] | 2.1 ± 0.4 |

[a] Value of τ which gave best fit to the Doppler shifted γ-ray peak shape.

[b] Value adopted for this study.

## B. GAMMA-RAY ANISOTROPIES

Table X presents a summary of the γ-ray anisotropy results for $^{115}$Sn. Column 3 lists the measured R values where R = W(0°)/W(90°), the ratio of the 0° to 90° γ-ray intensity. Column 4 lists the unique theoretical value for the $\frac{1}{2}$ (E2) $\frac{5}{2}$ (E2) $\frac{1}{2}$ transition. Column 5 lists $(a_2)_t$ which is calculated using program DIREKE2 mentioned earlier. Column 6 is $g_2$ the finite angular resolution correction factor for the detector geometry used. Column 7 gives the calculated value of $A_2$ using

$$A_2 = \frac{R-1}{(a_2)_t g_2(1 + \frac{R}{2})} \quad . \qquad \text{(V-1)}$$

Figures 25, 26, 27, 28, 29, 30, 31, 32, and 33 are plots of the theoretical angular distribution coefficient $A_2$ versus δ for the indicated spin sequences. These are calculated using the methods and tables of Ferentz and Rosenzweig.[57] Also plotted are the experimental values of $A_2$ from Table X. The experimental values for δ are extracted from the plots using the experimental $A_2$ values at their intersections with the δ versus $A_2$ curves.

## C. GAMMA-GAMMA COINCIDENCE

Table XI presents a summary of the coincidence information obtained from the Coulomb excitation of $^{115}$Sn. In column 2 are listed those γ-rays which are definitely in coincidence with the γ-rays of

TABLE X

Summary of γ-ray anisotropy results for $^{115}Sn$

| $E_\gamma$ (keV) | $E_\alpha$ (MeV) | R | $R(\frac{5}{2})$ | $(a_2)_t$ | $g_2$ | $A_2$ |
|---|---|---|---|---|---|---|
| 1416.78 | 10.0 | 1.38 ± 0.02 | 1.433 | 0.9648 | 0.9468 | 0.257 ± 0.014 |
| 1280.08 | 10.0 | 0.795 ± 0.006 | 1.419 | 0.9348 | 0.9467 | -0.166 ± 0.005 |
| 986.54 | 10.0 | 1.38 ± 0.02 | 1.353 | 0.8529 | 0.9466 | 0.277 ± 0.013 |
| 919.79 | 10.0 | 0.963 ± 0.044 | | 0.9648 | 0.9466 | -0.027 ± 0.033 |
| 782.99 | 10.0 | 1.81 ± 0.11 | | 0.9348 | 0.9465 | +0.480 ± 0.067 |
| 497.35 | 7.0 | 0.930 ± 0.014 | 1.272 | 0.7913 | 0.9456 | -0.064 ± 0.013 |
| 489.27 | 10.0 | 0.819 ± 0.027 | | 0.8529 | 0.9455 | -0.160 ± 0.024 |
| 430.27 | 10.0 | 1.66 ± 0.38 | | 0.9648 | 0.9449 | 0.40 ± 0.23 |
| 373.69 | 10.0 | 1.134 ± 0.042 | | 0.8529 | 0.9440 | 0.106 ± 0.033 |
| 293.60 | 10.0 | 1.39 ± 0.14 | | 0.9348 | 0.9418 | 0.261 ± 0.092 |
| 136.70 | 10.0 | 0.96 ± 0.19 | | 0.9648 | 0.9286 | -0.033 ± 0.146 |

Column 3 shows the observed $R = W(0°)/W(90°)$ for the γ-ray listed in column 1 at the α-particle bombarding energy listed in column 2. The column headed $R(\frac{5}{2})$ gives the unique value for R when the spin sequence is $\frac{1}{2} \xrightarrow{E2} \frac{5}{2} \xrightarrow{E2} \frac{1}{2}$. The $(a_2)_t$ is the thick-target particle parameter for the Coulomb excitation process. The quantity $g_2$ is the finite solid-angle correction factor. The last column headed $A_2$ is the individual extracted coefficient for the $P_2$ Legendre polynomial of the angular distribution of the γ-rays.

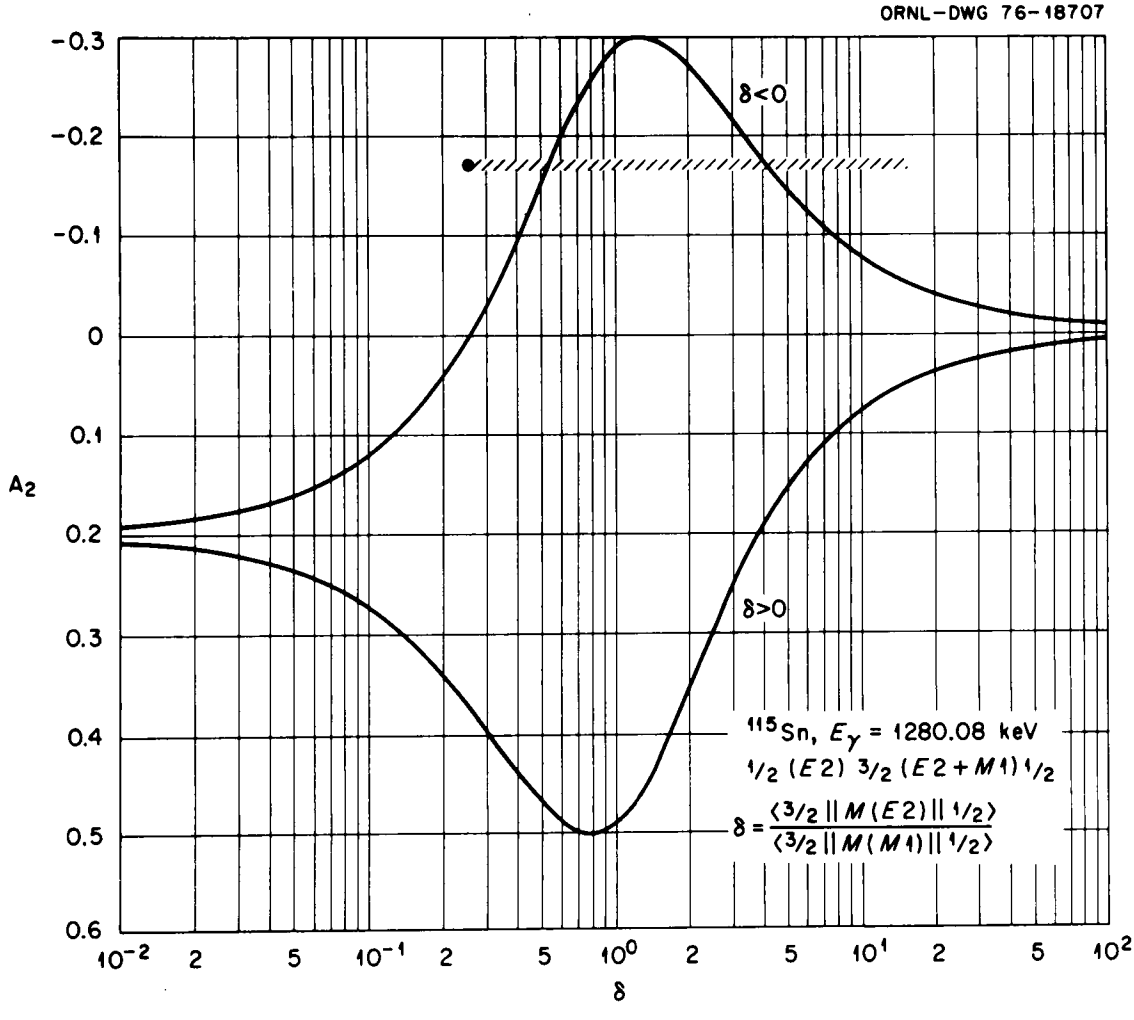


Figure 25. The angular distribution coefficient $A_2$ vs $\delta$ for the spin sequence $\frac{1}{2}(E2)\ \frac{3}{2}(E2 + M1)\frac{1}{2}$ including experimental results for $^{115}Sn$, $E_\gamma$ = 1280.08 keV.

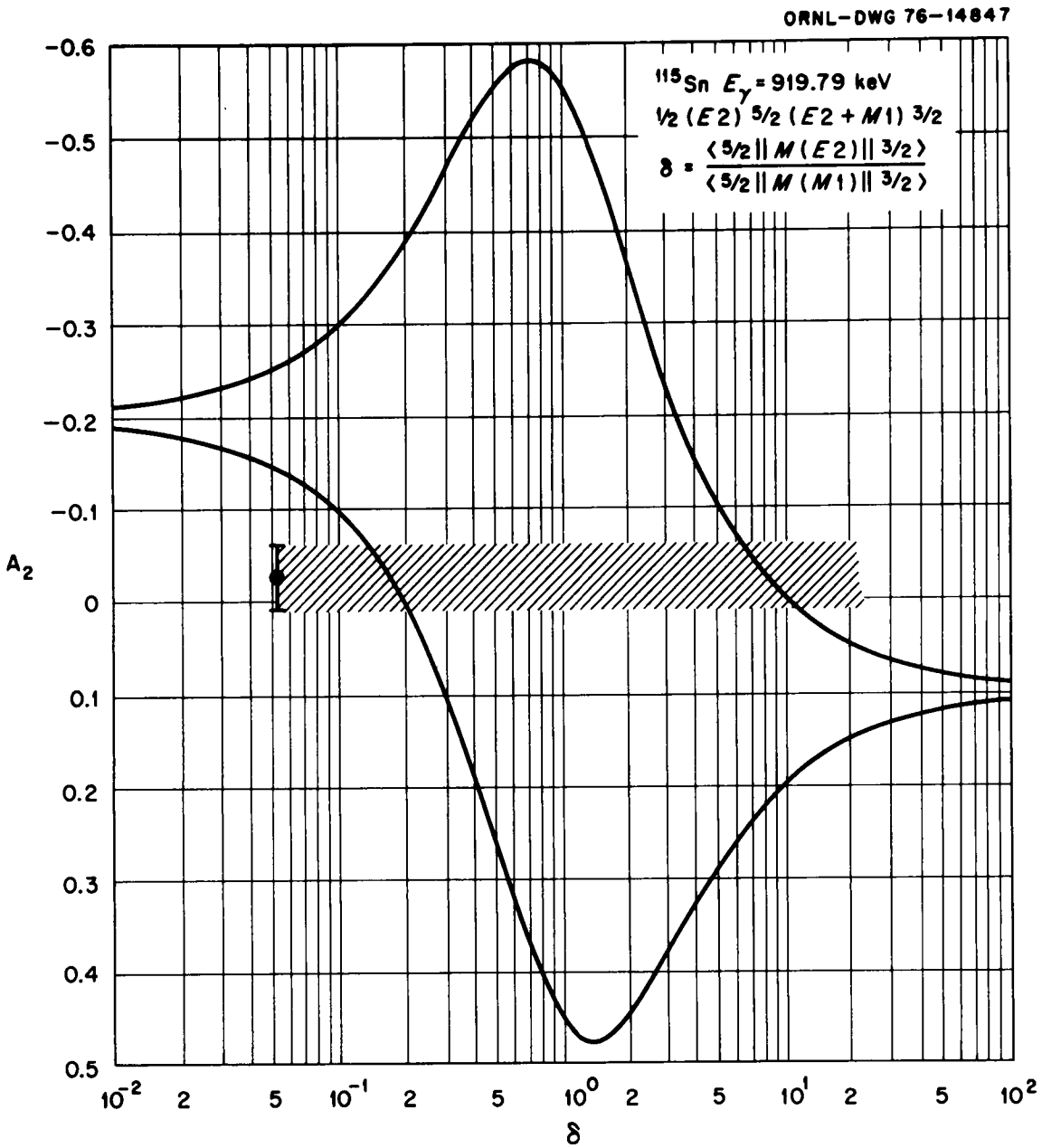


Figure 26. The angular distribution coefficient $A_2$ vs $\delta$ for the spin sequence $\frac{1}{2}$(E2) $\frac{5}{2}$(E2 + M1)$\frac{3}{2}$ including experimental results for $^{115}$Sn, $E_\gamma$ = 919.79 keV.

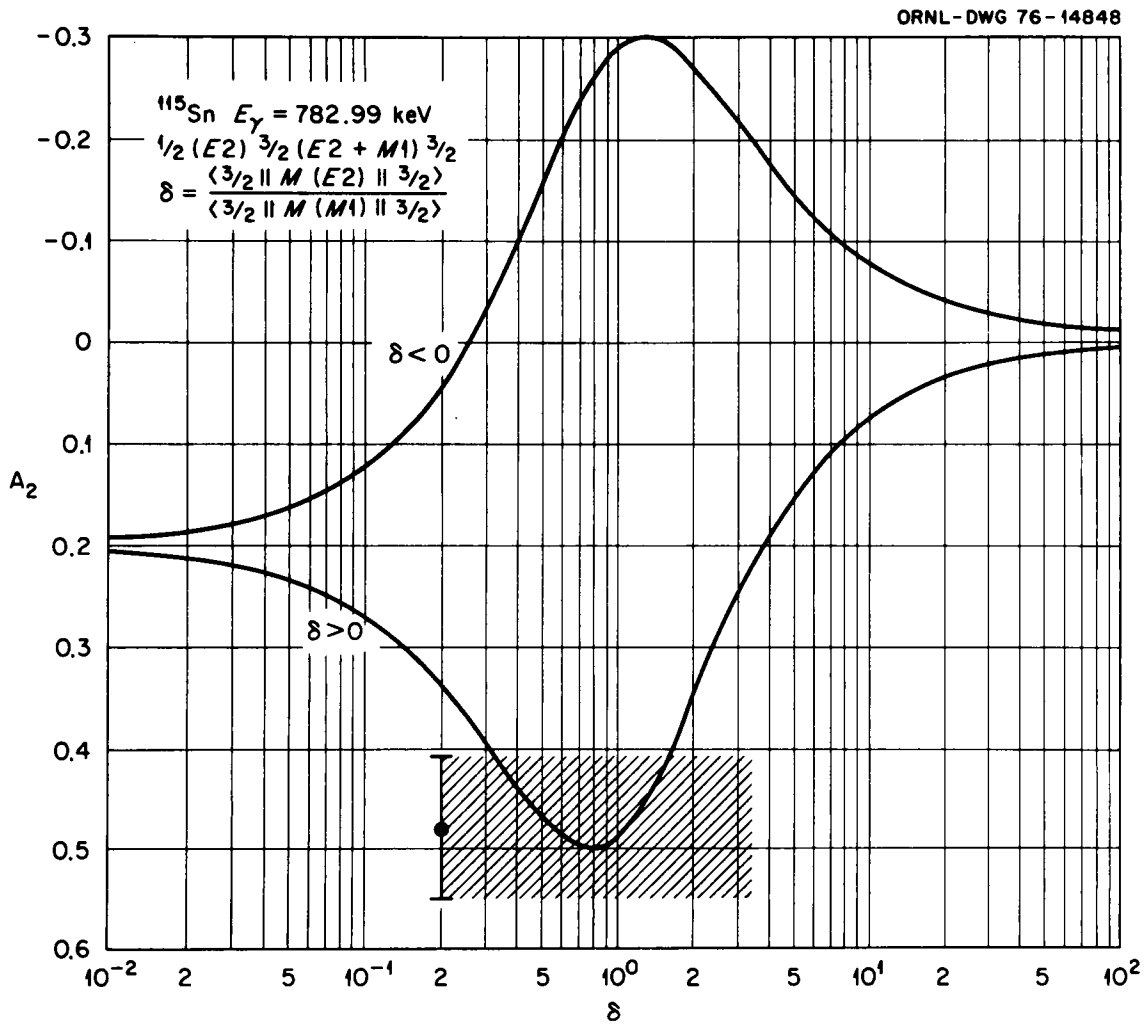


Figure 27. The angular distribution coefficient $A_2$ vs δ for the spin sequence $\frac{1}{2}$(E2) $\frac{3}{2}$(E2 + M1)$\frac{3}{2}$ including experimental results for $^{115}$Sn, $E_\gamma$ = 782.99 keV.

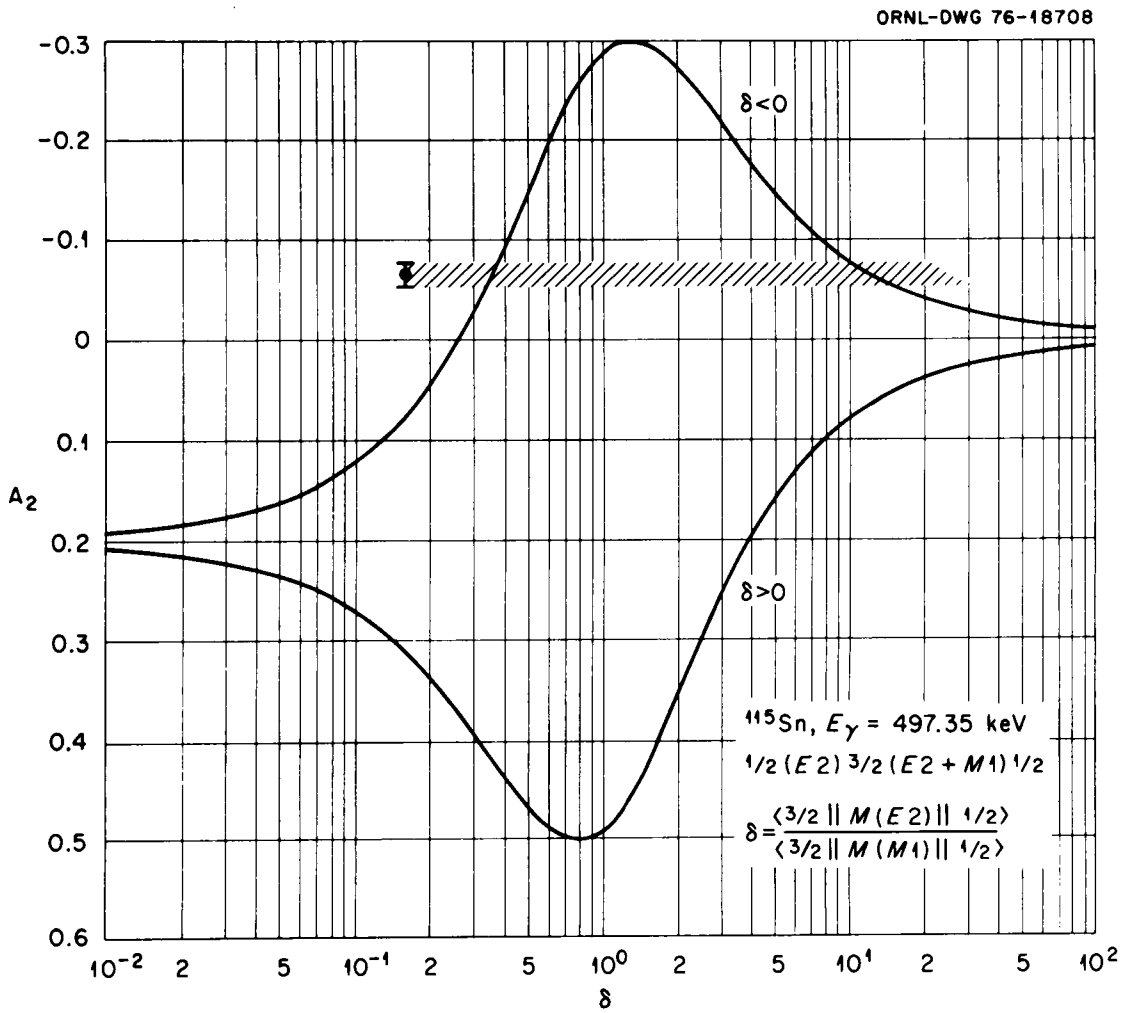


Figure 28. The angular distribution coefficient $A_2$ vs δ for the spin sequence $\frac{1}{2}$(E2) $\frac{3}{2}$(E2 + M1)$\frac{1}{2}$ including experimental results for $^{115}$Sn, $E_\gamma$ = 497.35 keV.

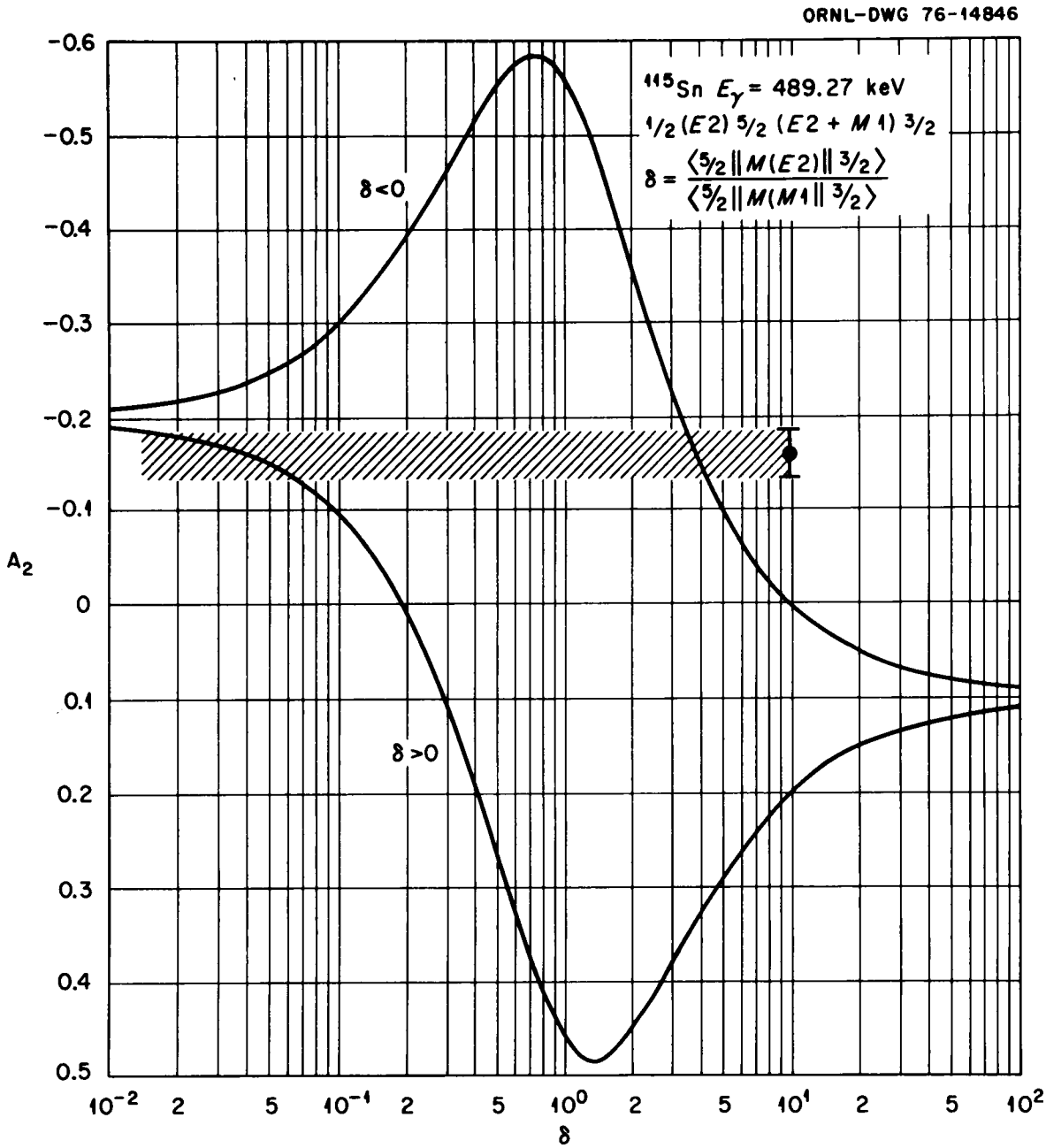


Figure 29. The angular distribution coefficient $A_2$ vs δ for the spin sequence $\frac{1}{2}$(E2) $\frac{5}{2}$(E2 + M1)$\frac{3}{2}$ including experimental results for $^{115}$Sn, $E_\gamma$ = 489.27 keV.

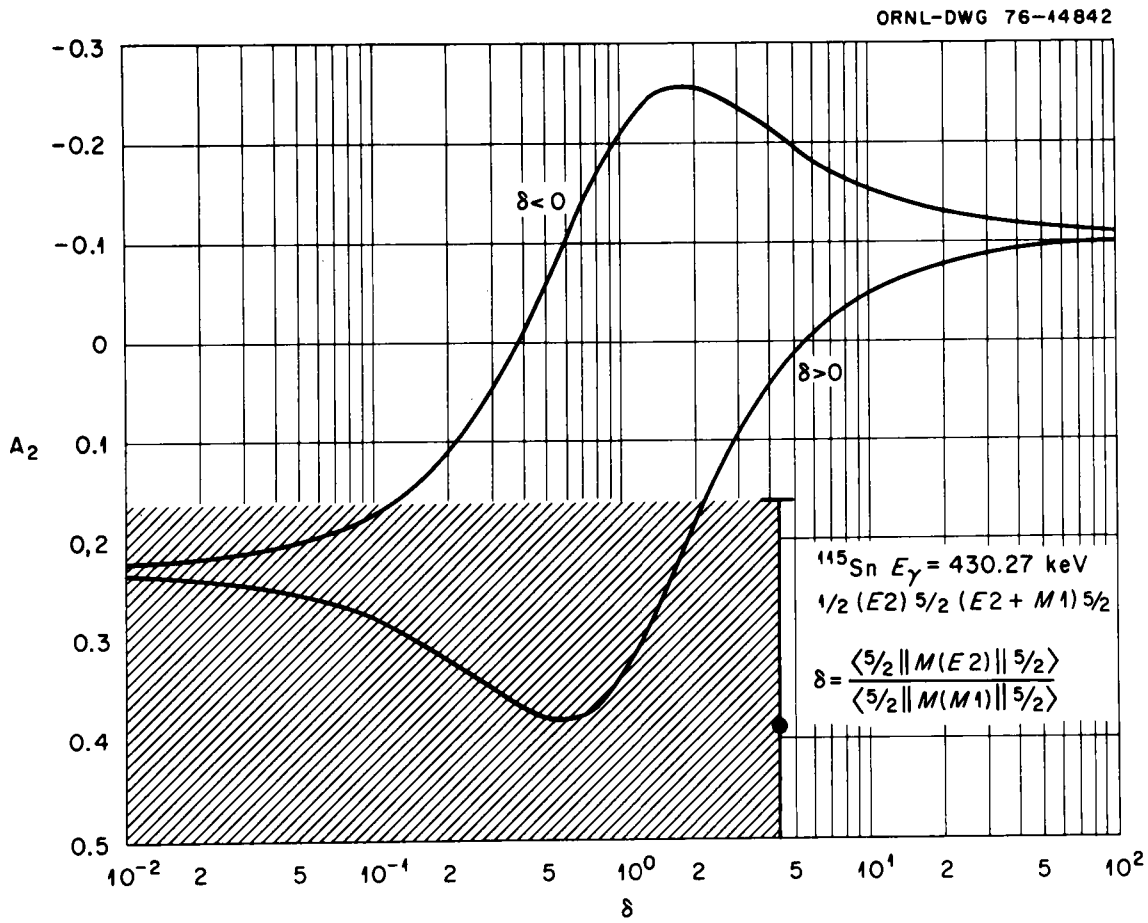


Figure 30. The angular distribution coefficient $A_2$ vs $\delta$ for the spin sequence $\frac{1}{2}(E2)\ \frac{5}{2}(E2 + M1)\frac{5}{2}$ including experimental results for $^{115}Sn$, $E_\gamma$ = 430.27 keV.

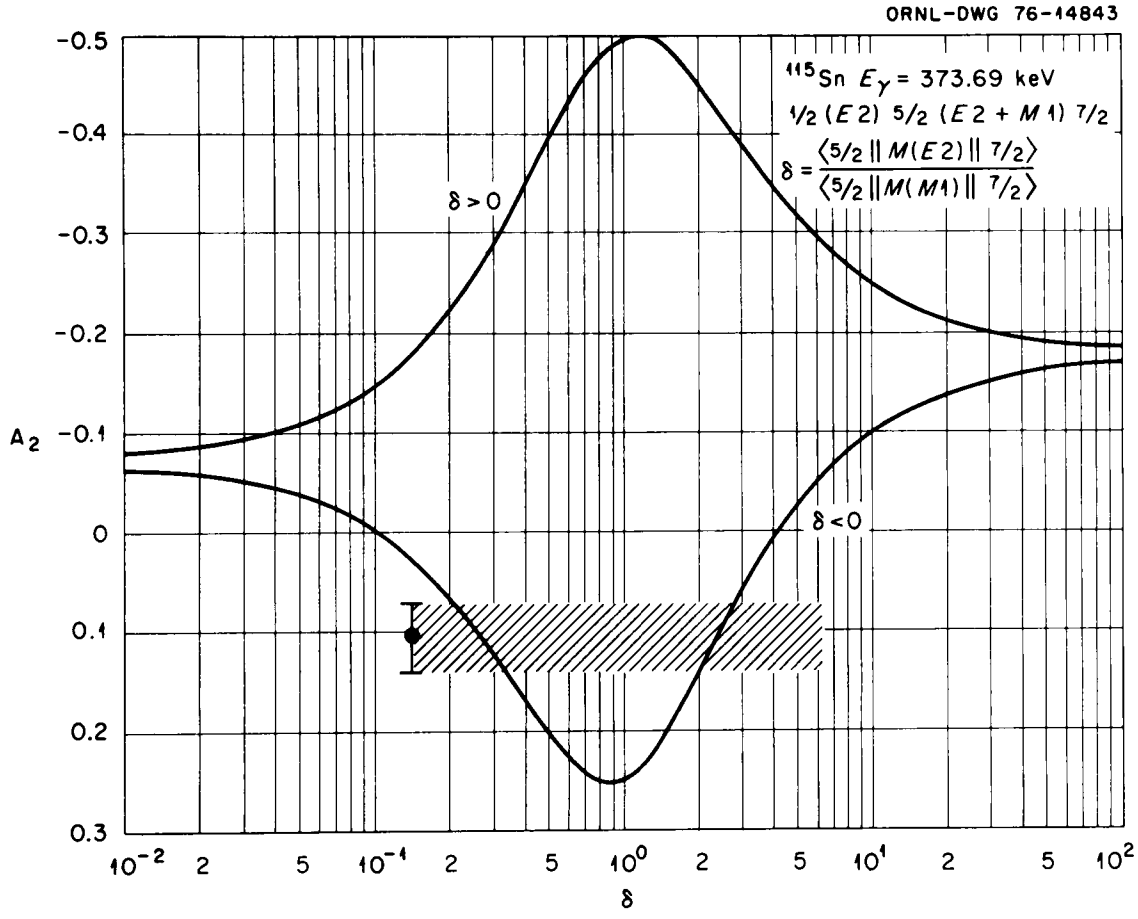


Figure 31. The angular distribution coefficient $A_2$ vs δ for the spin sequence $\frac{1}{2}$(E2) $\frac{5}{2}$(E2 + M1)$\frac{7}{2}$ including experimental results for $^{115}$Sn, $E_\gamma$ = 373.69 keV.

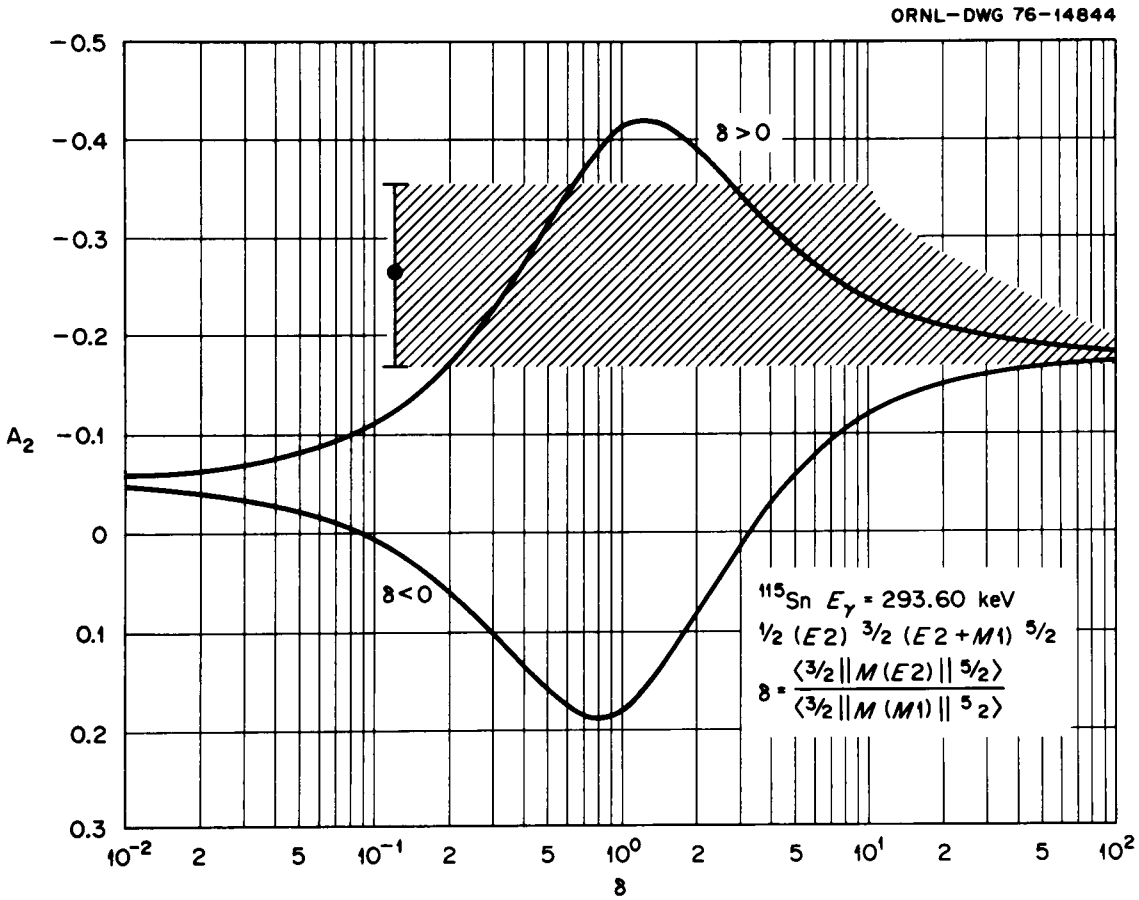


Figure 32. The angular distribution coefficient $A_2$ vs δ for the spin sequence $\frac{1}{2}$(E2) $\frac{3}{2}$(E2 + M1)$\frac{5}{2}$ including experimental results for $^{115}$Sn, $E_\gamma$ = 293.60 keV.

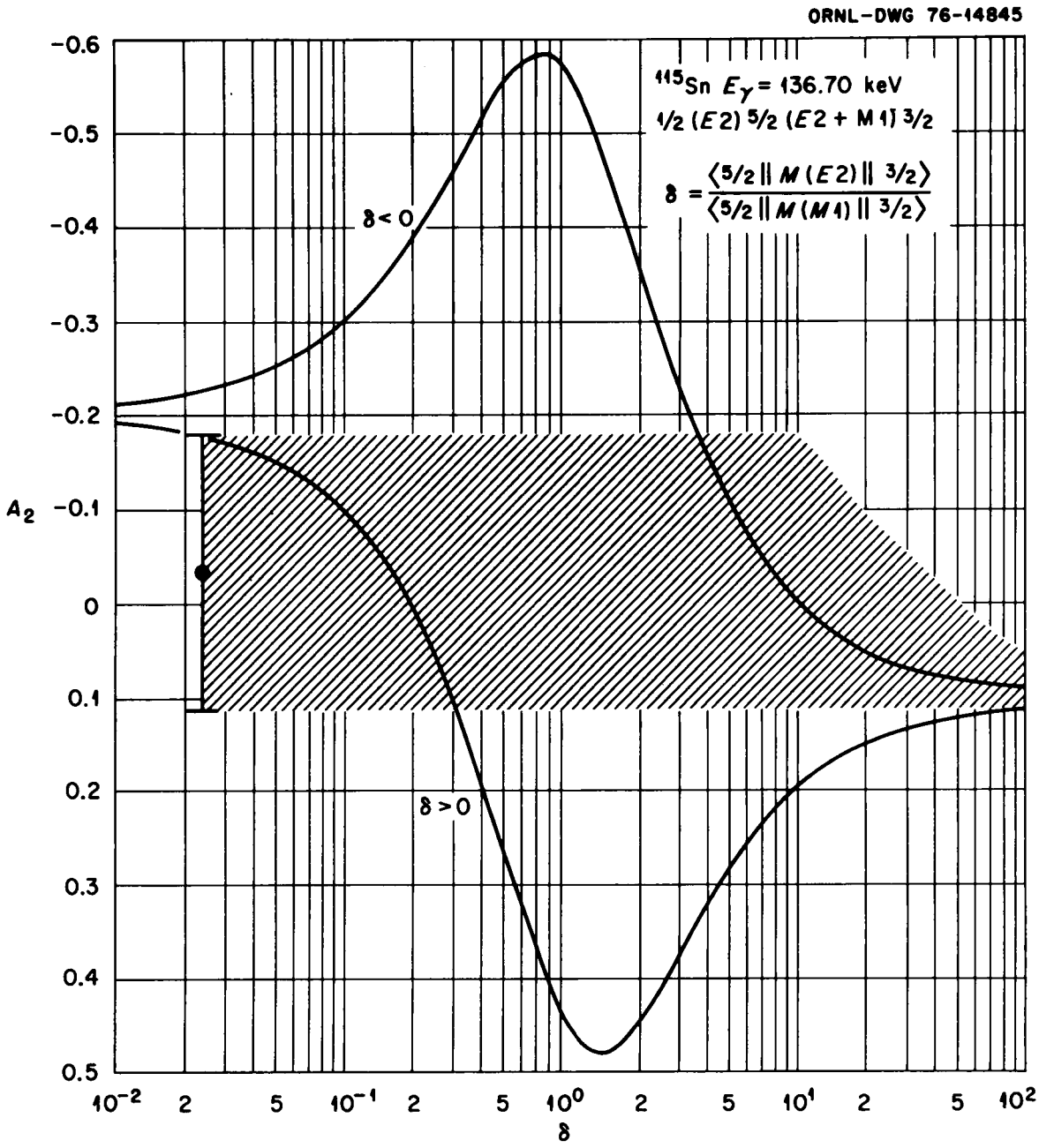


Figure 33. The angular distribution coefficient $A_2$ vs δ for the spin sequence $\frac{1}{2}$(E2) $\frac{5}{2}$(E2 + M1)$\frac{3}{2}$ including experimental results for $^{115}$Sn, $E_\gamma$ = 136.70 keV.

TABLE XI

Summary of coincidence information obtained from the Coulomb excitation of $^{115}Sn$

| Transition Energy (keV) | Coincident γ-rays (keV) | |
|---|---|---|
| | Definite | Possible |
| 115.44 | 497.4 | |
| 136.70 | 1280.1 | |
| 293.60 | 986.5, 489.3, 497.4 | |
| 373.69 | | |
| 430.27 | | |
| 489.27 | 497.4, 293.6 | |
| 497.35 | 489.3, 919.8, 783.0, 115.4, 430.3, 293.6 | 1136.7, 841.1, 1367.2, 1408.4 |
| 782.99 | 497.4 | |
| 919.79 | 497.4 | |
| 986.54 | 293.6 | |

column 1. Column 3 lists those γ-rays which may be in coincidence with the γ-rays of column 1.

## D. INELASTIC PARTICLE SPECTRA

In this section the methods used in the analysis of the $^{115}Sn(\alpha,\alpha')^{115}Sn$ are presented. First the theory is given and then the experimental results.

### Theory

Following the methods of Alder et al.[11] the differential cross section is given by the Rutherford law

$$d\sigma_R = \frac{1}{4} a^2 \sin^{-4}(\frac{\theta}{2}) d\Omega, \qquad \text{(V-2)}$$

where θ is the scattering angle in the center-of-mass system and a is half the distance of closest approach in a head-on collision.

Since we have assumed that the orbit of the particle is not significantly affected by the excitation process, the differential excitation cross section is given by

$$d\sigma_{ex} = P d\sigma_R, \qquad \text{(V-3)}$$

where P is the probability that the nucleus is excited in a collision in which the particle is scattered into the solid angle dΩ.

The symmetrized parameter a is defined by

$$a = \frac{Z_1 Z_2 e^2}{m_o v_i v_f} , \qquad \text{(V-4)}$$

where $v_i$ is the initial particle velocity, $v_f$ is the final particle velocity, $m_o$ is the reduced mass of the projectile and nucleus, and $Z_1$ and $Z_2$ are the projectile and target atomic numbers respectively. Alder[11] gives a numerical form for Equation (V-4) as

$$a = 0.07199\ (1 + A_1/A_2)\ \frac{Z_1 Z_2 (1 - \zeta)^{-1/2} 10^{-12} \text{cm}}{E_{\text{MeV}}} , \qquad \text{(V-5)}$$

where $A_1$ and $A_2$ are the projectile and target atomic number and E the projectile energy is measured in MeV. The parameter $\zeta$ is defined as

$$\zeta = \Delta E'/E, \qquad \text{(V-6)}$$

where

$$\Delta E' = (1 + A_1/A_2)\Delta E \qquad \text{(V-7)}$$

and $\Delta E$ represents the nuclear excitation energy.

The total differential cross-section for excitation of a given level may be expressed as

$$d\sigma_{ex}(E\lambda) = C_{E\lambda} E_{MeV}^{\lambda-2} (E_{MeV} - \Delta E'_{MeV})^{\lambda-1}$$

$$x\ B(E\lambda) df_{E\lambda}(\eta_i, \xi), \qquad \text{(V-8)}$$

where $\lambda$ is the order of the radiation. The constant $C_{E\lambda}$ is given by the following for the present case of $\lambda = 2$ excitation

$$C_{E2} = 4.819(1 + A_1/A_2) \frac{A_1}{Z_2^2} 10^{-24} cm^2. \qquad \text{(V-9)}$$

B(E2) is the reduced transition probability and the classical functions $df_{E2}/d\Omega(\eta_i \to \infty)$ are given in Table II.8 of Alder et al.[11] They are tabulated as a function of $\theta$ and $\xi$ where

$$\xi = \frac{Z_1 Z_2 A_1^{1/2}\ \Delta E'_{MeV}}{12.65(E_{MeV} - \frac{1}{2}\ \Delta E'_{MeV})^{3/2}}$$

$$x\ (1 + \frac{5}{32} (\frac{\Delta E'}{E})^2 + \ldots). \qquad \text{(V-10)}$$

Equating the differential excitation cross-section from Equation (V-3) with that of Equation (V-8) one may then solve for B(E2) as

$$P d\sigma_R = G(E,\xi) B(E2) \qquad \text{(V-11)}$$

where $d\sigma_R$ is calculated from Equation (V-2), $G(E,\xi)$ is calculated from tabulated data and P is the experimentally measured excitation probability. P is basically the ratio of the inelastic peak area for the particular transition involved to the elastic peak area in the spectra to be presented. Thus one may solve for $B_{ex}(E2)$ with only the uncertainty in peak areas having any significant effect on $B_{ex}(E2)$ accuracy. This determination of $B_{ex}(E2)$ will be compared with the value determined from in beam $\gamma$-ray work.

Experimental Spectra Data

Figure 34 shows the gated Enge magnet spectra for the reaction $^{115}Sn(\alpha,\alpha')^{115}Sn$ at 10.0 MeV for the 25 $\mu g/cm^2$ target using a 20 cm long position sensitive proportional detector. The background was too high and the counts too few to extract any data from the higher states. Only the 497.3 keV state provided useful data.

Figure 35 shows the spectra from the ungated Enge magnet spectra for the reaction $^{115}Sn(\alpha,\alpha')^{115}Sn$ at 9.5 MeV using the 75 $\mu g/cm^2$ target and the 60 cm position sensitive proportional detector. The thicker target, higher beam current, and higher peak to background ratio now result in useful data for all four Coulomb excited levels. The background ratios were particularly sensitive to good beam optics. Peak to background ratios of 10,000 to 1 were converted to 50,000 to 1 by several hours of beam tuning.

Figure 36 presents the gated Enge magnet spectrum for the reaction $^{115}Sn(\alpha,\alpha')^{115}Sn$ at 10.2 MeV using the 75 $\mu g/cm^2$ target

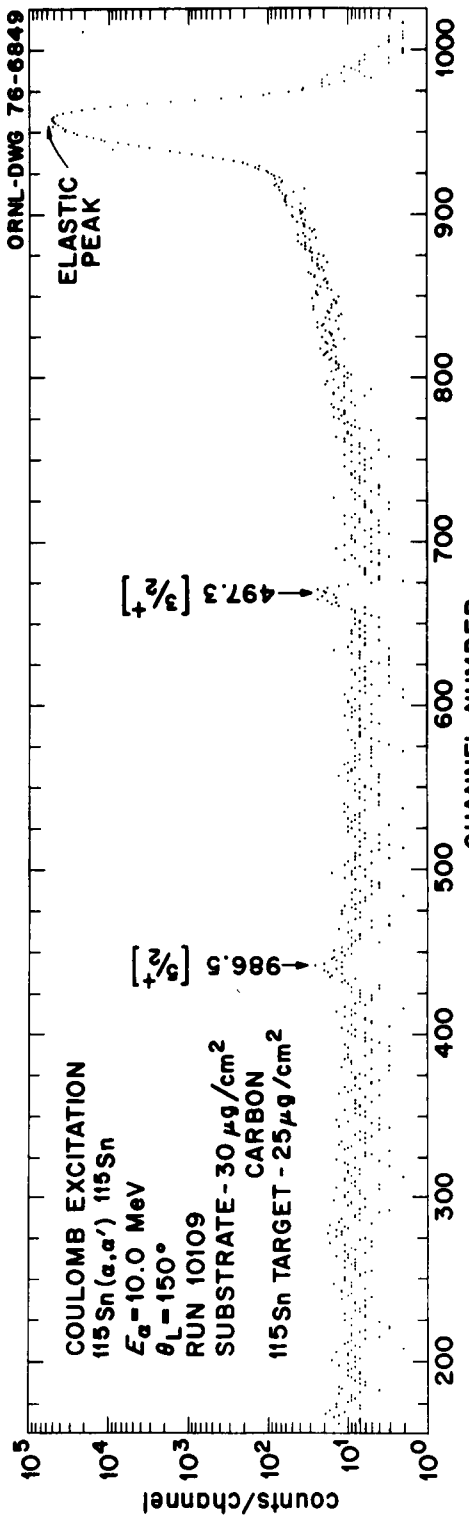


Figure 34. Gated Enge magnet spectra of $^{115}Sn(\alpha,\alpha')^{115}Sn$ reaction at 10.0 MeV for the 25 $\mu g/cm^2$ target using the 20 cm position sensitive detector.

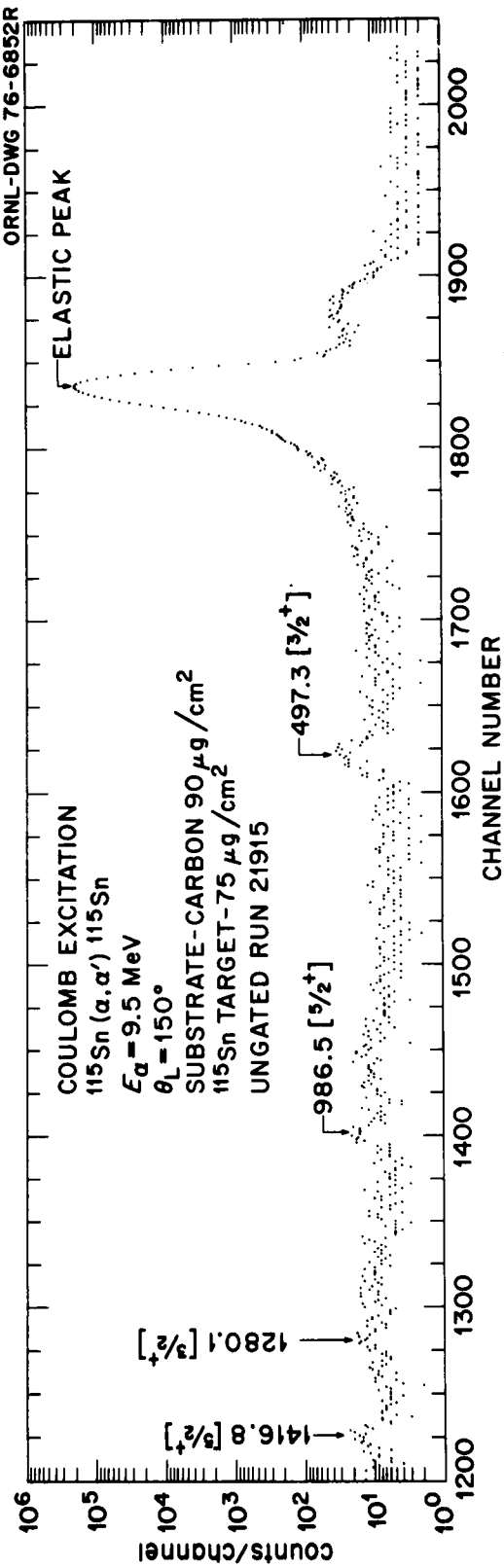


Figure 35. Ungated Enge magnet spectra of $^{115}Sn(\alpha,\alpha')^{115}Sn$ reaction at 9.5 MeV for the 75 μg/cm$^2$ target and the 60 cm position sensitive detector.

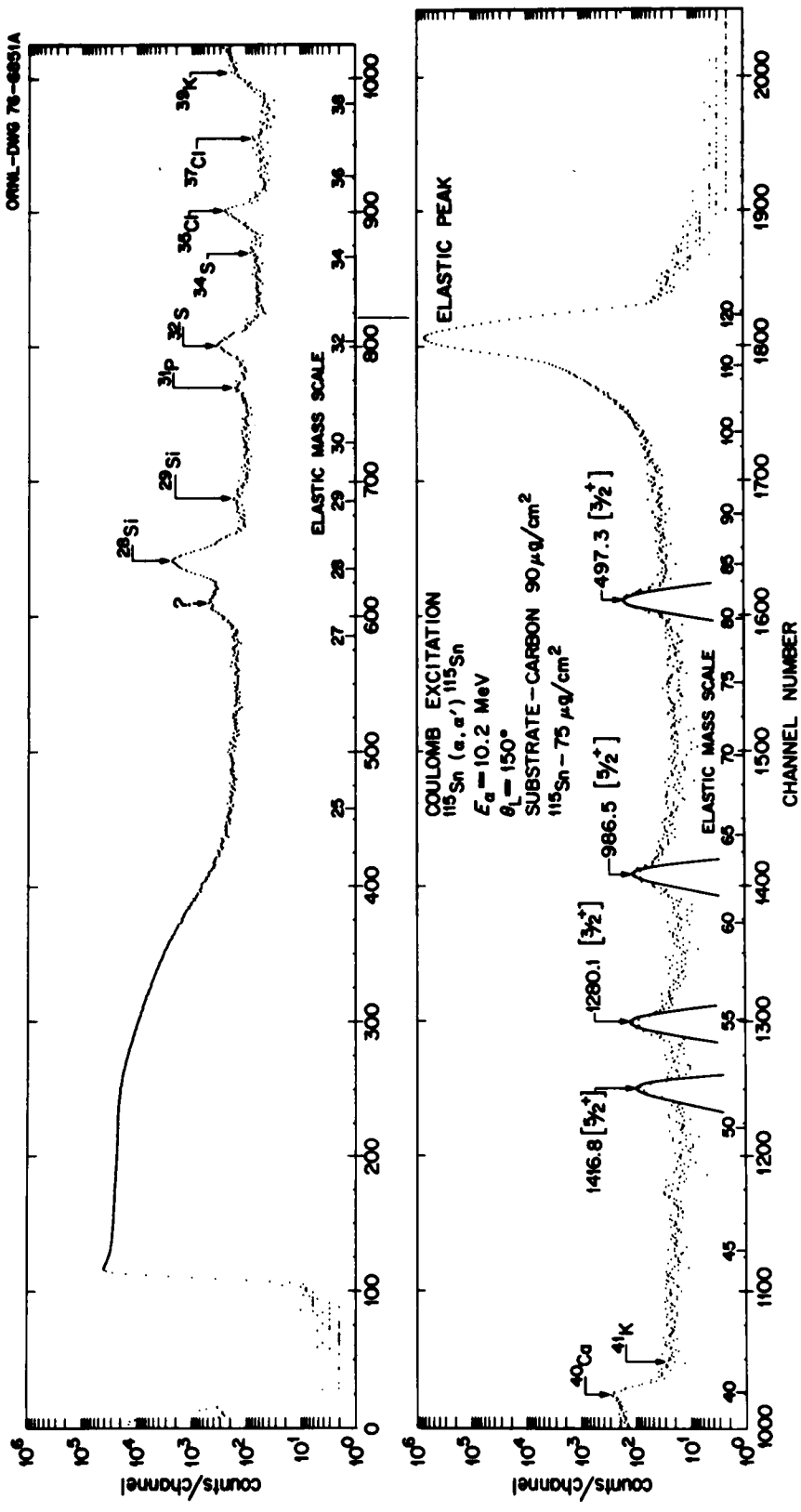


Figure 36. Gated Enge magnet spectrum of $^{115}Sn(\alpha,\alpha')^{115}Sn$ reaction at 10.2 MeV for the 75 μg/cm$^2$ target with the 60 cm position sensitive detector.

with the 60 cm position sensitive proportional detector. Note the elastic mass scale which has been provided in order to identify spectrum contaminants. The lower mass contaminants had no effect on the Sn determinations, but are provided for reference. Of particular significance was the identification of Fe contamination at the 1280.1 keV peak position and Cu contamination at the 986.5 keV position. These contaminants were probably sputtered onto the target surface during the target preparation in the isotope separator and can probably be eliminated on future targets. The light mass contaminants are contained in the carbon substrate.

Figure 37 shows the gated sum pulse from the left and right position sensitive proportional detector pulses for the 10.2 MeV $^{115}Sn(\alpha,\alpha')^{115}Sn$ reaction and shows that essentially all of the main event pulses were getting through and not being gated off. An efficiency calibration run made with the position sensitive proportional detector shows that the detector efficiency was constant to at least ± 1% over the region used by the Sn peaks.

Table XII shows a comparison of the $B_{ex}(E2)$ values extracted from the in beam γ-ray spectra and from the $(\alpha,\alpha')$ spectra. It can be seen that these two independent measurements give identical values for the 497.35 and 1416.78 keV states. The $(\alpha,\alpha')$ data is contaminated for the 986.54 and 1280.08 keV states and is useless for them. A new target could resolve this difficulty. It does show that the in beam γ-ray work has no large systematic errors.

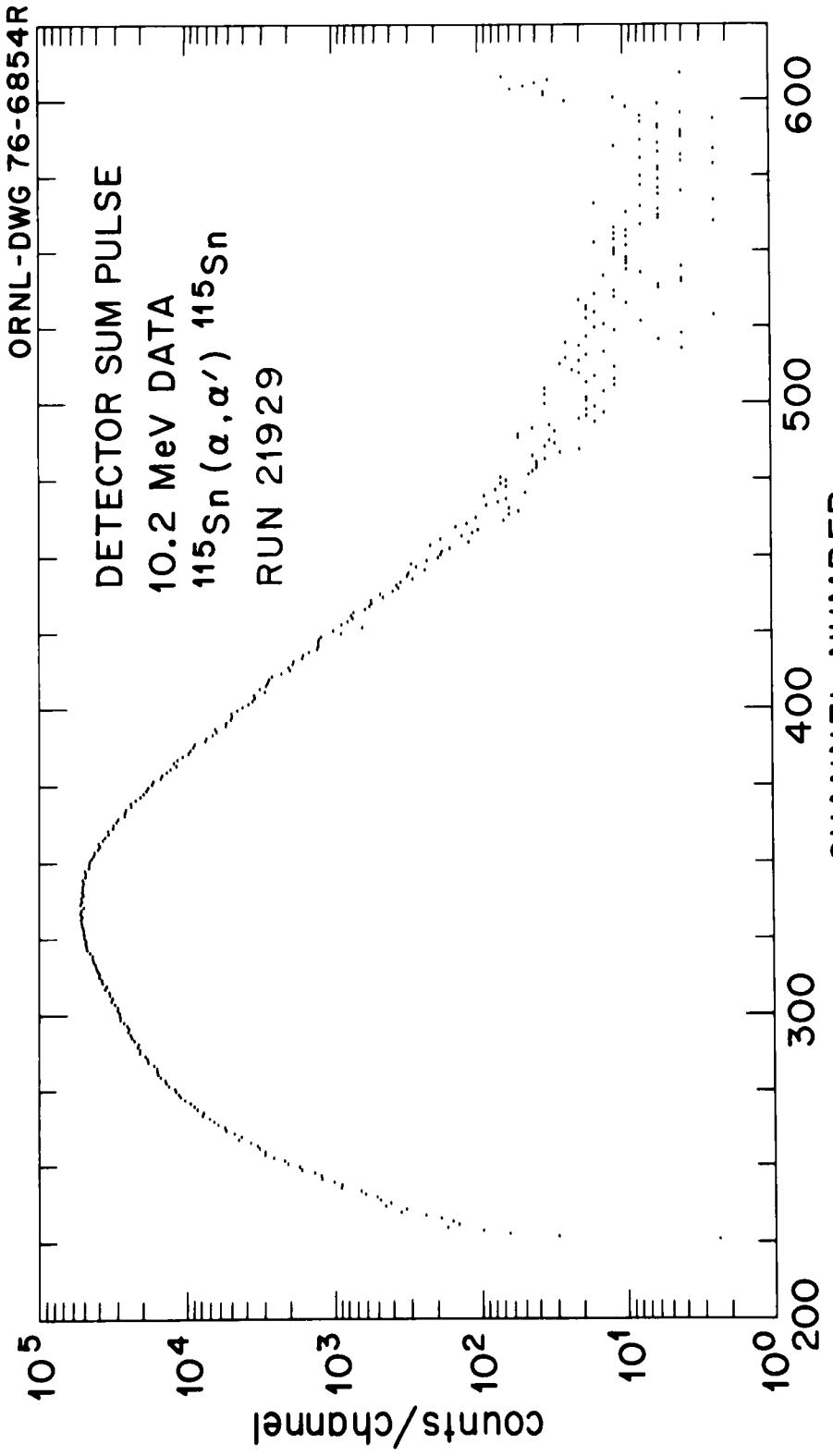


Figure 37. Gated sum pulse from the left and right detector pulses for the 10.2 MeV $^{115}$Sn(α,α')$^{115}$Sn data of Figure 36.

TABLE XII

Comparison of $B_{ex}(E2)$ from Enge magnet $^{115}Sn(\alpha,\alpha')^{115}Sn$ and in-beam $\gamma$-ray measurements

| E (keV) | $J^{\pi}$ | $B_{ex}(E2)$ ($e^2 \cdot fm^4$) | | |
|---|---|---|---|---|
| | | $^{115}Sn(\alpha,\alpha'\gamma)^{115}Sn$ $E_\alpha$ = 10.0 | $^{115}Sn(\alpha,\alpha')^{115}Sn$ $E_\alpha$ = 10.2 MeV | $^{115}Sn(\alpha,\alpha')^{115}Sn$ $E_\alpha$ = 9.5 MeV |
| 497.35 | 3/2+ | 140 ± 8 | 140 ± 4 | 139 ± 11 |
| 986.54 | 5/2+ | 227 ± 10 | (308 ± 11) [a] | (a) |
| 1280.08 | 3/2+ | 444 ± 37 | (662 ± 24) [b] | (b) |
| 1416.78 | 5/2+ | 598 ± 33 | 607 ± 33 | --- |

[a] Inelastic peak contaminated by elastic peak of a Cu contaminant in the target.

[b] Inelastic peak contaminated by elastic peak of a Fe contaminant in the target.

## E. DATA SUMMARY

Table XIII presents a summary of information deduced from the Coulomb excitation of $^{115}Sn$. The basis for the spin parity assignments are discussed in Chapter VI. The mean life $\tau_{calc}$ is calculated from

$$\tau_{calc} = \frac{1}{T} , \tag{V-12}$$

where T is given by

$$T = T_{E2} + T_{M1} . \tag{V-13}$$

The transition probabilities are given by (from Alder et al.[11])

$$T(E2;\ I_f \rightarrow I_i) = 1.23 \times 10^{-2} (\Delta E)^5 B(E2;\ I_i \rightarrow I_f) \times \frac{(2I_i + 1)}{(2I_f + 1)} , \tag{V-14}$$

where $B(E2;\ I_i \rightarrow I_f)$ is the reduced transition probability for excitation previously discussed. The transition probability T(M1) is calculated from

$$\delta^2 = \frac{T(E2)}{T(M1)} . \tag{V-15}$$

TABLE XIII

Summary of information obtained from the Coulomb excitation of $^{115}Sn$

| Level (keV) | $E_\gamma$ (keV) | Branching Ratio (%) | $(I^\pi)_i$ | $(I^\pi)_f$ | $B_d(E2)$ ($e^2fm^4$) | $\frac{B_d(E2)}{B_{sp}(E2)}$ [b] | δ | $B_d(M1)$ $(eħ/2Mc)^2$ | $(\tau_{calc})_{mean}$ (ps) |
|---|---|---|---|---|---|---|---|---|---|
| 497.35 | 497.35 | 100 | $3/2^+$ | $1/2^+$ | 70.0 ± 4.0 | 2.1 | +0.21 ± 0.02 | $(2.72 \pm 0.40)\times10^{-2}$ | 15.6 ± 1.5 |
| | | | | | | | or -3.0 ± 0.3 | $(1.33 \pm 0.20)\times10^{-4}$ | 332 ± 30 |
| 612.79 | 115.44 | 100 | $7/2^+$ | $3/2^+$ | 12.26 ± 0.30 [a] | 0.4 | ∞ | | (3.26 ± 0.08)μs [c] |
| 986.54 | 986.54 | 24.8 ± 0.7 | $5/2^+$ | $1/2^+$ | 75.7 ± 3.3 | 2.3 | ∞ | | 2.81 ± 0.20 |
| | 489.27 | 68.3 ± 0.4 | $5/2^+$ | $3/2^+$ | 11.0 ± 9.0 [f] | 0.33 [f] | 0.040 ± 0.023 | $(1.14 \pm 0.06)\times10^{-1}$ [f] | |
| | | | | | 6490 ± 347 [f] | 195 [f] | or -4.0 ± 0.4 | $(6.7 \pm 0.9)\times10^{-3}$ [f] | |
| | 373.69 | 6.8 ± 0.6 | $5/2^+$ | $7/2^+$ | 87 ± 28 [f] | 2.6 [f] | -0.265 ± 0.062 | $(1.20 \pm 0.11)\times10^{-2}$ [f] | |
| | | | | | 1132 ± 110 [f] | 34 [f] | or -2.40 ± 0.37 | $(1.90 \pm 0.40)\times10^{-3}$ [f] | |
| 1280.08 | 1280.08 | 86.2 ± 1.2 | $3/2^+$ | $1/2^+$ | 222 ± 19 | 6.7 | +0.09 ± 0.01 | (3.1 ± 0.6) | 0.007 ± 0.001 |
| | | | | | | | or -2.2 ± 0.2 [d] | $(5.2 \pm 0.8)\times10^{-3}$ | 0.73 ± 0.07 |
| | 782.99 | 7.8 ± 0.7 | $3/2^+$ | $3/2^+$ | $105^{+120}_{-83}$ | 3.1 | $0.77^{+0.83}_{-0.46}$ | $(7.5^{-4.1}_{+3.4})\times10^{-3}$ | |
| | 668.13 | 3.0 ± 0.7 | $3/2^+$ | $7/2^+$ | 244 ± 57 | 7.4 | ∞ | | |
| | 293.60 | 3.0 ± 0.4 | $3/2^+$ | $5/2^+$ | $1796^{+2859}_{-1236}$ | 54 | $0.38^{+0.25}_{-0.16}$ | $(7.4^{-1.3}_{+0.9})\times10^{-2}$ | |
| | | | | | $13947^{+300}_{-1800}$ | 420 | or > 2.4 | $< 1.1\times10^{-2}$ | |
| 1416.78 | 1416.78 | 72.1 ± 2.8 | $5/2^+$ | $1/2^+$ | 199 ± 11 | 6.0 | ∞ | | 0.53 ± 0.05 |
| | 919.79 | 21.0 ± 1.9 | $5/2^+$ | $3/2^+$ | 14.1 ± 3.8 | 0.4 | 0.17 ± 0.03 | $(2.9 \pm 0.3)\times10^{-2}$ | |
| | | | | | 496 ± 56 | 15 | or -8.2 ± 2.3 | $(4.3 \pm 1.8)\times10^{-4}$ | |
| | 804.04 | 5.1 ± 0.7 [e] | $5/2^+$ | $7/2^+$ | | | | | |
| | 430.27 | 0.6 ± 0.4 | $5/2^+$ | $5/2^+$ | $145^{+374}_{-145}$ | 4.4 | $0.55^{+1.65}_{-0.55}$ | $(6.2^{-4.8}_{+1.8})\times10^{-3}$ | |
| | 136.70 | 1.2 ± 0.5 | $5/2^+$ | $3/2^+$ | 8773 ± 11099 | 264 | 0.17 ± 0.15 | $(3.9 \pm 1.4)\times10^{-1}$ | |
| | | | | | $308,000^{-16,300}_{+5000}$ | 9,300 | or < -3.7 | $< 28 \times 10^{-3}$ | |

[a] Calculated from τ measured, see note (c).

[b] $B_{sp}(E2) = \frac{e^2}{4\pi}\left(\frac{3}{5}\right)^2 (1.2\text{ fm})^4 A^{4/3} = 33.2\ e^2fm^4$ for A = 115.

[c] τ measured value E. A. Ivanov, A. Iordachescu, G. Pascovici, Rev. Roumaine Phys. 13,879 (1968).

[d] Value selected as being in agreement with Doppler shift measurement of τ.

[e] Present $E_\gamma$ = 804 KeV line contaminated. Used branching ratio from work of Schwengler.[9]

[f] Used branching ratios of 3.7 ± 0.3%, 70.1 ± 5.4%, and 26.3 ± 1.74% from work of Schwengler[9] and Maduemo et al.[10] (see text).

The reduced transition probability for decay in terms of the excitation reduced probability is given by

$$B_d(E2;\ I_f \rightarrow I_i) = \frac{2I_i + 1}{2I_f + 1} B_{ex}(E2;\ I_i \rightarrow I_f). \qquad \text{(V-16)}$$

To calculate the properties of intermediate transitions we use the relationship

$$\text{Branching Ratio} = \frac{(1+\alpha^{T_i})[T(E2;I_f \rightarrow I_i)+T(M1;I_f \rightarrow I_i)]}{(1+\alpha^{T_f'})[T(E2;I_f \rightarrow I_f')+T(M1;I_f \rightarrow I_f')]}, \qquad \text{(V-17)}$$

where $I_f \rightarrow I_i$ is the ground state transition.

In practice one first calculates $B_d(E2)$, $B_d(M1)$ and $\tau_{calc}$ for the ground state transitions using measured data for $B_{ex}(E2)$, and Equations (V-16) and (V-14) to get T(M1) from Equation (V-15). The reduced transition probabilities for decay are related to the total transition probabilities for decay by

$$T(E2) = 1.22 \times 10^{9}(\Delta E)^{5}B_d(E2)$$

$$T(M1) = 1.76 \times 10^{13}(\Delta E)^{3}B_d(M1). \qquad \text{(V-18)}$$

Equations (V-17) and (V-15) are then used to calculate the T(E2) and T(M1) for the intermediate transitions. Equation (V-18) is then used to calculate $B_d(M1)$ and $B_d(E2)$. $B_{sp}$ is the reduced transition probability for a single particle transition.

Figure 38 is a level diagram showing the levels in $^{115}$Sn which are observed from Coulomb excitation. Also shown are the values $B_d(E2)/B_{sp}(E2)$. Figure 39 is a level diagram showing the levels in $^{115}$Sn which are observed from Coulomb excitation. Also shown are the values of $B_d(M1)$ taken from Table XIII in units of $(e\hbar/2mc)$.[2]

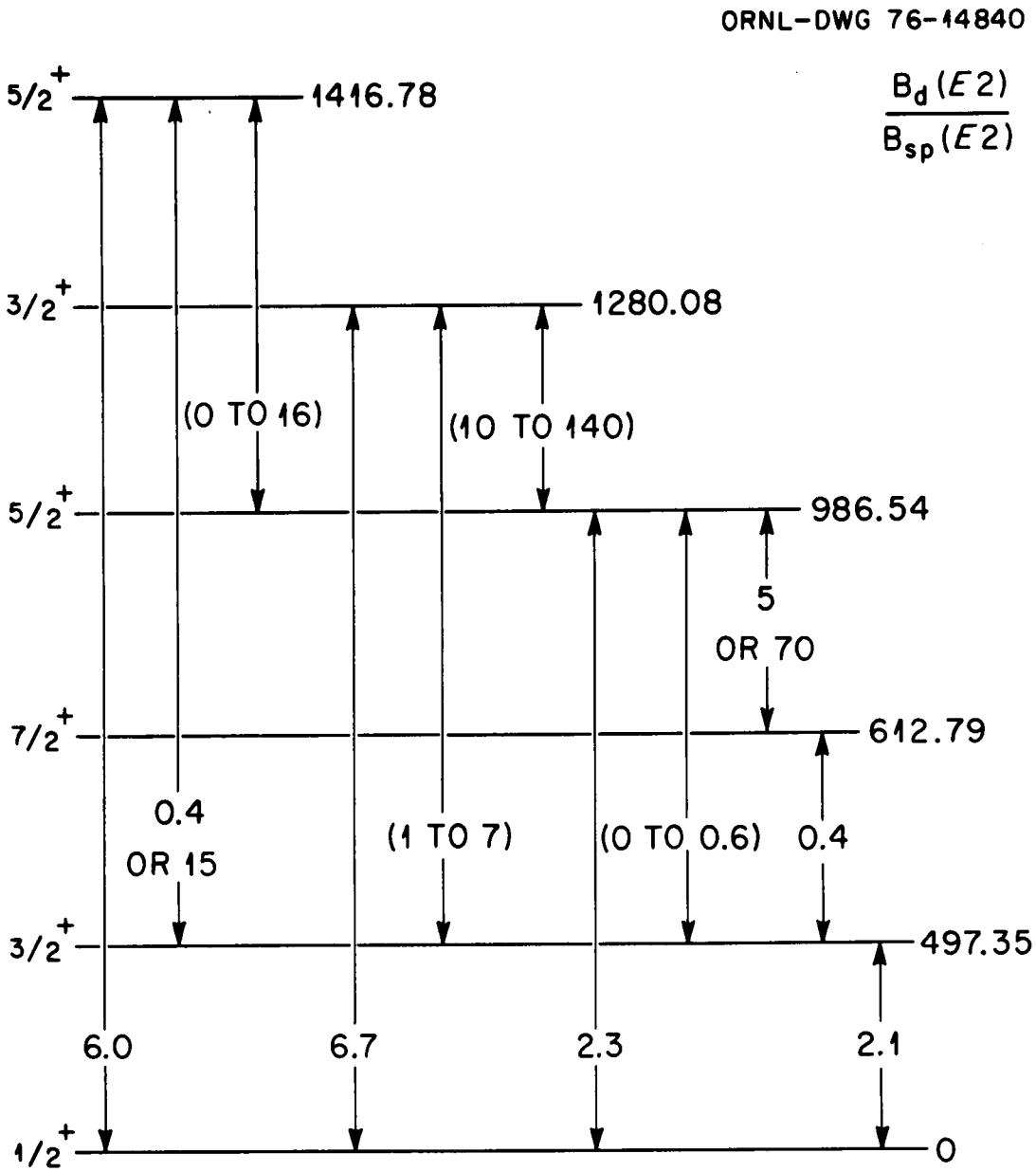


Figure 38. Level diagram showing the levels in $^{115}Sn$ which are observed from Coulomb excitation. Also shown are the values of $B_d(E2)/B_{sp}(E2)$.

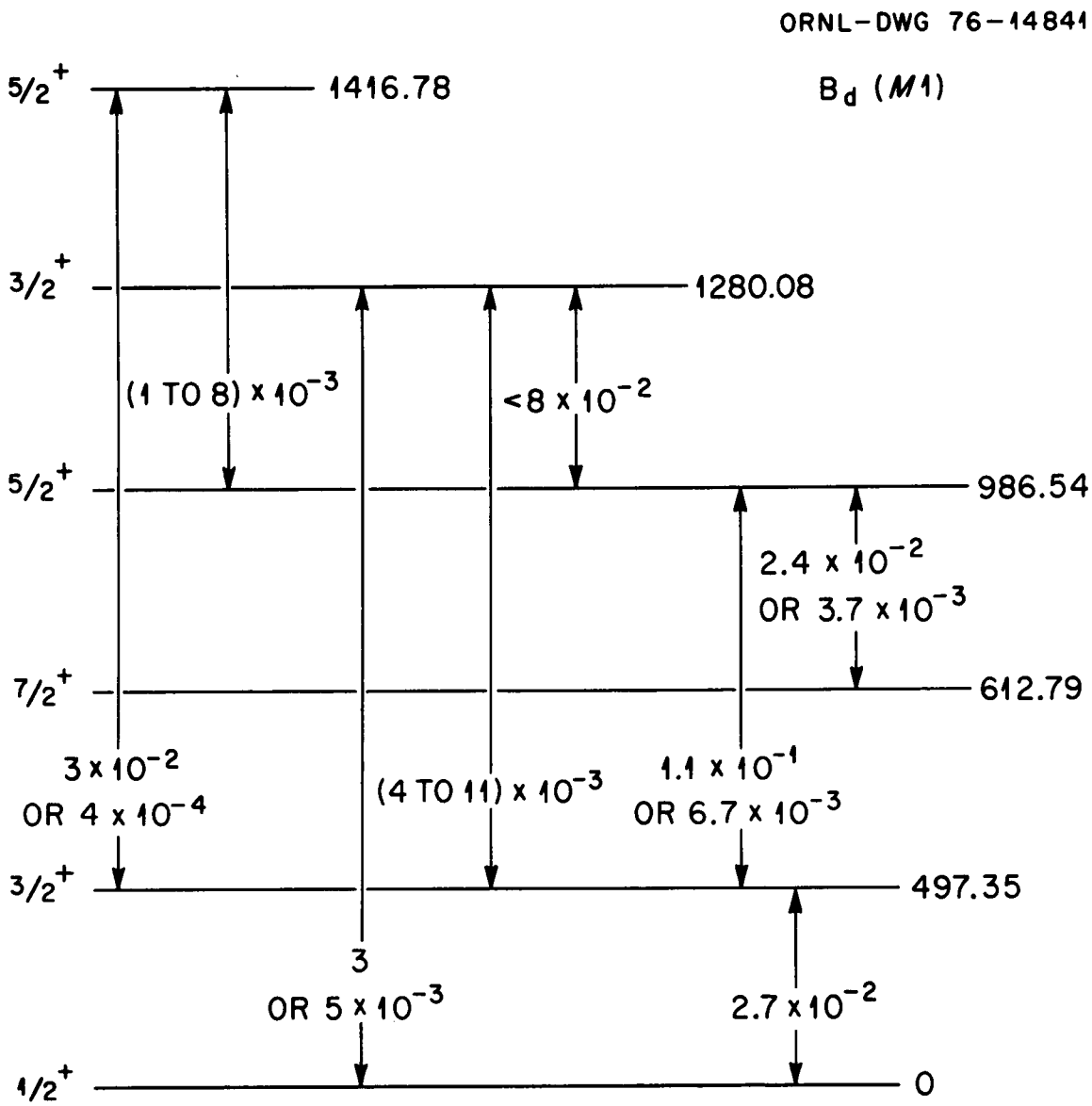


Figure 39. Level diagram showing the levels in $^{115}$Sn which are observed from Coulomb excitation. Also shown are the values of $B_d$(M1) taken from Table XIII in units of $(e\hbar/2mc)^2$.

# CHAPTER VI

## DISCUSSION AND CONCLUSIONS

The experimental results in the preceding sections have been used for the construction of the level scheme in Figure 22 (page 91). The ground state of $^{115}$Sn is known to be $1/2^+$.[55,58] Good agreement between precise $\gamma$-ray energies, angular distributions, coincidence relations, and excitation functions has led to the establishment of levels at g.s($1/2^+$), 497.35($3/2^+$), 612.79($7/2^+$), 713.21($11/2^-$), 986.54($5/2^+$), 1280.08($3/2^+$), and 1416.78($5/2^+$) keV. These assignments are in close agreement with the results of previous investigations as shown in Table XIV.

### A. DISCUSSION OF INDIVIDUAL LEVELS OF $^{115}$Sn

#### The 497.35 keV Level

The 497.35 keV level has been identified previously through the work of Madueme et al.,[10] Schwengler,[9] Cavanagh et al.,[7] Fleming et al.,[6] and Schneid et al.[5] The energies determined in this study agree with those of Madueme et al. and Schwengler within experimental error. Angular distribution measurements of the 497.35 keV $\gamma$-ray at $E_\alpha$ = 7.0 MeV are not consistent with a $5/2^+$ assignment. Since the 497.35 keV level is directly excited by the E2 Coulomb excitation process from the $1/2^+$ ground state and has an excitation function in agreement with a 497.35 keV assignment, it has been assigned a spin parity of $3/2^+$. The 986.54($5/2^+$) state decays by a 489.27 keV $\gamma$-ray via the 497.35($3/2^+$) level 68.4% of the time and the 489.27 keV $\gamma$-ray is in strong coincidence with

TABLE XIV

Comparison of published data on $^{115}$Sn energy levels, transitions, and spin assignments with the present study

| Level (keV) | $E_\gamma$ $^{115}$Sn(α,αγ)$^{115}$Sn this work (1976) | $J^\pi$ | Madueme et al.[10] $^{115}$In(p,n)$^{115}$Sn $^{112}$Cd(α,n)$^{115}$Sn $^{115}$In(d,2n)$^{115}$Sn $^{113}$Cd(α,2n)$^{115}$Sn (1975) | $J^\pi$ | Schwengler[9] $^{115}$In(p,nγ)$^{115}$Sn (1973) | $J^\pi$ | Nuclear Data Sheet[55] (1975) | $J^\pi$ | Cavanagh et al.[7] $^{116}$Sn(p,d)$^{115}$Sn (1970) | $J^\pi$ | Fleming et al.[6] $^{117}$Sn(p,t)$^{115}$Sn (1971) | $J^\pi$ | Schneid et al.[5] $^{114}$Sn(d,p)$^{115}$Sn $^{116}$Sn(d,t)$^{115}$Sn (1967) | $J^\pi$ |
|---|---|---|---|---|---|---|---|---|---|---|---|---|---|---|
| 1416.78 | 1416.78±0.10 | $\frac{5+}{2}$ | 1416.8±0.3 | $\frac{5+}{2}$ | 1416.89±0.08 | $\frac{5+}{2}$ | 1425±15 | $\frac{3+}{2},\frac{5+}{2}$ | 1419 | $\frac{5}{2}$ | 1430±15 | $(\frac{5+}{2})$ | | |
| | 919.79±0.17 | | 919.5±0.2 | | 919.43 | | | | | | | | | |
| | 804.04±0.25 | | 803.2±0.2 | | 804.29 | | | | | | | | | |
| | 430.27±0.30 | | | | | | | | | | | | | |
| | 136.70±0.15 | | | | | | | | | | | | | |
| 1280.08 | 1280.08±0.22 | $\frac{3+}{2}$ | 1280.0±0.2 | $\frac{3+}{2}$ | 1279.99±0.06 | $\frac{3+}{2}$ | 1279±3 | $\frac{3+}{2},\frac{5+}{2}$ | 1282 | $\frac{3}{2}$ | 1280±20 | $(\frac{3+}{2},\frac{5+}{2})$ | 1280 | $(\frac{5+}{2})$ |
| | 782.99±0.09 | | | | 782.73 | | | | | | | | | |
| | 668.13±0.34 | | | | | | | | | | | | | |
| | 293.60±0.29 | | | | | | | | | | | | | |
| 986.54 | 986.54±0.08 | $\frac{5+}{2}$ | 986.5±0.2 | $\frac{5+}{2}$ | 986.49±0.03 | $\frac{5+}{2}$ | 990±3 | $\frac{3+}{2},\frac{5+}{2}$ | 998 | $\frac{5}{2}$ | 990±10 | $\frac{5+}{2}$ | 980 | $\frac{5+}{2}$ |
| | 489.27±0.05 | | 489.3±0.3 | | 489.19 | | | | | | | | | |
| | 373.69±0.52 | | 373.6±0.4 | | | | | | | | | | | |
| 713.21 | | | | | 713.21±0.20 | $\frac{11-}{2}$ | 714.6±3.0 | $(\frac{11}{2})^-$ | 729 | $\frac{11}{2}$ | 730±20 | $\frac{11-}{2}$ | 730 | $\frac{11-}{2}$ |
| 612.79 | 612.79±0.06 | $\frac{7+}{2}$ | | | 612.64±0.06 | $\frac{7+}{2}$ | 613.9±2.5 | $(\frac{7}{2})^+$ | 623 | $\frac{7}{2}$ | 620±20 | $\frac{7+}{2}$ | 600 | $\frac{7+}{2}$ |
| | 115.44±0.04 | | 115.4±0.2 | | 115.34 | | | | | | | | | |
| 497.35 | 497.35±0.05 | $\frac{3+}{2}$ | 497.3±0.2 | $\frac{3+}{2}$ | 497.30±0.02 | $\frac{3+}{2}$ | 498.0±1.0 | $(\frac{3}{2})^+$ | 501 | $\frac{3}{2}$ | 495±15 | $\frac{3+}{2}$ | 490 | $\frac{3+}{2}$ |
| g.s. | g.s. | $\frac{1+}{2}$ | g.s. | $\frac{1+}{2}$ | g.s. | $\frac{1+}{2}$ | g.s. | $\frac{1+}{2}$ | g.s. | $\frac{1}{2}$ | g.s. | $\frac{1+}{2}$ | g.s. | $\frac{1+}{2}$ |

the 497.35 keV γ-ray thus supporting the existence of the 497.35 keV level. The work of Madueme et al. lists the 497.35 keV γ-ray as pure M1 thus leading to the selection of the present value of $\delta = +0.21 \pm 0.02$ rather than $-3.0 \pm 0.3$ from Table XIII (page 124). This also gives prefered values of $\tau = 15.6 \pm 1.5$ ps and $B_d(M1) = (2.72 \pm 0.40) \times 10^{-2}(e\hbar/2mc)^2$.

The 612.79 keV Level

The 612.79 keV level is not directly excited by the E2 Coulomb excitation process and no 612.79 keV radiation is observed thus indicating a $J^{\pi}$ assignment greater than 5/2+. However, a strong 115.44 keV γ-ray in coincidence with the 497.35 keV γ-ray is observed thus supporting the existence of a 612.79 keV level. The 612.79 keV level has been identified as an isomeric level with $T_{1/2} = 3.26 \pm 0.08$ μs by the work of Ivanov et al.[59] According to the level scheme of Figure 22 (page 91) the intensities of the 804.04 keV, 668.13 keV, and 373.69 keV γ-rays feeding the 612.79 keV level should equal the intensity of the 115.44 keV γ-ray depopulating this state. Unfortunately contaminant γ-rays on the feeding transitions prevented such a good balance check. The 804.04 keV transition was strongly contaminated by an $^{55}$Fe γ-ray originating from the $^{52}$Cr(α,n)$^{55}$Fe reaction. This γ-ray was measured in the two parameter coincidence spectrum along with the other $^{55}$Fe γ-rays to give a definite identification. The 373.69 keV and 668.13 keV transitions were also members of close lying γ-ray multiplets leading to the possibility of error in their stripped intensities.

The reaction work of Schwengler,[9] Cavanagh et al.,[7] Fleming et al.,[6] and Schneid et al.[5] have also identified this level as being $7/2^+$ and at 600 to 623 keV. Madueme et al. have also identified the 115.44 keV transition as originating from the 612.79 keV level and consisting of pure E2 radiation to the 497.35 keV level. The Nuclear Data Sheets have identified this level as 613.9 ± 2.5 keV with a possible $7/2^+$ assignment.

The 713.21 keV Level

The 713.21 keV level was not studied in this research, but has been included for completeness. Ivanov et al.[60-62] have studied this isomeric level and have reported a half life of $T_{1/2}$ = 159 ± 1 μs at 726 keV. Nuclear Data Sheets lists this level as having a possible 11/2 assignment with negative parity. Schwengler[9] lists this level as 713.21 keV with an $11/2^-$ assignment.

The 986.54 keV Level

The angular distribution of the 986.54 keV γ-ray is consistent with a $5/2^+$ spin assignment to the 986.54 keV state. The work of Madueme et al.[10] and Schwengler[9] agrees with this assignment to within experimental error. This level has been identified by Cavanagh et al.[7] as 998(5/2) keV, by Fleming et al.[6] as 990($5/2^+$) keV, and by Schneid et al.[5] as 980($5/2^+$) keV. The strong coincidence of the 489.27 keV and 497.35 keV γ-rays supports the existence of this level. The excitation function supports the 986.54 keV γ-ray as a ground state transition from the 986.54 keV level.

The 1280.08 keV Level

The existence of a strong 1280.08 keV γ-ray and a 782.99 keV γ-ray in coincidence with the 497.35 keV γ-ray supports the assignment of the 1280.08 keV γ-ray to a 1280.08 keV level. The excitation function of the 1280.08 keV γ-ray supports this assignment.

The angular distribution of the 1280.08 keV γ-ray does not support a $5/2^+$ assignment and has thus led to the spin parity assignment of $3/2^+$. This agrees with the spin parity assignments of Madueme et al.,[10] Schwengler,[9] and Schneid et al.[5] Cavanagh et al.[7] have listed this level as 1282 (3/2) and Fleming et al.[6] as 1280($3/2^+$, $5/2^+$).

The 1416.78 keV Level

The angular distribution of this level was done both with the 28.52% and 92.31% $^{115}$Sn target spectra and supports a $5/2^+$ spin parity assignment. The excitation function of the 1416.78 keV γ-ray supports the assignment of it to a 1416.78 keV level. The energy sum and strong coincidence of 919.79 keV and 497.35 keV γ-rays also supports the existence of the 1416.78 keV level.

Madueme et al.[10] and Schwengler[9] have made this same assignment within experimental error. Cavanagh et al.[7] has a level at 1419(5/2) keV and Fleming et al.[6] at 1430 with a possible $5/2^+$ assignment.

## B. COMPARISON OF THE ENGE AND GAMMA-RAY RESULTS

The Enge magnet (α,α') results and in beam γ-ray results listed in Table XII (page 122) show that there is excellent agreement between

these measurements. The $B_{ex}(E2)$ measured by the two independent methods agree within experimental error for the 497.35 and 1416.78 keV states. Discrepancies in the 986.54 and 1280.08 keV state data are accounted for by contaminants identified in the $(\alpha,\alpha')$ spectrum. A target has been prepared in which an attempt was made to eliminate these contaminants, but unfortunately was prepared too late to be run and included in this research.

## C. SUMMARY

Table XIV lists a comparison of published data on $^{115}$Sn energy levels, transitions and spin assignments with the present study. The results of this research agree most closely with the recent results of Schwengler[9] and Madueme et al.[10]

This study presents the first known Coulomb excitation results on $^{115}$Sn and on the $B_{ex}(E2)$, $B_d(E2)$, and $B_d(M1)$ values for this nucleus. An extensive search of the coincidence and singles data failed to show up any new energy levels. This study also has the first measurements of $^{115}$Sn state lifetimes other than the isomeric levels at 612.79 and 713.21 keV previously reviewed.

Figure 40 shows a level diagram for Sn, displaying excitation strengths to the various states of the stable odd $^{115,117,119}$Sn nuclei. Widths of the arrows are proportional to $B_{ex}(E2)$ values. The number associated with each arrow is $B_{ex}(E2)$ in units of $e^2fm^4$. The $^{117,119}$Sn results are from the work of Stelson et al.[4]

Figure 41 shows the systematics of the levels in several of the odd Sn nuclei in the energy region below 2 MeV.[63] Also shown are the

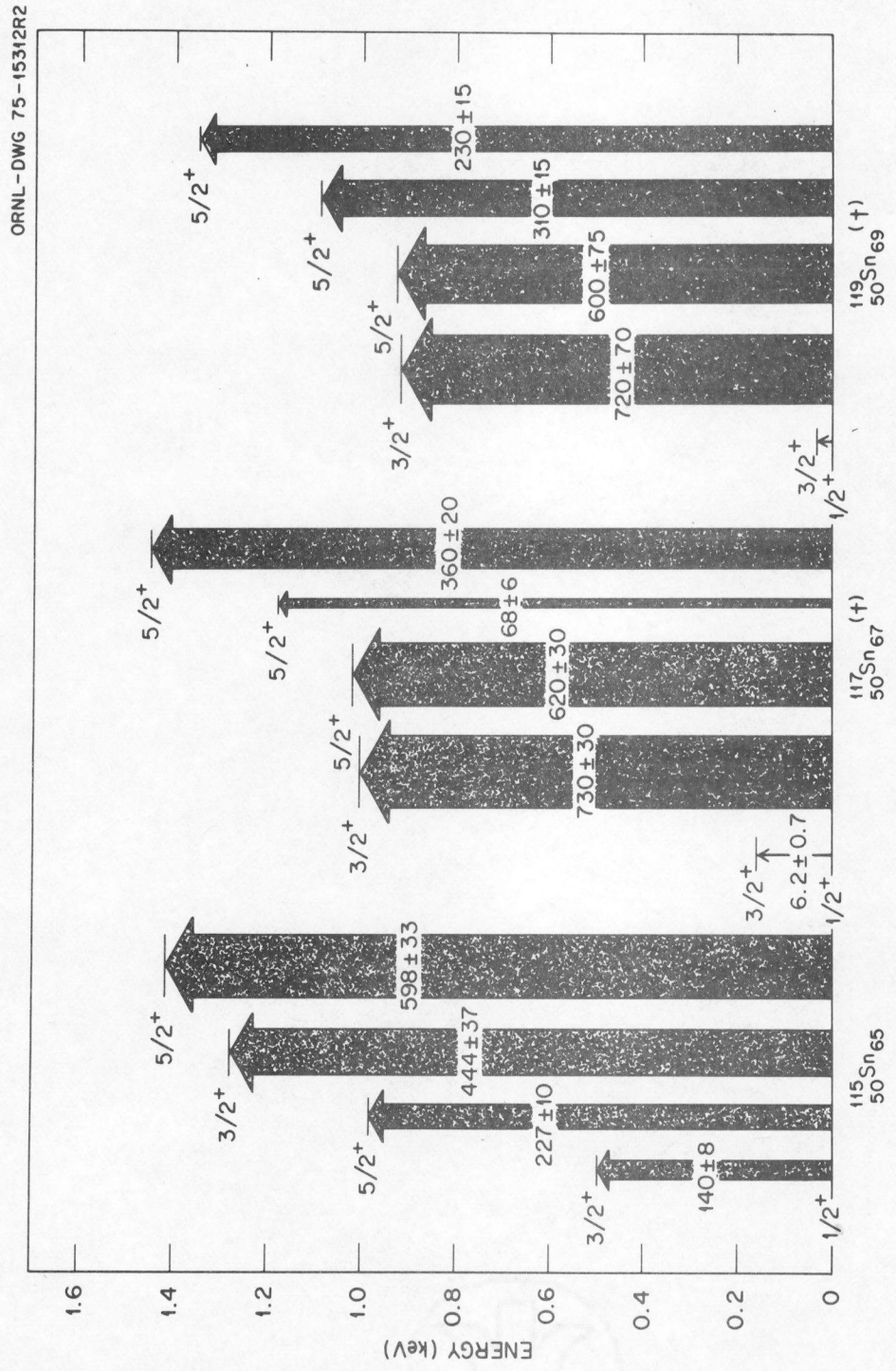


Figure 40. Level diagram for tin, displaying excitation strengths to the various states of $^{115,117,119}$Sn. Widths of arrows are proportional to $B_{ex}$(E2). The number associated with each arrow is $B_{ex}$(E2) in units of $e^2$ $fm^4$.

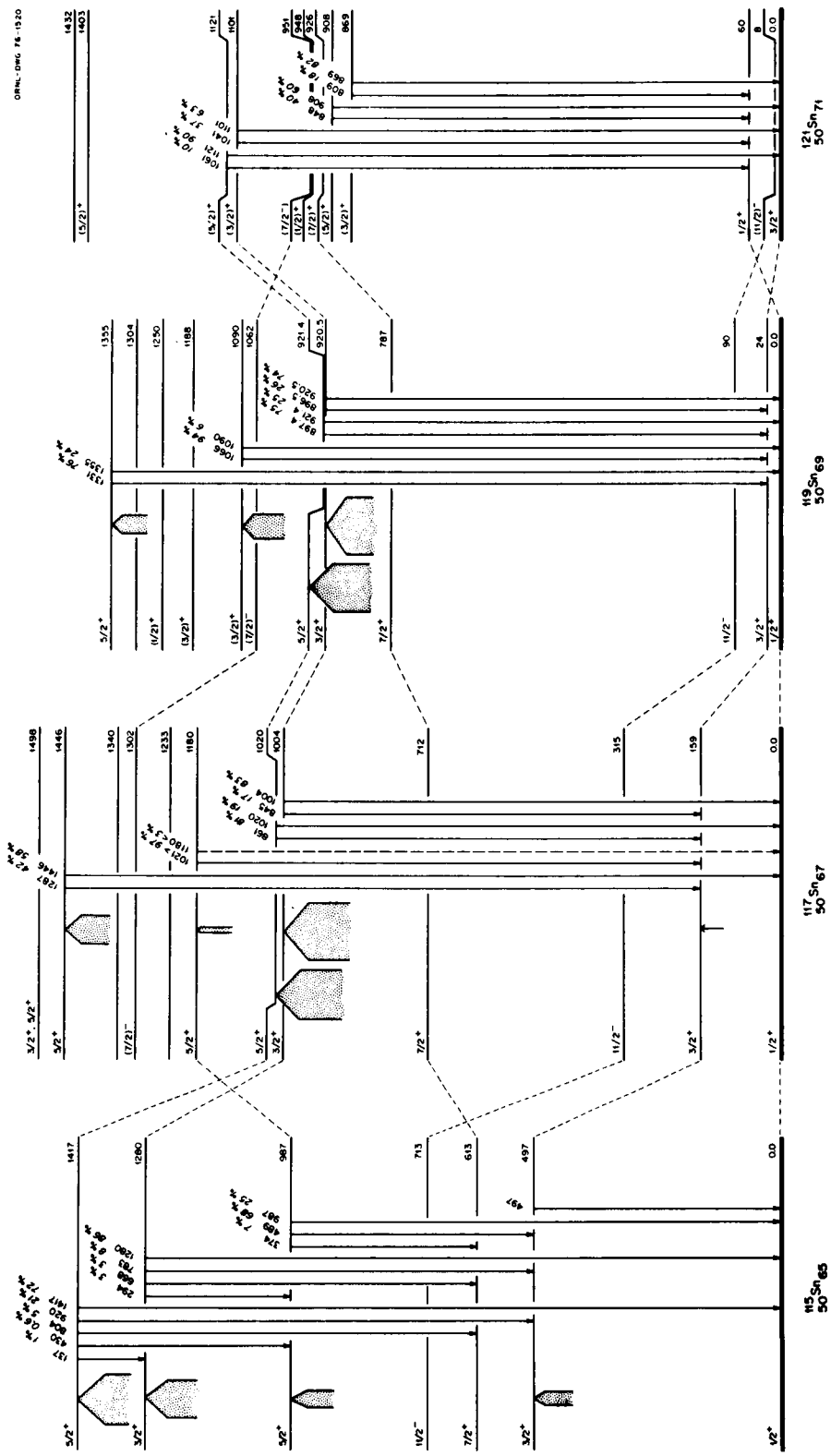


Figure 41. Systematics of the levels in the odd tin nuclei in the energy region below 2 MeV.

branching ratios and arrows whose widths are proportional to the $B_{ex}(E2)$ values of each level excited.

The states of the tin isotopes can be described as having a closed proton shell at Z = 50 and as belonging to a configuration with 13 to 25 neutrons distributed among the following five single-particle levels; $2d_{5/2}$, $1g_{7/2}$, $3s_{1/2}$, $2d_{3/2}$, and $1h_{11/2}$. The isotope $^{115}$Sn would have 15 neutrons distributed in this manner. Kuo et al.[3] have performed theoretical calculations on the odd-mass tin isotopes using a shell model with a residual interaction involving several unknown parameters; i.e., the range, the depth and exchange mixture. Calculations were limited to a central residual interaction and to a model with single-particle energies not depending on atomic mass and considered as parameters.

The BCS theory used in these calculations describes the low level Sn states as neutron one quasi-particle (1QP) states. Above 1 MeV the weak coupling model is useful in studying the energy structure. According to this model the levels in the odd tin isotopes will be grouped into multiplets whose wave functions consist of one of the eigenfunctions of the neighboring even tin isotopes, usually referred to as a "phonon" coupled to a quasi-particle.

Kuo et al.[3] have calculated several values for the 497.35 keV $3/2^+ \rightarrow 1/2^+$ ground state transition which are compared to experiment in Table XV.

Table XVI presents some experimental data for tin nuclei from Nuclear Data Sheets[55] on the cross-sections for particle transfer reactions. Using this data the lowest 497.35 ($3/2^+$) and 986.54

TABLE XV

A comparison of experimental with theoretically calculated values for $B_d(M1)$, $B_d(E2)$, and $T(E2)/T(M1)$ for the 497.35 keV transition

| | Kuo et al.[3] calculation | This study experimental |
|---|---|---|
| $B_d(M1)\left(\frac{e\hbar}{2mc}\right)^2$ | 0.014 | $0.027 \pm 0.004$ |
| $B_d(E2)\,(e^2fm^4)$ | 44 | $70 \pm 4$ |
| $\frac{T(E2)}{T(M1)}$ | $5.4 \times 10^{-2}$ | $(4.4 \pm 1.9) \times 10^{-2}$ |

TABLE XVI

A comparison of some experimental data from Nuclear Data Sheets[52] on relative cross-sections for particle transfer reactions

| Reaction E(level) (keV) | $J^{\pi}$ | (d,p) $(2J + 1)C^2S$ | (p,d) $\sigma(\theta)$max (mb/sr) | (p,t) rel.$\sigma$ |
|---|---|---|---|---|
| 0 | 1/2+ | 1.92 | 14.0 | 21.6 |
| 497.35 | 3/2+ | 2.48 | 3.22 | 2.2 |
| 986.54 | 5/2+ | 0.72 | 15.3 | 4.2 |
| 1280.08 | 3/2+ | 0.17 | 0.27 | 0.50 |
| 1416.78 | 5/2+ | not seen | 0.36 | 2.1 |

($5/2^+$) keV levels are interpreted as shell model states while the higher 1280.08($3/2^+$) and 1416.78($5/2^+$) keV levels are interpreted as collective states resulting from a coupling of the even tin core 2+ state with the $s_{1/2}$ odd particle.

Table XII (page 122) presents the reduced transition probability for excitation, $B_{ex}(E2)$, for the four low lying $^{115}Sn$ levels which were Coulomb excited. In contrast to the interpretation of Table XVI this data shows that considerable collective strength exists in all four levels. From the work of Stelson et al.[4] it can be seen that the high collectivity of the low lying $3/2^+$ state in $^{115}Sn$ is in sharp contrast to the case for $^{117}Sn$ where the lowest lying $3/2^+$ state at 158.7 keV has a $B_{ex}(E2)$ of only 6.2 $e^2fm^4$.

If one examines the systematics of the $B_{ex}(E2)$ values for $^{115,117,119}Sn$ it is found that the center-of-gravity, CG, of the low lying multiplets have a similar relationship for each of these odd nuclei when compared to the adjacent even-even tin nucleus 2+ state as shown in Table XVII. The center-of-gravity CG is defined as

$$CG = \frac{\sum_i E_i \times B_{ex}(E2)_i}{\sum_i B_{ex}(E2)_i} , \qquad \text{(VI-1)}$$

where $E_i$ is the energy level of the low direct Coulomb excited states in keV, CG is the center-of-gravity in keV, and $B_{ex}(E2)_i$ is the reduced transition probability for excitation of each low lying level $E_i$ in the odd tin nucleus .

TABLE XVII

Systematics of the even-even and odd tin B(E2) center of gravities

| Odd Nucleus | CG (keV) | Even-even Nucleus | 2+ State (keV) | CG/2+ | ΣB(E2) ($e^2fm^4$) | B(E2) 2+ ($e^2fm^4$) | Ratio |
|---|---|---|---|---|---|---|---|
| 115 | 1213 | 116 | 1293 | 0.94 | 1410 | 2160 | 0.65 |
| 117 | 1103 | 118 | 1230 | 0.90 | 1780 | 2160 | 0.82 |
| 119 | 1003 | 120 | 1171 | 0.86 | 1860 | 2030 | 0.92 |

Thus the $B_{ex}(E2)$ strength measured in the $^{115}Sn$ nucleus compares quite well with the values measured for $^{117}Sn$ and $^{119}Sn$ nuclei.

## D. CONCLUDING REMARKS

Isotopically enriched targets of $^{115}Sn$ have been Coulomb excited to provide a verification of a recently established low energy level scheme. This study has failed to uncover any new low energy levels by coincidence and singles $\gamma$-ray measurements. The first values for the reduced transition probabilities for excitation and decay, $B_{ex}(E2)$, $B_d(E2)$, $B_d(M1)$ have been measured. Definite values for spin parity assignments have been made. The first lifetime measurements for the 1416.78, 1280.08, and 986.54 keV states have been made by Doppler shift measurements. Excellent agreement was found between in beam $\gamma$-ray measurement of $B_{ex}(E2)$ values and those measured independently by the $^{115}Sn(\alpha,\alpha')^{115}Sn$ reaction. Future measurements could benefit greatly from cleaner targets. This study has demonstrated that significant reductions in low Z chemical contaminants can be had if targets are prepared by direct beam deposition in an isotope separator rather than by electroplating. Further work on this technique could probably provide still further reductions.

# LIST OF REFERENCES

# LIST OF REFERENCES


1. D. G. Alkhazov, A. P. Grinberg, G. M. Gusinskii, K. I. Erokhina, and I. Kh. Lemburg, JETP (Sov. Phys.) 10, 1086 (1960).

2. P. H. Stelson, W. T. Milner, F. K. McGowan, and R. L. Robinson, Bull. Am. Phys. Soc. 12, 19 (1967).

3. T. T. S. Kuo, E. U. Baranger, and Michel Baranger, Nucl. Phys. 79, 513-549 (1966).

4. P. H. Stelson, W. T. Milner, F. K. McGowan, R. L. Robinson, and S. Raman, Nucl. Phys. A190, 197-217 (1972).

5. E. J. Schneid, A. Prakash, and B. L. Cohen, Phys. Rev. 156, 1316-1331 (1967).

6. D. G. Fleming, M. Blann, and H. W. Fulbright, Nucl. Phys. A163, 401-417 (1971).

7. P. E. Cavanagh, C. F. Coleman, A. G. Hardacre, G. A. Gard, and J. F. Turner, Nucl. Phys. A141, 97-122 (1970).

8. S. Raman and H. J. Kim, Nuclear Data Sheets 16, No. 2, 195-230 (1975).

9. M. Schwengler, Doctoral Dissertation, Johann-Wolfgang-Goethe-Universitat zu Frankfurt am Main, 1973 (unpublished).

10. G. Ch. Madueme, L. Westerberg, L. O. Edvardson, and M. Migahed, Physical Scripta 12, 189-198 (1975).

11. K. Alder, A. Bohr, T. Huus, B. Mottelson, and A. Winter, Rev. Mod. Phys. 28, 432-542 (1956).

12. E. Rutherford, J. Chadwick, and C. D. Ellis, Radiations from Radioactive Substances (Cambridge University Press, Cambridge, England, 1930) p. 247 ff; L. Londau, Physik Z. Sowjetunion 1, 88 (1932); V. F. Weisskopf, Phys. Rev. 53, 1018 (1938).

13. S. W. Barnes and P. W. Aradine, Phys. Rev. 55, 50 (1939); J. R. Risser, K. Lark-Horovitz, and R. N. Smith, Phys. Rev. 57, 355 (1940).

14. R. B. Day and T. Huus, Phys. Rev. 85, 761 (1952); C. L. McClelland, M. S. Thesis, Massachusetts Institute of Technology, August, 1952.

15. C. L. McClelland and C. Goodman, Phys. Rev. 91, 760 (1953).

16. T. Huus and C. Zupancic, Kgl. Danske Videnskab. Selskab. Mat. fys. Medd. 28, No. 1 (1953).

17. K. Alder and A. Winther, Phys. Rev. 96, 237 (1954).

18. F. K. McGowan and P. H. Stelson, Phys. Rev. 99, 127 (1955).

19. L. C. Biedenharn, J. L. McHale, and R. M. Thaler, Phys. Rev. 100 **376** (1955); K. Alder and A. Winther, Kgl. Danske Videnskab. Selskab. Mat. fys. Medd. 29, No. 19 (1955); K. Alder and A. Winther, Phys. Rev. 91, 1578 (1953); **L.** C. Biedenharn, M. Goldstein, J. L. McHale, and R. M. Thaler, Phys. Rev. 101, 662 (1956) and 102, 1567 (1956).

20. N. Bohr, Kgl. Danske Videnskab. Selskab. Mat. fys. Medd. 18, No. 8 (1948).

21. K. Alder and A. Winther, Kgl. Danske Videnskab. Selskab. Mat. fys. Medd. 32, No. 8 (1960).

22. P. A. M. Dirac, The Principles of Quantum Mechanics (Oxford University Press, New York, 1947) third edition, p. 172.

23. K. Alder and A. Winther, Kgl. Danske Videnskab. Selskab. Mat. fys. Medd. 31, No. 1 (1956).

24. K. Alder and A. Winther, Cern Report T/KA-AW-1 (1954).

25. K. Alder and A. Winther, Cern Report T/KA-AW-4 (1955).

26. F. D. Benedict, P. B. Daitch, and G. Breit, Phys. Rev. 101, 171 (1956).

27. L. C. Biedenharn, M. Goldstein, J. M. McHale, and R. M. Thaler, Phys. Rev. 101, 662 (1956).

28. W. T. Milner, Doctoral Dissertation, University of Tennessee, 1968 (unpublished).

29. R. O. Sayer, Doctoral Dissertation, University of Tennessee, 1968 (unpublished).

30. L. C. Biedenharn and M. E. Rose, Rev. Mod. Phys. 25, 729 (1953).

31. H. J. Rose and D. M. Brink, Rev. Mod. Phys. 39, 306 (1967).

32. L. C. Biedenharn, M. Goldstein, J. M. McHale, and R. M. Thaler, Phys. Rev. 101, 662 (1956).

33. G. Breit, M. E. Ebel, and J. E. Russel, Phys. Rev. 101, 1504 (1956).

34. M. A. Preston, Physics of the Nucleus (Reading, Massachusetts: Addison-Wesley Publishing Co., Inc., 1962).

35. Aage Bohr and Ben R. Mottelson, Dan. Mat. Fys. Medd. 27, No. 16 (1953).

36. Rayleigh, Third Baron, The Theory of Sound (London: Macmillan, 1877), Vol. II, p. 364.

37. R. B. Leighton, Principles of Modern Physics (New York: McGraw-Hill Book Company, 1959).

38. M. G. Mayer, Phys. Rev. 75, 1969 (1949).

39. O. J. Haxel, J. H. D. Jensen, and H. E. Suess, Phys. Rev. 75, 1766 (1949).

40. M. G. Mayer and J. H. D. Jensen, Elementary Theory of Nuclear Shell Structure (New York: John Wiley and Sons, 1955).

41. C. D. Moak, H. E. Banta, J. N. Thurston, J. W. Johnson, and R. F. King, Rev. Sci. Inst. 30, 694 (1959).

42. J. E. Spencer and H. A. Enge, Nucl. Instr. and Meth. 49, 181-193 (1967).

43. J. L. C. Ford, Jr., P. H. Stelson, and R. L. Robinson, Nucl. Instr. and Meth. 98, 199 (1972).

44. C. J. Borkowski and M. K. Kopp, Rev. Sci. Instr. 39, 1515 (1968).

45. W. T. Milner, Tandem Van de Graaff Computer Program Library, ORNL (1976).

46. C. J. Borkowski and M. K. Kopp, Rev. Sci. Instr. 39, No. 10, 1515 (1968).

47. C. J. Borkowski and M. K. Kopp, IEEE Trans. Nucl. Sci. NS-17, No. 3, 340 (1970).

48. W. T. Milner, private communication.

49. J. O. Younghouse, private communication on the tin recovery procedure.

50. F. B. Thomas, private communcation on the tin target plating method.

51. W. C. Davis, private communication.

52. W. K. Dagenhart and T. Wilson Whitehead, Jr., Nucl. Instr. and Meth. 85, 215 (1970).

53. F. K. McGowan and P. H. Stelson, Nuclear Spectroscopy and Reactions, Part C, edited by Joseph Cerny (New York: Academic Press, 1974).

54. L. A. Sliv and I. M. Band, Internal Conversion Coefficients (Amsterdam: North-Holland Publishing Co., 1958).

55. S. Raman and H. J. Kim, Nuclear Data Sheets, 16, No. 2, 195 (1975).

56. W. K. Tuttle, private communication.

57. M. Ferentz and N. Rosenzweig, Table of F Coefficients, ANL-5324.

58. M. Gurevitch, Phys. Rev. 75, 767 (1949).

59. E. A. Ivanov, A. Iordachescu, G. Pascovici, Rev. Roumaine Phys. 13, 879 (1968).

60. E. Ivanov, D. Polstinaru, A. Alevia, D. Poenaru, Rev. Roumaine Phys. 10, 935 (1965).

61. E. A. Ivanov, Rev. Roumaine Phys. 12, 829 (1967).

62. E. A. Ivanov, M. I. Magda, Rev. Roumaine Phys. 12, 227 (1967).

63. S. Raman, private communication.

# APPENDIX

# APPENDIX

## TIN TARGETS BY ELECTRODEPOSITION

### A. PREPARATION OF SOLUTION POTASSIUM STANNATE

1. Weigh approximately twice the quantity of tin (in the form $SnO_2$) required on the target surface. (For 50 mg of tin metal, weigh $\sim$ 127 mg of $SnO_2$.)
2. Transfer tin oxide to a silver crucible and add potassium hydroxide pellets approximately 3 times the weight of $SnO_2$. (For 100 mg of tin (127 mg of $SnO_2$) approximately 400 mg of KOH works well.)
3. Place the silver crucible in a 100 ml Vycor dish, tilting the crucible, such that the oxide and KOH are in intimate contact.
4. Heat the dish, crucible, and contents to 700°C and allow the temperature to remain at 700°C approximately 15 minutes. (Using a small muffle furnace, the fusion step can be completed in about 1 hour, starting at room temperature.)
5. Remove the dish and crucible from the muffle furnace, cover with an inverted beaker, and allow to cool to room temperature. (The fused mass most often appears as a light brown mass (non-liquid) with the color being darker in color if impurities are present.)
6. Cover the crucible with a watch glass and add approximately 2 ml of distilled water. (The watch glass should be replaced over the crucible as soon as the water is added since some heat is

generated and some spattering is involved.) As soon as the initial reaction has ceased and the melt disintegrated, place the dish and covered crucible in a shallow water bath at ∿ 75°C to provide digestion and complete solutioning of the potassium stannate. (In every case so far, a brown solid (presumably silver oxide) appears in the solution and agglomerates on digestion.)

7. Remove the dish from the water bath and wash the underside of the watchglass into the crucible with approximately 1 ml of water with the aid of a medicine dropper.
8. Immediately filter the solution through a very small No. 42 Whatman paper filter into a 10 ml beaker, again making use of a medicine dropper. Wash the crucible, and in-turn the solid on the paper, with three to five 1-ml portions of water such that the total volume in the receiving beaker is 6 to 8 ml. (Retain the paper filter for recovery in the event of enriched tin isotope.)
9. Place the 2 beakers in a shallow water bath at ∿ 75°C and allow the liquid in the smaller beaker to evaporate to approximately 1 ml. (The final volume can be adjusted by placing the beaker adjacent to another 10 ml beaker containing a known 1-ml volume.)
10. Remove the beakers from the water bath and cover with a larger inverted beaker. Retain the solution for plating.

## B. CELL PREPARATION

1. Prior to assembling the plating cell, weigh the cleaned nickel planchet on analytical balance to the nearest tenth of a milligram. (The planchet (plating disc) can be cleaned adequately from organics, surface oils, etc. by soaking the disc for 15 minutes to overnight (dependent on schedule) in ethyl alcohol, then wiping with absorbent tissue.)
2. Set up the small plating cell as shown in Figure 42. The quartz tube should be positioned on a plastic gasket on the nickel planchet approximating the center of the planchet as near as possible. The tube is then held in the centered vertical position by four threaded nuts screwed down to hold the brass plate against the "O" ring.
3. When the cell has been assembled and the 4 nuts tightened equally and firmly, fill the cell with water and let stand for at least 15 minutes to check for leaks around the gasket. (Obviously plating cannot be started until a perfect seal with the gasket has been established.)
4. Remove the water from the cell and replace with 5 ml of a prepared solution of trisodium phosphate (6% solution of $Na_3PO_4 \cdot 12H_2O$). Make electrical connections from a DC source such that the cell frame (and consequently plating disc) is negative and the platinum strip is positive. Adjust the current to 100 mA and continue for three minutes to electro-clean the plating disk.

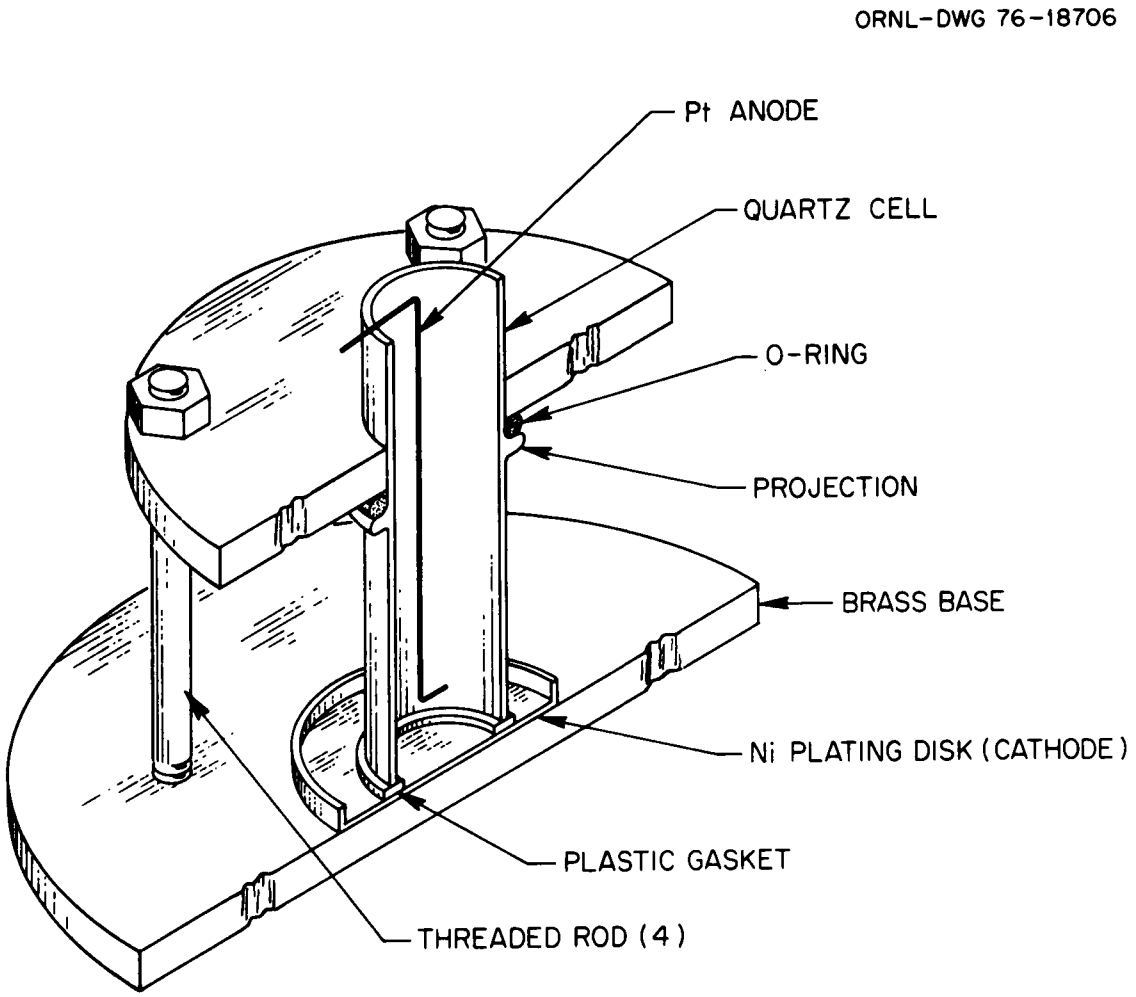


Figure 42. Plating cell apparatus.

5. Disconnect electrical connections and flush the cell with an abundance of distilled water.
6. Add 5 ml of a prepared solution of cuprous cyanide (12 g/liter CuCN, 23 g/liter NaCN, and 15 g/liter $Na_2CO_3$), replace the platinum anode, and re-establish electrical connections. Adjust the current to approximately 20 mA and continue for three minutes to provide a flash coat of copper on the plating disc.
7. Again disconnect electrical connections and flush the cell with an abundance of distilled water. (This solution can be disposed of into the sink drain so long as there is a strong flow of water for dilution.) The cell is now ready for the actual plating.

## C. TIN PLATING

Before plating is begun:

A. A thermostated water bath is set up such that the water temperature is in the range of 75 - 77°C. (A small thermostated hot plate and a large flat-bottomed crystallizing dish works quite well.)

B. If, on visual observation, there is any particulate matter in the plating solution it should be filtered into the cell. This can be accomplished with the very small paper filter, as utilized before, with the aid of a medicine dropper. One milliliter of water is added to the beaker and used to wash the beaker and

filter. Although there is a small loss of sample on the filter due to inadequate washing, retaining the 2-ml volume is felt to be more important than the slight loss. In the event that the plating solution appears to be perfectly clear, a medicine dropper is still the best transfer method, again using one additional ml of water to effect the transfer.

1. As soon as the plating solution is added to the cell, transfer the entire cell to the water bath (already heated to $\sim$ 75°C) and allow to warm to the bath temperature.
2. After approximately 15 minutes insert the platinum anode into the cell (such that the end dips under the plating solution) and complete the electrical connections. Set the amperage by the variac initially at $\sim$ 18 mA. (The matching voltage is usually between 2.5 - 3.0. Very often the amperage begins to climb after a few minutes of plating time--presumably due to the non-homogeneity of the plating solution. As soon as the current exceeds 20 mA, the variac is adjusted in an effort to maintain current settings between 15-20 mA. This plating rate appears to give the most uniform, adherent coatings.)
3. Maintain the water bath temperature between 75 - 77°C throughout the 5 to 5-1/2 hour plating period by periodic additions of hot water. (An auxiliary hot plate of the same type with essentially the same thermostatic setting makes a good way to maintain hot water.) Maintain the water level throughout the plating about 1/4 inch above the plating solution to assure that the plating solution stays at about the same temperature as the bath.

4. At the end of the plating period, turn off the DC Supply, disconnect the electrical leads, and remove the cell from the water bath. Pour the spent plating solution from the cell carefully for future total recovery. Wash the cell and electrode a number of times with distilled water, retaining the washings for tin recovery. Disassemble the cell.
5. Remove the plating disc and wash with distilled water, ethyl alcohol, then acetone, again collecting the washings. Allow the nickel disc to air-dry for at least 15 minutes and then re-weigh on an analytical balance to determine quantity of tin plated. (Good, high-quality tin plates appear white, uniform, and perfectly adherent. Poor quality plates, on the other hand, appear dark and very thin. By controlling the cell volume at approximately 2 ml (for 100 mg or less tin), the temperature between 75 and 80°C, good plates with 50 - 60% plating efficiency can usually be achieved.)

# VITA

William Kelly Dagenhart was born in Stony Point, North Carolina on April 8, 1937. He attended elementary school in Riviera Beach, and Junior High School at Green Haven, Maryland. He graduated from Glen Burnie High School in 1955. The following September he entered the Virginia Polytechnic Institute at Blacksburg, Virginia as a co-operative student with the Bendix Radio Corporation. In June 1960 he received the Bachelor of Science degree in Physics.

In January 1960 he accepted employment at the Oak Ridge National Laboratory. In September 1960 he entered the University of Tennessee, Knoxville for study toward a Master's degree in Physics which he received in December 1964. He then continued study toward a Doctor of Philosophy degree with a major in Nuclear Physics. In April 1975 he transferred full time jobs at the Oak Ridge National Laboratory from the Isotopes Division to the Thermonuclear Division for a research position in plasma heating.

He is married to the former Sally Frances Rorrer and has children; Pamela Lynn Dagenhart born July 17, 1959, William David Dagenhart born May 14, 1962, Keith Randal Dagenhart born February 22, 1964, and Jonathan Kelly Dagenhart born August 2, 1969.